A DMRG study of the Fermi-Hubbard model in hybrid space

Leo Johannes Martin Stenzel

München 2017

A DMRG study of the Fermi-Hubbard model in hybrid space

Leo Johannes Martin Stenzel

Masterarbeit
an der Fakultät für Physik
der Ludwig–Maximilians–Universität
München

vorgelegt von
Leo Johannes Martin Stenzel
aus Starnberg

München, den 6. März 2017

Erstgutachter: Prof. Dr. Ulrich Schollwöck[1]
Zweitgutachter: Prof. Dr. Lode Pollet[1]
Datum der mündlichen Prüfung: 13. März 2017

[1]Fakultät für Physik und Arnold Sommerfeld Zentrum für theoretische Physik, Ludwig-Maximilians-Universität München

Abstract

In this thesis, we find numerical indication for the coexistence of phases with different molar volumes in the repulsive, two-dimensional Fermi-Hubbard model below half-filling.

The Hubbard Hamiltonian is a pinnacle model of strong correlation physics. It has been studied for more than 50 years and the scientific interest increased further due to the more recent realizations of this model in ultracold atoms. Despite its apparent simplicity, the Hubbard model contains a variety of physical effects and is very difficult to assess both analytically and numerically.

This thesis studies the Fermi-Hubbard model in two spatial dimensions. We focus on the case of intermediate to strong repulsion *below* half-filling. This model is believed to describe the physics of quasi two-dimensional layers in high temperature cuprate superconductors.

We employ the DMRG algorithm which is a numerical method for one-dimensional systems. While it can easily be adapted for higher dimensions, this comes at exponentially high costs. To make computations feasible, we enforce symmetries of the Hubbard model explicitly. Apart from particle number conservation we exploit the full $SU(2)$ spin symmetry. Furthermore, we transform our system to *hybrid space* by going into momentum space along the wide axis but staying in real space for the long side of the system. Thus, we can enforce quasi-momentum conservation along the circumference as an additional symmetry. At the same time we preserve open boundaries on two sides—these are generally favored by the DMRG algorithm.

Our method agrees well with benchmark results for the Hubbard model. We observe density fluctuations, "stripes", and exponentially decaying particle number and spin correlations.

Eventually, we discover signs of phase coexistence at intermediate interactions around filling $n = 0.9$ based on thermodynamic arguments. Our observations agree with unpublished Monte Carlo results but we currently lack numerical data to make definitive claims.

We propose a method to reduce the entanglement in a matrix product state during the DMRG procedure. Furthermore, we calculate local projections of the Hamiltonian to gain insight into properties of the ground state and thus suggest a procedure to reduce the influence of open boundaries.

Contents

1 Theory of high-T_c superconductivity

The discovery of the first high-temperature superconductor by Bednorz and Müller [1] in 1986 sparked interest in this new field. As the effect is not only physically fascinating but also relevant for technology, a great amount of experimental research has been conducted since then and many materials which exhibit superconductivity at high temperatures have been discovered (cf. Damascelli [2]). On the theoretical side however there was less success and there is an ongoing discussion about how well existing theories can explain high-T_c superconductivity (cf. "Towards a complete theory of high Tc" [3]). While high-T_c superconductivity is mostly agreed upon to be a phenomenon of strongly correlated electrons, this regime is difficult to assess both with analytic and numeric methods.

In this chapter we will first discuss the basic properties of materials which are high-T_c superconductors. In section 1.2, we will motivate the Hamiltonians used to describe these systems. To set the context for understanding cuprate superconductivity, section 1.3 will recapitulate the "conventional" theory of BCS pairing. We will then discuss how a pairing mechanism might work in cuprates. Finally, in section 1.5 the thermodynamics of phase separation, which is likely to exist in the Hubbard model, is outlined.

1.1 Cuprate superconductors

The 1986 discovery of superconductivity in LaBaCuO systems [1] was not only significant because the critical temperature T_c of the transition to superconductivity was much higher than in all previously known materials. It was scientifically exciting as it led to the discovery of many more superconducting materials (cf. Damascelli [2]) which have very different properties from the "conventional" superconductors which were known before.

High-T_c superconductivity in these materials arises from layers of CuO_2, which is why they are also called cuprates. In fig. 1.1 such two-dimensional planes separated by an isolating layer are shown. This yields a quasi two-dimensional electronic structure as the d-orbital of copper hybridizes with the p-orbitals of the surrounding oxygen atoms.

The *parent compound*, in case of fig. 1.1 $CaCuO_2$ or $BaCuO_2$, itself however is not superconducting [5]. In fact it is an antiferromagnetically ordered Mott insulator, i.e. it should be conductive according to electronic band theory but is not due to electron interactions: while the band is *exactly* half-filled such that electronic excitations should be possible, the strong on-site Coulomb repulsion prohibits any double occupations and no charge transfer is allowed [2].

Any additional charges added to such Mott insulating state can however move in the lattice such that this phase does not exist when dopants are introduced: a schematic phase diagram is shown in fig. 1.2. One can add holes into the CuO_2 layer by replacing some atoms in the isolating layer with elements of lower valency as for example with $La_{2-x}Sr_xCuO_4$ or conversely also add higher valence atoms and thus $|x|$ electrons. Upon doping such cuprates become metallic, though unusual properties remain, i.e. the resistivity is proportional to the temperature [6]. Only upon *overdoping*, increasing the electron (hole) doping $|x|$ beyond the value with highest T_c, "normal", i.e. Fermi-liquid like, resistivity $\propto T^2$ can be observed—although applicability of Fermi-liquid theory is disputed due to strong electronic interactions

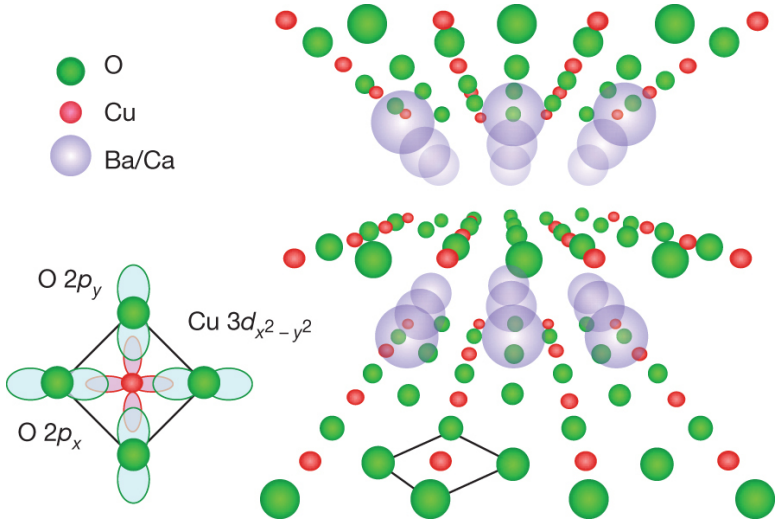

Figure 1.1: Crystal layer structure of copper oxides. Schematic drawing of the hybridization of copper $d_{x^2-y^2}$ holes with p_x and p_y oxygen orbitals. From Keimer et al. [4].

[2]. Note that the experimentally observed phase diagram is asymmetric regarding particle or hole doping and that superconductivity is much more stable on the hole-doped side. While the lack of symmetry is relevant for theoretical models describing cuprates, we will only focus on hole-doped systems.

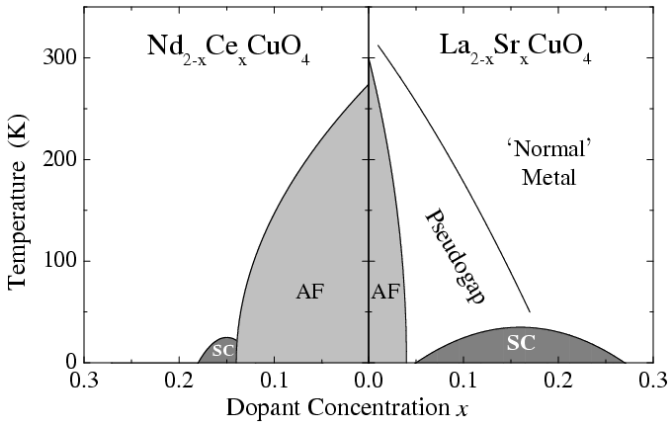

Figure 1.2: Phase diagram for electron- (left side) and hole-doped (right side) high T_c superconductors. At low doping there is an insulating state with antiferromagnetic order (AF), upon higher doping there is a superconducting phase (SC). From Damascelli [2].

1.2 Model Hamiltonians

In this section we want to motivate our description of the cuprate CuO_2 layer. First we want to show that such a 2D system can be described by an extended Hubbard model and then we argue that a single band Hubbard model is probably sufficient to capture the relevant physics. Finally, we want to briefly discuss approximations to the Hubbard model in limiting cases, as these Hamiltonians are frequently studied to describe strongly interacting systems.

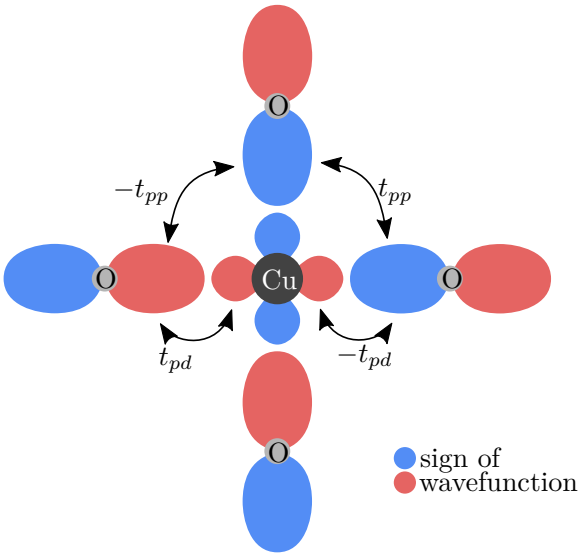

Figure 1.3: Oxygen $p_{x,y}$ orbitals and copper $d_{x^2-y^2}$ orbital. Hopping rates t between neighboring orbitals are shown. Adapted from Annett and Martin [7].

The orbitals which are most relevant for the electronic interactions are the $d_{x^2-y^2}$ orbitals of copper and the oxygen p_x, p_y orbitals, drawn in fig. 1.3. Following Annett and Martin [7], a hole in either orbital contributes an energy ϵ_p, ϵ_d, where we can shift these energies such that one term drops out due to particle conservation.

To model Coulomb repulsion, we introduce an energy U for sites which are vacant (doubly occupied). The authors [7] find that the on-site repulsion is strong for the $d_{x^2-y^2}$ orbitals, but can be neglected for p_x, p_y orbitals, as the energy U_p is much smaller than U_d and the hole density in p-orbitals on oxygen is smaller than in copper d-orbitals. Therefore, longer range repulsion need not be considered, either.

Furthermore, the particles (holes) can hop between neighboring sites with reciprocal rates t_{pp} and t_{pd} as indicated in fig. 1.3. Other authors (e.g. Zhang and Rice [8]) did not consider hopping between p-orbitals explicitly—these can be seen as next-nearest neighbor hopping which can also be realized as virtual hoppings.

We use operators $\hat{c}_\sigma^\dagger$ ($\hat{c}_\sigma$) to create (annihilate) a hole of spin σ, where the spatial index also indicates the kind of orbital the hole is created in: we use the index $\boldsymbol{r}$ for d-orbitals and $\boldsymbol{i}$ for p-orbitals. We define $\hat{n} \coloneqq \hat{c}^\dagger \hat{c}$ to be the hole number operator, $\langle \boldsymbol{r}, \boldsymbol{i} \rangle$ denotes index pairs of nearest neighbors and H.c. is the Hermitian conjugate. We can thus write down the Hamiltonian for this three band model,

$$\begin{aligned} \hat{H}_{\text{three band}} = &\sum_{\boldsymbol{r},\sigma} \epsilon_d \hat{n}_{\boldsymbol{r},\sigma} + U \sum_{\boldsymbol{r}} \hat{n}_{\boldsymbol{r},\uparrow} \hat{n}_{\boldsymbol{r},\downarrow} && d\text{-orbital} \\ &+ \sum_{\boldsymbol{i},\sigma} \epsilon_p \hat{n}_{\boldsymbol{i},\sigma} + \sum_{\langle \boldsymbol{i},\boldsymbol{i'} \rangle,\sigma} \left(t_{\boldsymbol{i},\boldsymbol{i'}} \hat{c}_{\boldsymbol{i},\sigma}^\dagger \hat{c}_{\boldsymbol{i'},\sigma} + \text{H.c.} \right) && p\text{-orbital} \\ &+ \sum_{\langle \boldsymbol{r},\boldsymbol{i} \rangle,\sigma} \left(t_{\boldsymbol{r},\boldsymbol{i}} \hat{c}_{\boldsymbol{r},\sigma}^\dagger \hat{c}_{\boldsymbol{i},\sigma} + \text{H.c.} \right) && p\text{-}d \text{ interaction.} \end{aligned} \tag{1.1}$$

We follow Zhang and Rice [8] and consider the case $\epsilon_d = 0$, $\epsilon_p > 0$, $|t| \to 0$. If one dopes holes into the system they will either localize at Cu sites if $\epsilon_p > U$ or at oxygen sites of $\epsilon_p < U$. In the first case one can find an effective single band Hubbard Hamiltonian by removing the p-orbital contribution in eq. (1.1). In the case $\epsilon_p < U$ this is not as

obvious: Zhang and Rice [8] create a diamond shaped combination of the four oxygen holes surrounding a Cu site such that they arrive, upon orthogonalization, at an effective two band model.

The authors further argue that holes in d-orbitals form singlets with holes in the effective orbitals created from the superposition of four p-orbitals. They find hopping rates for these singlets which are nonvanishing only for nearest neighbor interactions such that they arrive at an effective single band Hubbard model in terms of d-orbital operators,

$$\hat{H}_{\mathrm{Hub}} = \sum_{\langle \boldsymbol{r},\boldsymbol{r'}\rangle,\sigma} \left(\hat{c}^{\dagger}_{\boldsymbol{r},\sigma} \hat{c}_{\boldsymbol{r'},\sigma} + \hat{c}^{\dagger}_{\boldsymbol{r'},\sigma} \hat{c}_{\boldsymbol{r},\sigma} \right) + U \sum_{\boldsymbol{r}} \hat{n}_{\boldsymbol{r},\uparrow} \hat{n}_{\boldsymbol{r},\downarrow}, \tag{1.2}$$

were we have scaled the Hamiltonian such that the hopping rate $t = 1$ is unity. The sum $\langle \boldsymbol{r}, \boldsymbol{r'} \rangle$ goes over nearest neighbors and the spin-$\frac{1}{2}$ operators fulfill anticommutation relations, eq. (1.26).

We note that there is some controversy about whether the reduction to the single band Hamiltonian is sufficient to model the physics of 2D cuprate layers. Annett and Martin [7] reviewed the arguments we just outlined and came to the conclusion that the reduction to a single band model would necessarily introduce longer range hopping. While it is possible that a single band Hubbard model cannot explain the physics of high-T_c superconductors, the crucial point is: we do not know. We consider it reasonable to work with the simplest model until one finds it to be too simple, i.e. insufficient to describe physical effects.

For this thesis we will thus restrict ourselves to studying the **Hubbard Hamiltonian** as given in eq. (1.2). This model has been brought forward by Hubbard [9] in 1963 and has frequently been used as a simple model to describe strongly interacting systems. The model is of quite some academic interest as it has proven to be very hard to analyze both with analytic and numeric methods, especially in the case of strong interaction and doping. The more recent advances in ultracold atomic gases also allow for accurate reproduction of the Hubbard model in well controllable experimental environments, as for example performed by Cheuk et al. [10].

An approximation to the Hubbard model which is frequently used to describe strongly correlated electrons is called the t-J model. There is a discussion of the original derivation by Spalek [11], which we only want to outline briefly.

The ***t-J* model** tries to approximate the Hubbard Hamiltonian in the case of strong-coupling. In this regime the on-site interaction U is significantly larger than the hopping rate $t = 1$, such that a free quasi-particle band theory fails, but not large enough that the atomic limit would be applicable. Due to this "competition" of relevant scales, common perturbative approaches fail.

Spalek [11] considers the Hubbard model slightly below half filling. In the case of strong on-site repulsion the contribution from states with doubly occupied lattice sites will be small. We will separate the Hilbert space into one part without any double occupations and its complement. Denoting by $\overline{\sigma}$ the spin opposite to σ, we can thus write the kinetic term as

$$\mathbb{1} = (1 - \hat{n}_{\boldsymbol{r},\overline{\sigma}})(1 - \hat{n}_{\boldsymbol{r'},\overline{\sigma}}) + (1 - \hat{n}_{\boldsymbol{r},\overline{\sigma}})\hat{n}_{\boldsymbol{r'},\overline{\sigma}} + \hat{n}_{\boldsymbol{r},\overline{\sigma}}(1 - \hat{n}_{\boldsymbol{r'},\overline{\sigma}}) + \hat{n}_{\boldsymbol{r},\overline{\sigma}}\hat{n}_{\boldsymbol{r'},\overline{\sigma}}, \tag{1.3}$$

splitting it into parts which act only on certain subspaces. We can use a Gutzwiller projector $\hat{P}_G$ to restrict $\hat{H}_{\mathrm{Hub}}$ to the subspace with no double occupations and to hoppings from the doubly occupied space by calculating:

$$\hat{P}_G \coloneqq \prod_{\boldsymbol{i}} (1 - \hat{n}_{\boldsymbol{i},\uparrow}\hat{n}_{\boldsymbol{i},\downarrow}), \tag{1.4}$$

$$\hat{P}_G \hat{H}_{\mathrm{Hub}} \hat{P}_G = \sum_{\langle \boldsymbol{r},\boldsymbol{r'}\rangle,\sigma} \hat{c}^\dagger_{\boldsymbol{r},\sigma}(1 - \hat{n}_{\boldsymbol{r},\overline{\sigma}})\hat{c}_{\boldsymbol{r'},\sigma}(1 - \hat{n}_{\boldsymbol{r'},\overline{\sigma}}), \tag{1.5}$$

$$\hat{P}_G \hat{H}_{\mathrm{Hub}} (1 - \hat{P}_G) = \sum_{\langle \boldsymbol{r},\boldsymbol{r'}\rangle,\sigma} \hat{c}^\dagger_{\boldsymbol{r},\sigma}(1 - \hat{n}_{\boldsymbol{r},\overline{\sigma}})\hat{c}_{\boldsymbol{r'},\sigma}\hat{n}_{\boldsymbol{r'},\overline{\sigma}}. \tag{1.6}$$

The contribution from off-diagonal terms, $\hat{P}_G \hat{H}_{\mathrm{Hub}}(1 - \hat{P}_G)$ and its Hermitian conjugate, will be suppressed by a factor U^{-1} such that one can perform a canonical transformation and arrive at an approximation for the Hubbard Hamiltonian near half-filling,

$$\hat{H}_{\mathrm{Hub}} \approx \hat{P}_G \hat{H}_{\mathrm{Hub}} \hat{P}_G - \frac{\hat{P}_G \hat{H}_{\mathrm{Hub}}(1 - \hat{P}_G)\hat{H}_{\mathrm{Hub}}\hat{P}_G}{U}. \tag{1.7}$$

The second term in this approximation accounts for virtual hopping into the subspace with doubly occupied sites. We can express this term using expressions for the projected Hamiltonian we found previously,

$$\begin{aligned}\hat{H}_1 \coloneqq \hat{P}_G \hat{H}_{\mathrm{Hub}}(1 - \hat{P}_G)\hat{H}_{\mathrm{Hub}}\hat{P}_G = \sum_{\langle \boldsymbol{r},\boldsymbol{r'}\rangle,\sigma} \Big(&\hat{c}^\dagger_{\boldsymbol{r},\sigma}(1 - \hat{n}_{\boldsymbol{r},\overline{\sigma}})\hat{c}_{\boldsymbol{r'},\sigma}\hat{n}_{\boldsymbol{r'},\overline{\sigma}} \\ &\times \sum_{\boldsymbol{r''}\in \mathrm{NN}(\boldsymbol{r'}),\sigma'} \hat{n}_{\boldsymbol{r'},\overline{\sigma'}}\hat{c}^\dagger_{\boldsymbol{r'},\sigma'}(1 - \hat{n}_{\boldsymbol{r''},\overline{\sigma'}})\hat{c}_{\boldsymbol{r''},\sigma'}\Big).\end{aligned} \tag{1.8}$$

Close to half-filling it is likely that electrons only hop back and forth between two neighboring sites as most other sites around are already occupied with one electron and must not be filled with two electrons. This corresponds to removing the $\boldsymbol{r''}$ sum and approximating the expression with $\boldsymbol{r''} = \boldsymbol{r}$. We can then write the sum over σ' explicitly and employ commutation relations to find

$$\begin{aligned}\hat{H}_1 &\approx \sum_{\langle \boldsymbol{r},\boldsymbol{r'}\rangle,\sigma} \Big(\hat{c}^\dagger_{\boldsymbol{r},\sigma}(1 - \hat{n}_{\boldsymbol{r},\overline{\sigma}})(1 - \hat{n}_{\boldsymbol{r'},\sigma})\hat{n}_{\boldsymbol{r'},\overline{\sigma}}\hat{c}_{\boldsymbol{r},\sigma} + \hat{c}^\dagger_{\boldsymbol{r},\sigma}\hat{c}_{\boldsymbol{r'},\sigma}\hat{c}^\dagger_{\boldsymbol{r'},\overline{\sigma}}\hat{c}_{\boldsymbol{r},\overline{\sigma}}\Big) \\ &= \sum_{\langle \boldsymbol{r},\boldsymbol{r'}\rangle,\sigma} \Big((1 - \hat{n}_{\boldsymbol{r},\overline{\sigma}})(1 - \hat{n}_{\boldsymbol{r'},\sigma})\hat{n}_{\boldsymbol{r},\sigma}\hat{n}_{\boldsymbol{r'},\overline{\sigma}} - \hat{c}^\dagger_{\boldsymbol{r},\sigma}\hat{c}_{\boldsymbol{r},\overline{\sigma}}\hat{c}^\dagger_{\boldsymbol{r'},\overline{\sigma}}\hat{c}_{\boldsymbol{r'},\sigma}\Big).\end{aligned} \tag{1.9}$$

We can furthermore write $\hat{H}_1$ using spin operators by noticing that for sites occupied with a single spin-$\frac{1}{2}$ particle we can write

$$\hat{\boldsymbol{S}}_{\boldsymbol{r}} \coloneqq \begin{pmatrix} \hat{S}^+_{\boldsymbol{r}}/\sqrt{2} \\ \hat{S}^z_{\boldsymbol{r}} \\ \hat{S}^-_{\boldsymbol{r}}/\sqrt{2} \end{pmatrix} = \frac{1}{2}\begin{pmatrix} \sqrt{2}\,\hat{c}^\dagger_{\boldsymbol{r},\uparrow}\hat{c}_{\boldsymbol{r},\downarrow} \\ \hat{n}_{\boldsymbol{r},\uparrow} - \hat{n}_{\boldsymbol{r},\downarrow} \\ \sqrt{2}\,\hat{c}^\dagger_{\boldsymbol{r},\downarrow}\hat{c}_{\boldsymbol{r},\uparrow} \end{pmatrix}. \tag{1.10}$$

Therefore, the product of such spin operators contains many of the terms in $\hat{H}_1$,

$$\begin{aligned}2\hat{\boldsymbol{S}}_{\boldsymbol{r}} \cdot \hat{\boldsymbol{S}}_{\boldsymbol{r'}} &= \Big(\hat{S}^-_{\boldsymbol{r}}\hat{S}^+_{\boldsymbol{r'}} + \hat{S}^+_{\boldsymbol{r}}\hat{S}^-_{\boldsymbol{r'}}\Big) + 2\hat{S}^z_{\boldsymbol{r}}\hat{S}^z_{\boldsymbol{r'}} \\ &= \hat{c}^\dagger_{\boldsymbol{r},\downarrow}\hat{c}_{\boldsymbol{r},\uparrow}\hat{c}^\dagger_{\boldsymbol{r'},\uparrow}\hat{c}_{\boldsymbol{r'},\downarrow} + \hat{c}^\dagger_{\boldsymbol{r},\uparrow}\hat{c}_{\boldsymbol{r},\downarrow}\hat{c}^\dagger_{\boldsymbol{r'},\downarrow}\hat{c}_{\boldsymbol{r'},\uparrow} + \frac{1}{2}(\hat{n}_{\boldsymbol{r},\uparrow} - \hat{n}_{\boldsymbol{r},\downarrow})(\hat{n}_{\boldsymbol{r'},\uparrow} - \hat{n}_{\boldsymbol{r'},\downarrow}).\end{aligned} \tag{1.11}$$

And we can write our approximation of $\hat{H}_1$ in a more instructive form,

$$\begin{aligned}\hat{H}_1 \approx \sum_{\langle \boldsymbol{r},\boldsymbol{r'}\rangle} & \Big(\sum_{\sigma} (1-\hat{n}_{\boldsymbol{r},\overline{\sigma}})(1-\hat{n}_{\boldsymbol{r'},\sigma})\hat{n}_{\boldsymbol{r},\sigma}\hat{n}_{\boldsymbol{r'},\overline{\sigma}} \\ & \qquad - 2\hat{\boldsymbol{S}}_{\boldsymbol{r}}\cdot\hat{\boldsymbol{S}}_{\boldsymbol{r'}} + (\hat{n}_{\boldsymbol{r},\uparrow}-\hat{n}_{\boldsymbol{r},\downarrow})(\hat{n}_{\boldsymbol{r'},\uparrow}-\hat{n}_{\boldsymbol{r'},\downarrow})/2\Big) \\ = \sum_{\langle \boldsymbol{r},\boldsymbol{r'}\rangle} & \left(-2\hat{\boldsymbol{S}}_{\boldsymbol{r}}\cdot\hat{\boldsymbol{S}}_{\boldsymbol{r'}} + \frac{1}{2}\hat{n}_{\boldsymbol{r}}\hat{n}_{\boldsymbol{r'}}\right).\end{aligned} \tag{1.12}$$

We find the commonly used expression for the t-J model, which is an approximation of the Hubbard model in the case of strong on-site interaction and close to half-filling. We note that it acts only on the reduced Hilbert space without doubly occupied sites which could also make it easier to handle numerically. As it is frequently done, we do not write down the Gutzwiller projectors explicitly and we note that $2t/U = J/t$ to explain the model's name.

$$\hat{H}_{\mathrm{Hub}} \approx \hat{H}_{t-J} = t\sum_{\langle \boldsymbol{r},\boldsymbol{r'}\rangle,\sigma}\left(\hat{c}^{\dagger}_{\boldsymbol{r},\sigma}\hat{c}_{\boldsymbol{r'},\sigma} + \hat{c}^{\dagger}_{\boldsymbol{r'},\sigma}\hat{c}_{\boldsymbol{r},\sigma}\right) + J\sum_{\langle \boldsymbol{r},\boldsymbol{r'}\rangle}\left(\hat{\boldsymbol{S}}_{\boldsymbol{r}}\cdot\hat{\boldsymbol{S}}_{\boldsymbol{r'}} - \frac{1}{4}\hat{n}_{\boldsymbol{r}}\hat{n}_{\boldsymbol{r'}}\right). \tag{1.13}$$

From this approximation it is particularly simple to explain antiferromagnetic correlations at half filling: in this case the kinetic term cannot contribute to the dynamics of electrons as double occupations are prohibited and we are left with an **antiferromagnetic Heisenberg** Hamiltonian.

The t-J model is frequently extended to include further-range hopping. It is argued (e.g. by Lee, Nagaosa, and Wen [6]) that these terms are significant and might help explain the particle-hole asymmetry of the high-T_c phase diagram fig. 1.2. If next-nearest neighbor hopping is introduced with rate t', the effects of the relative sign t'/t are also discussed (e.g. Lee, Nagaosa, and Wen [6] and White and Scalapino [12]). We will come back to these questions in section 2.2.

1.3 Theory of conventional superconductivity

Conventional superconductivity has been known for more than a century as it was first discovered in 1911 by Onnes [13] in mercury cooled to $T \approx 4\mathrm{K}$. Soon after this discovery superconductivity was also found in tin and lead and since then conventional superconductivity has been discovered in more than 20 metallic elements [14]. Yet, it took almost half of this century for Bardeen, Cooper, and Schrieffer [15] (BCS) to arrive at a complete theoretical explanation in 1957, for which they were awarded the Nobel Prize in 1972.

The idea that electrons can form pairs, much like "molecules", which would then behave as bosonic particles and could condense in a common ground state, a Bose-Einstein condensate, had been around before (cf. Bardeen and Schrieffer [16]). While such a state would be superfluid, in order to form electronic pairs which are localized in space, one would require a binding force which overcomes the Coulomb repulsion. Note that such states have however been realized in ultracold atoms where the interaction strength of Fermions can be tuned [17].

Instead there are pairwise excitations of particles close to the Fermi surface, which are not localized in real space. The argument goes along the lines of Bardeen and Schrieffer [16]:

Considering a non-interacting system with Hamiltonian $\hat{H}_0$ and adding some interaction $\hat{U}$ such that:

$$\begin{aligned} \hat{H} &= \hat{H}_0 + \hat{U}, \\ \hat{H}_0 \left|\psi_i\right\rangle &= E_i \left|\psi_i\right\rangle . \end{aligned} \tag{1.14}$$

The interaction $\hat{U}$ is off-diagonal and while it is Hermitian, U_{ij} can have an arbitrary phase. Assume there is a subset of such eigenstates for which the interaction lowers the energy,

$$A = \{|\psi\rangle \text{ eigenstate of } \hat{H} \mid \forall \psi, \phi \in A : \ \Re \left\langle\psi\right| \hat{U} \left|\phi\right\rangle \leq 0\}. \tag{1.15}$$

Then we can define a state $|\Psi\rangle$ that decreases in energy as interaction is turned on as,

$$|\Psi\rangle = \sum_{|\psi_j\rangle \in A} a_j \left|\psi_j\right\rangle , \quad a_j \geq 0, \tag{1.16}$$

$$\left\langle\Psi\right| \hat{H} \left|\Psi\right\rangle = \sum_{|\psi_j\rangle \in A} a_j^2 E_j + \sum_{|\psi_i\rangle, |\psi_j\rangle \in A} a_i a_j U_{ij}. \tag{1.17}$$

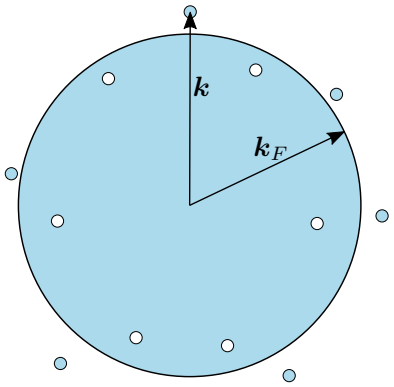

Figure 1.4: Configuration with particles excited above the Fermi surface (filled circles) and corresponding holes below. Adapted from Bardeen and Schrieffer [16]

The idea is that the attractive electronic interaction is mediated by phonons (cf. Kittel [18]): one electron distorts the atomic lattice, looses momentum to create a phononic excitation, a second electron "sees" the distortion and absorbs phonon momentum. The interaction is therefore not local in space and does not need to compete with the Coulomb repulsion. As superconductivity occurs at low temperatures, the electronic states we consider are close to the Fermi surface (compare fig. 1.4) and there are only very few phonons.

We consider a simple Hamiltonian where electrons and phonons only interact with the other species but not with their own kind. We assume the coupling amplitude D to be small and constant for the momenta transferred at low temperatures. Electrons are created (annihilated) by the fermionic operators $\hat{c}^\dagger$ ($\hat{c}$), phonons by the bosonic $\hat{a}^\dagger$ ($\hat{a}$). Their dispersion relations are $\epsilon_{\boldsymbol{k}}$ and $\omega_{\boldsymbol{q}}$ respectively,

$$\hat{H} = \underbrace{\sum_{\boldsymbol{q}} \omega_{\boldsymbol{q}} \hat{a}^\dagger_{\boldsymbol{q}} \hat{a}_{\boldsymbol{q}} + \sum_{\boldsymbol{k}} \epsilon_{\boldsymbol{k}} \hat{c}^\dagger_{\boldsymbol{k}} \hat{c}_{\boldsymbol{k}}}_{\hat{H}_0} + \underbrace{\mathrm{i}\, D \sum_{\boldsymbol{k},\boldsymbol{q}} \hat{c}^\dagger_{\boldsymbol{k}+\boldsymbol{q}} \hat{c}_{\boldsymbol{k}} (\hat{a}_{\boldsymbol{q}} - \hat{a}^\dagger_{-\boldsymbol{q}})}_{\hat{U}} . \tag{1.18}$$

We can transform the Hamiltonian as

$$\hat{H}' = \mathrm{e}^{-\hat{S}} \, \hat{H} \, \mathrm{e}^{\hat{S}} = \hat{H} + [\hat{H}, \hat{S}] + \frac{1}{2}[[\hat{H}, \hat{S}], \hat{S}] + \ldots , \tag{1.19}$$

and we can choose $\hat{S}$ such that the off-diagonal contribution vanishes to first order of D in this expansion. We find for eigenstates $|\phi\rangle , |\psi\rangle$ of $\hat{H}_0$:

$$0 \stackrel{!}{=} \mathrm{i}\, D\hat{U} + [\hat{H}_0, \hat{S}], \tag{1.20}$$

$$\Rightarrow \quad \langle\psi|\, \hat{S}\, |\phi\rangle = \mathrm{i}\, D \frac{\langle\psi|\, \hat{U}\, |\phi\rangle}{E_\phi - E_\psi} \tag{1.21}$$

Close to $T = 0$ we only consider states with either zero or one phonons such that we only need two matrix elements,

$$\langle 1_{\boldsymbol{q}}|\, \hat{S}\, |0\rangle = -\,\mathrm{i}\, D \sum_{\boldsymbol{k}} \hat{c}^\dagger_{\boldsymbol{k}-\boldsymbol{q}} \hat{c}_{\boldsymbol{k}} \frac{1}{\epsilon_{\boldsymbol{k}} - \epsilon_{\boldsymbol{k}-\boldsymbol{q}} - \omega_{\boldsymbol{q}}}, \tag{1.22}$$

$$\langle 0|\, \hat{S}\, |1_{\boldsymbol{q}}\rangle = \mathrm{i}\, D \sum_{\boldsymbol{k}'} \hat{c}^\dagger_{\boldsymbol{k}'+\boldsymbol{q}} \hat{c}_{\boldsymbol{k}'} \frac{1}{\epsilon_{\boldsymbol{k}'} + \omega_{\boldsymbol{q}} - \epsilon_{\boldsymbol{k}'+\boldsymbol{q}}}. \tag{1.23}$$

And we find an effective Hamiltonian with electronic interactions, where the operators are projected onto the state with zero phonons,

$$\begin{aligned}
\hat{H}' &\approx \hat{H}_0 + \frac{1}{2}[\mathrm{i}\, D\hat{U}, \hat{S}] + \mathcal{O}(D^3) \\
&= \hat{H}_0 + \frac{1}{2} D^2 \sum_{\boldsymbol{q}} \sum_{\boldsymbol{k},\boldsymbol{k}'} \hat{c}^\dagger_{\boldsymbol{k}'+\boldsymbol{q}} \hat{c}_{\boldsymbol{k}'} \hat{c}^\dagger_{\boldsymbol{k}-\boldsymbol{q}} \hat{c}_{\boldsymbol{k}} \left(\frac{1}{\epsilon_{\boldsymbol{k}} - \epsilon_{\boldsymbol{k}-\boldsymbol{q}} - \omega_{\boldsymbol{q}}} - \frac{1}{\epsilon_{\boldsymbol{k}'} + \omega_{\boldsymbol{q}} - \epsilon_{\boldsymbol{k}'+\boldsymbol{q}}} \right) \\
&= \hat{H}_0 + D^2 \sum_{\boldsymbol{q}} \sum_{\boldsymbol{k},\boldsymbol{k}'} \hat{c}^\dagger_{\boldsymbol{k}'+\boldsymbol{q}} \hat{c}_{\boldsymbol{k}'} \hat{c}^\dagger_{\boldsymbol{k}-\boldsymbol{q}} \hat{c}_{\boldsymbol{k}} \frac{\omega_{\boldsymbol{q}}}{(\epsilon_{\boldsymbol{k}'} - \epsilon_{\boldsymbol{k}'+\boldsymbol{q}})^2 - \omega_{\boldsymbol{q}}^2}.
\end{aligned} \tag{1.24}$$

Where for the last step we have assumed the phonon dispersion to be invariant under spatial inversion $\omega_{\boldsymbol{q}} = \omega_{-\boldsymbol{q}}$ and resummed these terms by exchanging $\boldsymbol{k}, \boldsymbol{k}'$.

One can see how the effective electron interaction can lower the energy as demanded in eq. (1.17) when $|\epsilon_{\boldsymbol{k}} - \epsilon_{\boldsymbol{k}-\boldsymbol{q}}| < \omega_{\boldsymbol{q}}$. Therefore, the **Fermi surface is unstable** against the formation of such Cooper pairs. In the following we will only consider the case when the net momentum of the interacting electrons is zero, i.e. $\boldsymbol{k}' + \boldsymbol{k} = 0$. Note that until now we did not consider the electronic spin. The common argument is that the energy will be lower for an antiparallel spin configuration then for a parallel one, thus it should suffice to consider a reduced Hamiltonian,

$$H_{\mathrm{red}} = \sum_{\boldsymbol{k},\sigma} \epsilon_{\boldsymbol{k}} \hat{c}^\dagger_{\boldsymbol{k},\sigma} \hat{c}_{\boldsymbol{k},\sigma} + \sum_{\boldsymbol{k},\boldsymbol{k}'} V_{\boldsymbol{k}\boldsymbol{k}'} \hat{c}^\dagger_{\boldsymbol{k},\uparrow} \hat{c}^\dagger_{-\boldsymbol{k},\downarrow} \hat{c}_{-\boldsymbol{k}',\downarrow} \hat{c}_{\boldsymbol{k}',\uparrow}. \tag{1.25}$$

If we want to consider the full BCS many-particle wave function we need to remember that we are dealing with fermions of momentum $\boldsymbol{k}$ and spin σ and thus we have the anticommutation relations,

$$\begin{aligned}
\{\hat{c}^\dagger_{\boldsymbol{k},\sigma}, \hat{c}_{\boldsymbol{k}',\sigma'}\} &= \delta_{\boldsymbol{k},\boldsymbol{k}'} \delta_{\sigma,\sigma'}, \\
\{\hat{c}_{\boldsymbol{k},\sigma}, \hat{c}_{\boldsymbol{k}',\sigma'}\} = \{\hat{c}^\dagger_{\boldsymbol{k},\sigma}, \hat{c}^\dagger_{\boldsymbol{k}',\sigma'}\} &= 0.
\end{aligned} \tag{1.26}$$

If we define an order for $i := (\boldsymbol{k}, \sigma)$ we can write any state $|\psi\rangle$ as the sum of products of creation operators in the appropriate order, weighted by complex factors $c_{\boldsymbol{i}}$ as

$$|\psi\rangle = \sum_{\{\boldsymbol{i}\}} |\psi_{\boldsymbol{i}}\rangle = \sum_{\{\boldsymbol{i}\}} c_{\boldsymbol{i}} \hat{c}^\dagger_{i_1} \cdots \hat{c}^\dagger_{i_N} |0\rangle\,. \tag{1.27}$$

If we act on this state with operators $\hat{c}_j \hat{c}_k$, as we do in the interaction term, we only find contributions from states $|\psi_{\boldsymbol{i}}\rangle$ for which there are indices $i_{m,l} = j, k$. However, we will find a relative minus sign depending on the occupation of the states *between* (in terms of our

index order) the particles we annihilate. If we define by $\boldsymbol{i'}$ the ordered indices $\boldsymbol{i}$ with the elements $i_{l,m}$ removed, we find using the antisymmetric tensor ϵ,

$$\hat{c}_{i_l}\hat{c}_{i_m}\left|\psi_{\boldsymbol{i}}\right\rangle = \epsilon_{i_l,i_m}(-1)^{m-l}\hat{c}_{i'_1}\cdots\hat{c}_{i'_{N-2}}\left|0\right\rangle. \tag{1.28}$$

Therefore, if we evaluate $\langle\psi|\,\hat{c}^\dagger_{\boldsymbol{q}+\boldsymbol{k}}\hat{c}_{\boldsymbol{k}}\hat{c}^\dagger_{\boldsymbol{k'}-\boldsymbol{q}}\hat{c}_{\boldsymbol{k'}}\left|\psi\right\rangle$ for a random state $|\psi\rangle$, we would find both positive and negative contributions and the expectation value should vanish. However if we restrict ourselves to states created by pair creation operators, $\hat{c}^\dagger_{\boldsymbol{k},\uparrow}\hat{c}^\dagger_{-\boldsymbol{k},\downarrow}$, we can only find even values for $m-l$ as used in eq. (1.28). Considering $\boldsymbol{k'}=3$ with the blue spins created using pair creation operators one can picture this as shown in table 1.1

$\uparrow\downarrow$	$\uparrow\downarrow$	$\uparrow\downarrow$	$\uparrow\downarrow$	$\uparrow\downarrow$	$\uparrow\downarrow$	$\uparrow\downarrow$	$\uparrow\downarrow$	$\uparrow\downarrow$
$k=-4$	$k=-3$	$k=-2$	$k=-1$	$k=0$	$k=1$	$k=2$	$k=3$	$k=4$

Table 1.1: BCS pair configuration. We act with pair creation operators to create the *red* spins at sites $\boldsymbol{k'}=\pm 3$. The *blue* spins have been created using pair-wise operators, gray denotes unoccupied states. By using pair creation operators, we ensure that there is an even number of occupied states "between" a new pair.

In this way we can create many Cooper pairs and find a many-body wave function with lower energy than the non-interacting ground state. We do not want to explicitly construct the ground-state wave function to explore its properties, instead we want to briefly analyze the reduced Hamiltonian from eq. (1.25), following Tinkham [19]. We define $b_{\boldsymbol{k}}$ to be the average of the pair annihilation operator such that we can perform a mean field approximation for small deviations $\hat{\delta}_{\boldsymbol{k}}$,

$$b_{\boldsymbol{k}} \coloneqq \langle\hat{c}_{-\boldsymbol{k},\downarrow}\hat{c}_{\boldsymbol{k},\uparrow}\rangle, \tag{1.29}$$

$$\hat{c}_{-\boldsymbol{k},\downarrow}\hat{c}_{\boldsymbol{k},\uparrow} = b_{\boldsymbol{k}} + \hat{\delta}_{\boldsymbol{k}}, \tag{1.30}$$

$$\Delta_{\boldsymbol{k}} \coloneqq -\sum_{\boldsymbol{k'}} V_{\boldsymbol{k},\boldsymbol{k'}}\langle\hat{c}_{-\boldsymbol{k'},\downarrow}\hat{c}_{\boldsymbol{k'},\uparrow}\rangle = -\sum_{\boldsymbol{k'}} V_{\boldsymbol{k},\boldsymbol{k'}}b_{\boldsymbol{k'}}. \tag{1.31}$$

One can express the reduced Hamiltonian from eq. (1.25) to first order of the pair fluctuations,

$$\begin{aligned}\hat{H}_{\mathrm{MF}} &= \sum_{\boldsymbol{k},\sigma}\epsilon_{\boldsymbol{k}}\hat{c}^\dagger_{\boldsymbol{k},\sigma}\hat{c}_{\boldsymbol{k},\sigma} + \sum_{\boldsymbol{k},\boldsymbol{k'}}V_{\boldsymbol{k}\boldsymbol{k'}}\left(\hat{c}^\dagger_{\boldsymbol{k},\uparrow}\hat{c}^\dagger_{-\boldsymbol{k},\downarrow}b_{\boldsymbol{k'}} + b^*_{\boldsymbol{k}}\hat{c}_{-\boldsymbol{k'},\downarrow}\hat{c}_{\boldsymbol{k'},\uparrow} - b^*_{\boldsymbol{k}}b_{\boldsymbol{k'}}\right)\\ &= \sum_{\boldsymbol{k},\sigma}\epsilon_{\boldsymbol{k}}\hat{c}^\dagger_{\boldsymbol{k},\sigma}\hat{c}_{\boldsymbol{k},\sigma} - \sum_{\boldsymbol{k}}\left(\Delta_{\boldsymbol{k}}\hat{c}^\dagger_{\boldsymbol{k},\uparrow}\hat{c}^\dagger_{-\boldsymbol{k},\downarrow} + \Delta^*_{\boldsymbol{k}}\hat{c}_{-\boldsymbol{k},\downarrow}\hat{c}_{\boldsymbol{k},\uparrow} - \Delta_{\boldsymbol{k}}b^*_{\boldsymbol{k}}\right).\end{aligned} \tag{1.32}$$

This mean-field Hamiltonian can be diagonalized by introducing Bogoliubov fermions $\hat{\gamma}_{\boldsymbol{k}}$,

$$\hat{c}_{\boldsymbol{k},\uparrow} = u^*_{\boldsymbol{k}}\hat{\gamma}_{\boldsymbol{k},\downarrow} + v_{\boldsymbol{k}}\hat{\gamma}^\dagger_{\boldsymbol{k},\uparrow}, \tag{1.33}$$

$$\hat{c}^\dagger_{-\boldsymbol{k}\downarrow} = -v^*_{\boldsymbol{k}}\hat{\gamma}_{\boldsymbol{k},\downarrow} + u_{\boldsymbol{k}}\hat{\gamma}^\dagger_{\boldsymbol{k},\uparrow}. \tag{1.34}$$

We require $|u_{\boldsymbol{k}}|^2 + |v_{\boldsymbol{k}}|^2 = 1$ to fulfill the commutation relations and we can choose the coefficients in such way that all off-diagonal terms in the transformed Hamiltonian vanish by requiring

$$0 \overset{!}{=} 2\epsilon_{\boldsymbol{k}}u_{\boldsymbol{k}}u_{\boldsymbol{k}} + \Delta^*_{\boldsymbol{k}}v^2_{\boldsymbol{k}} - \Delta_{\boldsymbol{k}}u^2_{\boldsymbol{k}}, \tag{1.35}$$

$$\frac{\Delta^*_{\boldsymbol{k}}v_{\boldsymbol{k}}}{u_{\boldsymbol{k}}} = \sqrt{\epsilon^2_{\boldsymbol{k}} + |\Delta_{\boldsymbol{k}}|^2} - \epsilon_{\boldsymbol{k}}. \tag{1.36}$$

The resulting Hamiltonian in terms of the Bogoliubov operators is given by

$$\hat{H}_{\mathrm{MF}} = \sum_{\boldsymbol{k}} \left(\epsilon_{\boldsymbol{k}} - \sqrt{\epsilon_{\boldsymbol{k}}^2 + |\Delta_{\boldsymbol{k}}|^2} + \Delta_{\boldsymbol{k}} b_{\boldsymbol{k}}^* \right) + \sum_{\boldsymbol{k},\sigma} \sqrt{\epsilon_{\boldsymbol{k}}^2 + |\Delta_{\boldsymbol{k}}|^2} \hat{\gamma}_{\boldsymbol{k},\sigma}^\dagger \hat{\gamma}_{\boldsymbol{k},\sigma}. \tag{1.37}$$

The first sum yields a constant by which the energy is lowered as the $\Delta_{\boldsymbol{k}}$ becomes finite, the second sum gives the excitations in terms of Bogoliubov quasiparticles. The excitation term also explains why we defined $\Delta_{\boldsymbol{k}}$ in this way: it is the gap in the excitation spectrum.

For finite temperatures we can thus use the Fermi distribution to express the occupation numbers of the free fermions $\hat{\gamma}_{\boldsymbol{k}}^{(\dagger)}$,

$$E_{\boldsymbol{k}} \coloneqq \sqrt{\epsilon_{\boldsymbol{k}}^2 + |\Delta_{\boldsymbol{k}}|^2} \tag{1.38}$$

$$\langle \hat{\gamma}_{\boldsymbol{k},\sigma}^\dagger \hat{\gamma}_{\boldsymbol{k},\sigma} \rangle = f(E_{\boldsymbol{k}}) \coloneqq (1 + \exp(\beta E_{\boldsymbol{k}}))^{-1}. \tag{1.39}$$

Thus, we can use our definition of the gap $\Delta_{\boldsymbol{k}}$ from eq. (1.31) to express it in terms of Bogoliubov operators,

$$\begin{aligned} \Delta_{\boldsymbol{k}} &= -\sum_{\boldsymbol{k}'} V_{\boldsymbol{k},\boldsymbol{k}'} u_{\boldsymbol{k}'}^* v_{\boldsymbol{k}'} \left\langle 1 - \sum_\sigma \hat{\gamma}_{\boldsymbol{k}',\sigma}^\dagger \hat{\gamma}_{\boldsymbol{k}',\sigma} \right\rangle \\ &= -\sum_{\boldsymbol{k}'} V_{\boldsymbol{k},\boldsymbol{k}'} \frac{\Delta_{\boldsymbol{k}'}}{2E_{\boldsymbol{k}'}} \tanh \frac{\beta E_{\boldsymbol{k}'}}{2}. \end{aligned} \tag{1.40}$$

To find the **critical temperature T_c** a self-consistency equation for the particle number is also needed, as the mean field Hamiltonian eq. (1.32) does not preserve particle number. Finally, using the assumption that $V_{\boldsymbol{k},\boldsymbol{k}'} = -V$ is constant up to the cutoff frequency ω_c, one can find a temperature dependent expression for $\Delta_{\boldsymbol{k}} = \Delta$ and find T_c by setting the gap equal to zero [19],

$$k_B T_c = 1.13 \hbar \omega_c \, \mathrm{e}^{-1/N(0)V}, \tag{1.41}$$

$N(0)$ being the density of states at the Fermi surface.

1.4 Pairing in high-T_c superconductors

In section 1.3 we saw how small attractive interactions between electrons can lead to the formation of Cooper pairs, destabilize the Fermi surface and lead to a superconducting phase. For high-T_c superconductors we also expect to find some kind of pairing mechanism such that the pairs can condense into a coherent state. However, we should not expect the mechanisms to be similar: cooper pairing occurs for pairs of particles close to the Fermi surface, i.e. we consider a system of free quasiparticles in a given band structure. Cuprate superconductors on the other hand are strongly interacting electronic systems. In the case of small doping, as shown in fig. 1.2, they are Mott insulators—states which cannot be adequately described by band theory.

The physical idea for high-T_c pairing is the formation of electronic singlet pairs which can be motivated like this: without doping the ground state of cuprates (see fig. 1.2) is an antiferromagnetic Mott insulator. Due to the strong on-site Coulomb repulsion, hopping of electrons is prohibited such that the system can effectively be described by spin interactions. This can be seen from the $\hat{\boldsymbol{S}} \cdot \hat{\boldsymbol{S}}$ term in the t-J model in eq. (1.13). Once holes are doped however, the antiferromagnetic order of the ground state of a Heisenberg model becomes frustrated.

A simple motivation why holes form pairs when doped into an antiferromagnetic Mott insulator can be found e.g. in Demler [20] and is sketched in fig. 1.5. If a single hole moves through the antiferromagnetic background, it creates a stripe of ferromagnetic bonds and thus increases the energy. Therefore, assuming there are two adjacent holes, these holes will not separate but rather move through the lattice as a bound pair. This does not yet explain why localized pairs should be created in the first place. One could motivate the formation of such pairs by arguing that theses pairs can lower their energy by delocalizing in the lattice and are thus more favorable than single holes.

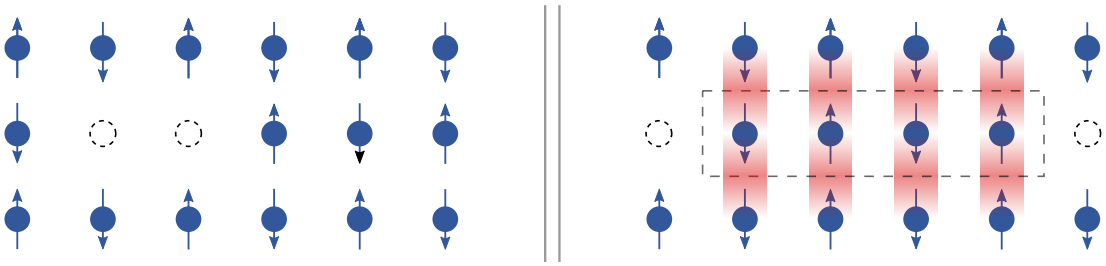

Figure 1.5: If holes move through the antiferromagnetic background they create a "string" of ferromagnetic bonds and thus increase the energy proportional to the distance they moved. A localized pair of holes should therefore tend to stay bound as it moves through the lattice.

A more quantitative explanation for high-T_c pairing was published by Anderson et al. [21]. They argue that the Mott insulator upon doping behaves like other frustrated spin systems, i.e. on triangular lattices, where the theory of **resonating valence bonds** (RVB) had been brought forward by Fazekas and Anderson [22]. In a cuprate layer these singlets are not necessarily nearest neighbors allowing for movement of the holes as shown in fig. 1.6.

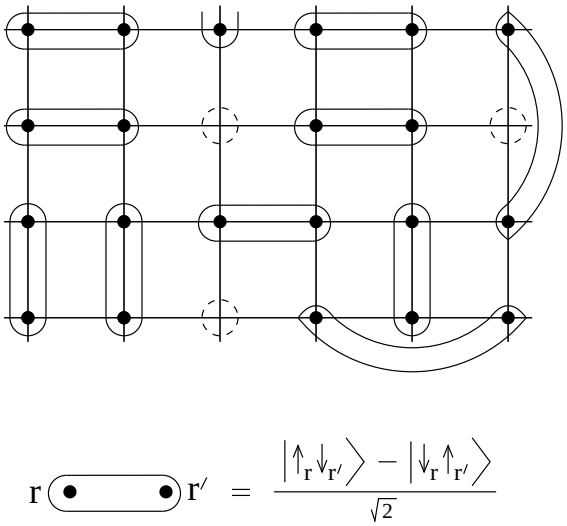

Figure 1.6: Possible configuration of electronic singlet pairs, i.e. *valence bonds* in a system with doped holes. There would be many such configurations degenerate in energy such that the system would resonate among them. Such state is therefore called "resonating valence bond" (RVB) state. From Anderson et al. [21].

If one considers a pair of spins coupled by a Heisenberg exchange with positive J corresponding to antiferromagnetic coupling,

$$\hat{H} = J\hat{\boldsymbol{S}}_1 \cdot \hat{\boldsymbol{S}}_2 = \frac{J}{2}\left[(\hat{\boldsymbol{S}}_1 + \hat{\boldsymbol{S}}_2)^2 - \hat{\boldsymbol{S}}_1^2 - \hat{\boldsymbol{S}}_2^2\right], \tag{1.42}$$

the energy of a singlet pair is $-S(S+1)J$. The "quantum-mechanical" factor of $(S+1)$ stabilizes the singlet, especially for spin-$\frac{1}{2}$ particles. In one dimension such dimer pairs are energetically favorable, in a two dimensional spin lattice the antiferromagnetic Néel state is slightly superior at $-\frac{J}{2}$ compared to $-\frac{3}{8}J$ for singlet pairs [6].

Anderson [23] proposed that such singlet pairs exist in cuprate layers such that these pairs would become superfluid once charge transport is possible due to doping. In this paper he constructs an RVB wave function by creating valence bond pairs displaced by $\boldsymbol{\tau}$ in space,

$$\frac{1}{\sqrt{N}} \sum_{\boldsymbol{j}} \hat{c}^\dagger_{\boldsymbol{j},\uparrow} \hat{c}^\dagger_{\boldsymbol{j}+\boldsymbol{\tau},\downarrow} = \frac{1}{\sqrt{N}} \sum_{\boldsymbol{k}} \mathrm{e}^{\mathrm{i}\,\boldsymbol{k}\cdot\boldsymbol{\tau}}\, \hat{c}^\dagger_{\boldsymbol{k},\uparrow} \hat{c}^\dagger_{-\boldsymbol{k},\downarrow}. \tag{1.43}$$

The phase $\mathrm{e}^{\mathrm{i}\,\boldsymbol{k}\cdot\boldsymbol{\tau}}$ which appears upon transformation to momentum space can generally be a function $a(\boldsymbol{k})$ where we require $\sum_{\boldsymbol{k}} a(\boldsymbol{k}) = 0$ in order to avoid doubly occupied sites in the limit of strong repulsion.

To create a RVB wave function of N electrons Anderson suggested using a Gutzwiller projector $\hat{P}_G$ we defined in eq. (1.4) on the product of $\frac{N}{2}$ singlet pair creators,

$$|\Psi_{\mathrm{RVB}}\rangle \propto \hat{P}_G \left(\sum_{\boldsymbol{k}} a(\boldsymbol{k}) \hat{c}^\dagger_{\boldsymbol{k},\uparrow} \hat{c}^\dagger_{-\boldsymbol{k},\downarrow} \right)^{N/2} |0\rangle\,. \tag{1.44}$$

In the same paper Anderson [23] points out that this RVB state can also be obtained starting from a variational BCS wave function

$$|\Psi_{\mathrm{BCS}}\rangle = \prod_{\boldsymbol{k}} \left(u_{\boldsymbol{k}} + v_{\boldsymbol{k}} \hat{c}^\dagger_{\boldsymbol{k},\uparrow} \hat{c}^\dagger_{-\boldsymbol{k},\downarrow} \right) |0\rangle = \exp\left(\sum_{\boldsymbol{k}} \frac{v_{\boldsymbol{k}}}{u_{\boldsymbol{k}}} \hat{c}^\dagger_{\boldsymbol{k},\uparrow} \hat{c}^\dagger_{-\boldsymbol{k},\downarrow} \right) |0\rangle\,, \tag{1.45}$$

which becomes the RVB state from eq. (1.44) upon projecting it onto the space with $\frac{N}{2}$ pairs and removing double occupancies,

$$|\Psi_{\mathrm{RVB}}\rangle \propto \hat{P}_G \hat{P}_{N/2} \,|\Psi_{\mathrm{BCS}}\rangle \propto \hat{P}_G \left(\sum_{\boldsymbol{k}} \frac{v_{\boldsymbol{k}}}{u_{\boldsymbol{k}}} \hat{c}^\dagger_{\boldsymbol{k},\uparrow} \hat{c}^\dagger_{-\boldsymbol{k},\downarrow} \right)^{N/2}. \tag{1.46}$$

Variational Monte Carlo calculations of the resonating valence bond state in the two dimensional Hubbard model have been performed by Paramekanti, Randeria, and Trivedi [24]. They find that this state is not the true ground state but argue that their approach might still describe physical properties of cuprates as details of the microscopic Hamiltonian should not affect the behavior too much. Due to their restrictions on the variational states, they could obtain results for systems up to sizes of 19×19.

They can observe how a variational parameter $\tilde{\Delta}_{\mathrm{var}} = \Delta_0/t$, which would correspond to the amplitude of the gap as in eq. (1.49), vanishes for a critical doping x_c as shown in fig. 1.7a. There is no more pairing for higher hole doping. Furthermore, they investigate the pairing symmetry: there are theoretical and experimental arguments for a $d_{x^2-y^2}$ symmetric shape of the gap, unlike the s-wave gap of BCS superconductors. A review of these arguments can be found by Scalapino [25]. Different gap shapes are sketched in fig. 1.8. The decisive part is the position and orientation of nodes in the surface: an s-wave gap generally has no symmetry protected nodes or, in the case of an extended s-wave which is shown, a more or less isotropic node. In the case of d-wave gaps, there are orthogonal nodes going through the center of the Brillouin zone and thus also crossing the Fermi surface. There is a relative sign for orthogonal vectors in a d-wave shape, i.e. a different sign for singlet pairs along either axis in a cuprate material.

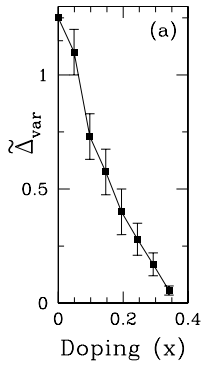

(a) The variational parameter $\tilde{\Delta}_{\rm var}$ for doping $x = 1 - n$. The "gap" closes at x_c such that there is no more pairing.

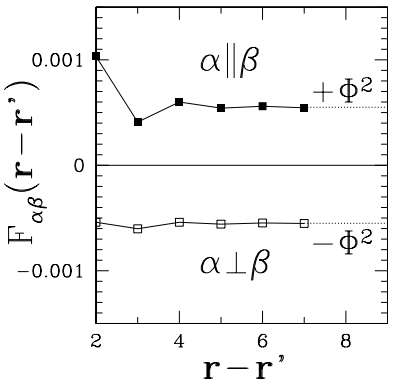

(b) Singlet pairing correlations approach a finite value for increasing distance which corresponds to the order parameter Φ^2. There is a relative minus sign for parallel and orthogonal displacement, indicating d-wave symmetry.

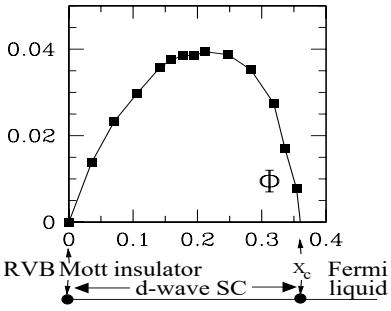

(c) The d-wave superconducting order parameter Φ is finite for a range of doping $0 < x \lesssim 0.35$.

Figure 1.7: Results from variational Monte Carlo computations assuming the RVB state in the Hubbard model. From Paramekanti, Randeria, and Trivedi [24]

Paramekanti, Randeria, and Trivedi [24] measure pairing correlators along either axis: a singlet between sites $\boldsymbol{r}$ and $\boldsymbol{r} + \boldsymbol{\alpha}$ is created by $\hat{B}^\dagger_{\boldsymbol{r},\boldsymbol{\alpha}}$, such that they consider correlators $F_{\boldsymbol{\alpha\beta}}$,

$$\hat{B}^\dagger_{\boldsymbol{r},\boldsymbol{\alpha}} = \frac{1}{2}\left(\hat{c}^\dagger_{\boldsymbol{r},\uparrow}\hat{c}^\dagger_{\boldsymbol{r}+\boldsymbol{\alpha},\downarrow} - \hat{c}^\dagger_{\boldsymbol{r},\downarrow}\hat{c}^\dagger_{\boldsymbol{r}+\boldsymbol{\alpha},\uparrow}\right), \tag{1.47}$$

$$F_{\boldsymbol{\alpha},\boldsymbol{\beta}}(\boldsymbol{r},\boldsymbol{r'}) := \langle \hat{B}^\dagger_{\boldsymbol{r},\alpha}\hat{B}_{\boldsymbol{r'},\boldsymbol{\beta}}\rangle. \tag{1.48}$$

As shown in fig. 1.7b, the correlator $F_{\boldsymbol{\alpha},\boldsymbol{\beta}}(|\boldsymbol{r}-\boldsymbol{r'}|)$ approaches a finite value for large distances $|\boldsymbol{r} - \boldsymbol{r'}|$. The magnitude is the same for either parallel or orthogonal pair displacements $\boldsymbol{\alpha}$, $\boldsymbol{\beta}$ but the sign differs—indicating $d_{x^2-y^2}$ symmetry.

An argument to motivate that pairs created by doping a Mott insulator exhibit d-wave symmetry has been brought forward by Scalapino and Trugman [26]. The $d_{x^2-y^2}$-symmetric gap should be like

$$\Delta_{d_{x^2-y^2}}(\boldsymbol{k}) = \Delta_0(\cos k_x - \cos k_y), \tag{1.49}$$

with some amplitude Δ_0. Thus, the corresponding operator for creating a hole pair is given by

$$\begin{aligned}\frac{1}{N}\sum_{\boldsymbol{k}}\Delta_{d_{x^2-y^2}}(\boldsymbol{k})\hat{c}_{\boldsymbol{k},\uparrow}\hat{c}_{-\boldsymbol{k},\downarrow} &= \frac{\Delta_0}{N^3}\sum_{\boldsymbol{k}}\left(\sum_{\boldsymbol{r},\boldsymbol{r'}} \mathrm{e}^{\mathrm{i}\,\boldsymbol{k}\cdot(\boldsymbol{r}-\boldsymbol{r'})}\,\hat{c}_{\boldsymbol{r},\uparrow}\hat{c}_{\boldsymbol{r'},\downarrow}\right)(\cos k_x - \cos k_y) \\ &= \frac{\Delta_0}{4N}\sum_{\boldsymbol{r}}\big[\,(\hat{c}_{\boldsymbol{r}+\boldsymbol{x},\uparrow}\hat{c}_{\boldsymbol{r},\downarrow} - \hat{c}_{\boldsymbol{r}+\boldsymbol{x},\downarrow}\hat{c}_{\boldsymbol{r},\uparrow}) - (\hat{c}_{\boldsymbol{r}+\boldsymbol{y},\uparrow}\hat{c}_{\boldsymbol{r},\downarrow} - \hat{c}_{\boldsymbol{r}+\boldsymbol{y},\downarrow}\hat{c}_{\boldsymbol{r},\uparrow}) \\ &\quad + (\hat{c}_{\boldsymbol{r}-\boldsymbol{x},\uparrow}\hat{c}_{\boldsymbol{r},\downarrow} - \hat{c}_{\boldsymbol{r}-\boldsymbol{x},\downarrow}\hat{c}_{\boldsymbol{r},\uparrow}) - (\hat{c}_{\boldsymbol{r}-\boldsymbol{y},\uparrow}\hat{c}_{\boldsymbol{r},\downarrow} - \hat{c}_{\boldsymbol{r}-\boldsymbol{y},\downarrow}\hat{c}_{\boldsymbol{r},\uparrow})\,\big].\end{aligned} \tag{1.50}$$

This operator creates singlet hole pairs on adjacent lattice sites in either x or y direction, where the amplitude exhibits a relative $(+-+-)$ phase. While the pairs need not be on neighboring sites, the angular dependence of the phase is decisive for $d_{x^2-y^2}$ symmetry, in contrast to e.g. s-wave symmetry in conventional superconductors where no such phase exists.

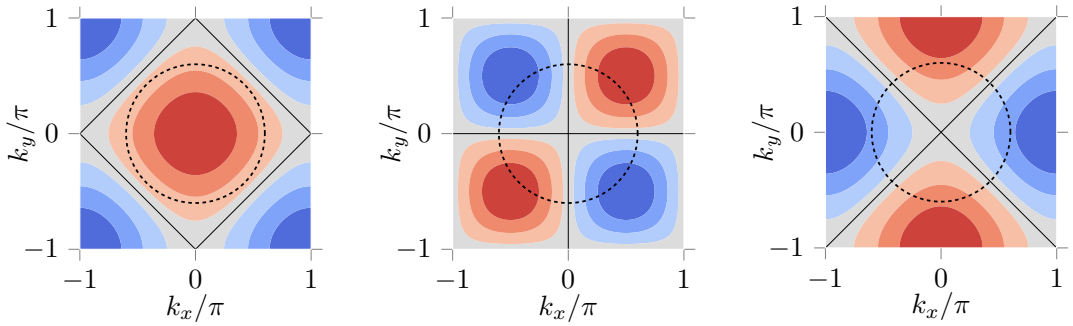

(a) Extended s-wave, i.e. $\Delta_{s^*} \propto \cos k_x + \cos k_y$.

(b) d_{xy} wave symmetry $\Delta_{x_{xy}} \propto \sin k_x \sin k_y$.

(c) $d_{x^2-y^2}$ symmetric gap, i.e. $\Delta_{d_{x^2-y^2}} \propto \cos k_x - \cos k_y$.

Figure 1.8: Different shapes of gap symmetries. The dashed line indicates a possible Fermi surface, the thin lines are zeros of the excitation spectrum. An s-wave gap is more or less isotropic but there is a relative sign for orthogonal axes in the d-wave gaps.

High-T_c superconductivity is expected to be found upon doping hole pairs into a Mott insulating state. We want to motivate that the ground state of the doped system can be created by acting with $d_{x^2-y^2}$ hole pair creation operators on the Mott insulator. We want to show this for the plaquette in fig. 1.9 with a Hubbard Hamiltonian, eq. (1.2).

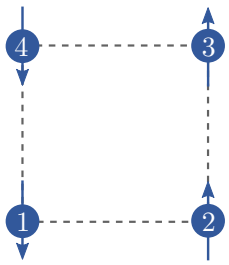

Figure 1.9: A plaquette, four sites taken from a square lattice with antiferromagnetic spin order shown. Adapted from Scalapino and Trugman [26]

For the noninteracting case, the ground state of the doped system on the plaquette consists of two electrons in the $k = 0$ state, thus of opposite spin:

$$|\psi_2\rangle = N \left(\hat{c}^\dagger_{1,\downarrow} + \hat{c}^\dagger_{2,\downarrow} + \hat{c}^\dagger_{3,\downarrow} + \hat{c}^\dagger_{4,\downarrow}\right) \left(\hat{c}^\dagger_{1,\uparrow} + \hat{c}^\dagger_{2,\uparrow} + \hat{c}^\dagger_{3,\uparrow} + \hat{c}^\dagger_{4,\uparrow}\right) |0\rangle \,. \tag{1.51}$$

This state has s-wave symmetry as pairs created along x direction, i.e. $\hat{c}^\dagger_{1,\downarrow}\hat{c}^\dagger_{2,\uparrow}$, have the same sign as pairs displaced along y direction, $\hat{c}^\dagger_{1,\downarrow}\hat{c}^\dagger_{4,\uparrow}$. The authors argue that introducing interactions would suppress double occupations and increase antiferromagnetic correlations, which would change the amplitude of different pair operators but would not introduce nodes or a relative minus sign. Thus the ground state is of s-wave form,

$$|\psi_2\rangle = \sum_{\boldsymbol{k}} \Delta_s(\boldsymbol{k})\, \hat{c}^\dagger_{\boldsymbol{k},\uparrow} \hat{c}^\dagger_{-\boldsymbol{k},\downarrow} |0\rangle \,. \tag{1.52}$$

The gap might be of form $\Delta_{s^*}(\boldsymbol{k}) = \Delta_0 (\cos k_x + \cos k_y)$, to restrict ourselves to nearest neighbor interaction ("extended s-wave"), but could generally be of other nodeless form.

At half-filling and strong on-site repulsion the ground state of the plaquette is an antiferromagnetic, Mott insulating state:

$$|\phi_a\rangle = \hat{c}^\dagger_{4,\downarrow}\hat{c}^\dagger_{2,\downarrow}\hat{c}^\dagger_{3,\uparrow}\hat{c}^\dagger_{1,\uparrow} |0\rangle \,, \qquad |\phi_b\rangle = \hat{c}^\dagger_{3,\downarrow}\hat{c}^\dagger_{1,\downarrow}\hat{c}^\dagger_{4,\uparrow}\hat{c}^\dagger_{2,\uparrow} |0\rangle \,. \tag{1.53}$$

If one dopes a hole pair into either state one finds a relative sign: depending on whether the pair is displaced along x or y direction we find due to the anticommutation relations eq. (1.26):

$$\begin{aligned} \hat{c}_{1,\uparrow}\hat{c}_{2,\downarrow}\left|\phi_a\right\rangle &= -\hat{c}^\dagger_{4,\downarrow}\hat{c}_{2,\downarrow}\hat{c}^\dagger_{2,\downarrow}\hat{c}^\dagger_{3,\uparrow}\hat{c}_{1,\uparrow}\hat{c}^\dagger_{1,\uparrow}\left|0\right\rangle = -\hat{c}^\dagger_{4,\downarrow}\hat{c}^\dagger_{3,\uparrow}\left|0\right\rangle, \\ \hat{c}_{1,\uparrow}\hat{c}_{4,\downarrow}\left|\phi_a\right\rangle &= \hat{c}_{4,\downarrow}\hat{c}^\dagger_{4,\downarrow}\hat{c}^\dagger_{2,\downarrow}\hat{c}^\dagger_{3,\uparrow}\hat{c}_{1,\uparrow}\hat{c}^\dagger_{1,\uparrow}\left|0\right\rangle = \hat{c}^\dagger_{2,\downarrow}\hat{c}^\dagger_{3,\uparrow}\left|0\right\rangle. \end{aligned} \tag{1.54}$$

Therefore, if we act on $\left|\phi_{a,b}\right\rangle$ with a s-wave pair creation operator, the overlap with $\left|\psi_2\right\rangle$ vanishes. In the case of s-wave symmetric operators with isotropic real space coefficients $a(|\boldsymbol{r}-\boldsymbol{r'}|)$, this can be seen most easily,

$$\left\langle\psi_2\right|\sum_{\boldsymbol{k}}\Delta_s(\boldsymbol{k})\hat{c}_{\boldsymbol{k},\uparrow}\hat{c}_{-\boldsymbol{k},\downarrow}\left|\phi_{a,b}\right\rangle \propto \left\langle\psi_2\right|\sum_{\boldsymbol{r},\boldsymbol{r'}}a(|\boldsymbol{r},\boldsymbol{r'}|)\hat{c}_{\boldsymbol{r},\uparrow}\hat{c}_{\boldsymbol{r'},\downarrow}\left|\phi_{a,b}\right\rangle = 0. \tag{1.55}$$

Thus, the ground state of the doped system $\left|\psi\right\rangle$ cannot be created by doping s-wave hole pairs into a Mott insulator. Instead, to create hole pairs from half-filled Mott insulators, which is the physically relevant limit for cuprate superconductors, one has to introduce a relative sign for the operators in eq. (1.54), which corresponds to a d-wave shaped gap.

1.5 Phase separation

In fig. 1.2 we have seen that there are various, rather extraordinary phases present in high-T_c superconductors. The fact that different phases compete with each other might be crucial for the physics of cuprates. Experimentally, quasi-static stripes have been observed in some high-T_c materials, i.e. by Tranquada et al. [27] in $La_{1.6-x}Nd_{0.4}Sr_xCuO_4$. Competition of phases might also be the reason why Hubbard and related models are difficult to simulate in the physically interesting regions, as we will see in the next chapter. We want to briefly recapitulate the thermodynamic basics of phase transitions to understand how phase coexistence and separation can be observed.

Following arguments by Landau and Lifshitz [28] a phase transition requires the *intensive variables* to be equal,

$$T_1 = T_2, \qquad P_1 = P_2 \qquad \text{and} \qquad \mu_1 = \mu_2, \tag{1.56}$$

as the two phases are in contact and at thermal equilibrium. As the *Gibbs free energy* is constant, it is natural to use it to describe the system,

$$\mathrm{d}\,g = -s\,\mathrm{d}\,T + v\,\mathrm{d}\,P, \tag{1.57}$$

where we have used only intensive variables, i.e. molar entropy $s \coloneqq S/N$ and volume $v \coloneqq V/N$. However, g is not *differentiable* at a phase transition: this corresponds to a finite change of volume and entropy, respectively. A jump in volume at the critical pressure is sketched in fig. 1.10.

If we consider the van der Waals equation of state, we do not see the finite jumps at the phase transition. The P-v diagram we considered in fig. 1.10 instead shows regions where v cannot be expressed as a function of P, see fig. 1.11. A *Maxwell construction*, indicated by the dashed lines, is required to find the physically realized behavior of a jump of volumes.

The Gibbs free energy is however impractical to describe our simulations: we do control the temperature—as we do ground state physics we expect $T = 0$—however we cannot control the pressure. We can only set the volume as we vary system size and particle number, i.e.

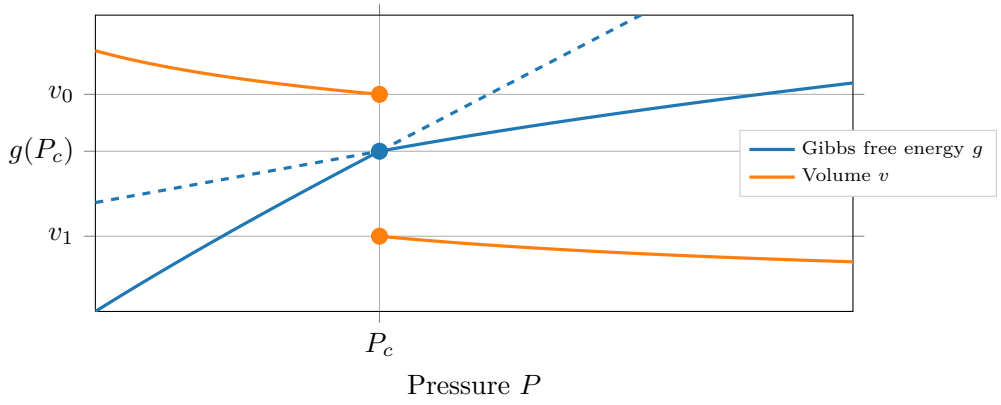

Figure 1.10: The Gibbs free energy is continuous at a phase transition but not differentiable. The volume $v = \partial_P g|_T$, corresponding to the slope of the dashed lines, makes a finite jump at the transition.

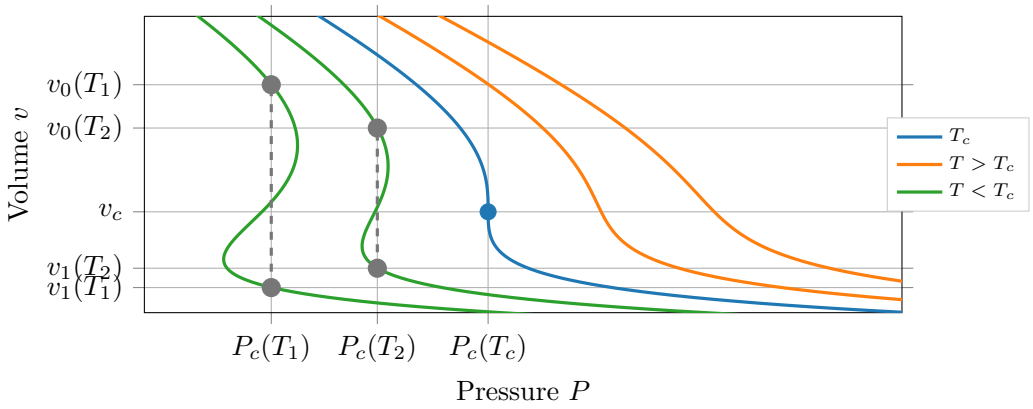

Figure 1.11: *Van der Waals* isotherms. At the critical temperature T_c there is the onset of a phase transition at the point where $\partial P/\partial v = 0$. At lower temperatures regions emerge where there are multiple values for v at given pressure. This is not realized physically, instead there is phase coexistence and the system evolves along a *Maxwell construction*. This is indicated by the dashed lines and corresponds to the jump in fig. 1.10

hole doping. This corresponds to describing the system in terms of the *free energy*[1] we can find using a Legendre transformation, which is given at a phase transition by [29]

$$f(T, v) = \inf_P \left[g(T, P) - Pv \right]. \tag{1.58}$$

The Gibbs free energy is concave in pressure, therefore the free energy needs to be convex in volume. Assuming that the free energy is twice differentiable, this is equivalent to demanding that the second derivative with respect to the volume is non-negative,

$$\left.\frac{\partial^2 f(v,T)}{\partial v^2}\right|_T = \left.\frac{\partial P}{\partial v}\right|_T \geq 0. \tag{1.59}$$

[1] At $T = 0$ the free energy f is just equivalent to the internal energy u. In some sense we do not only keep the temperature fixed at $T = 0$ but also the entropy $s = 0$.

We note that this expression is proportional to the isothermal compressibility. Naively, an equation of state at a phase transition might give a free energy which is not convex, as shown in fig. 1.12. The proper Legendre transformation as given in eq. (1.58) gives the true, linear dependence $P_c v$ as the phases mix between (A) and (B).

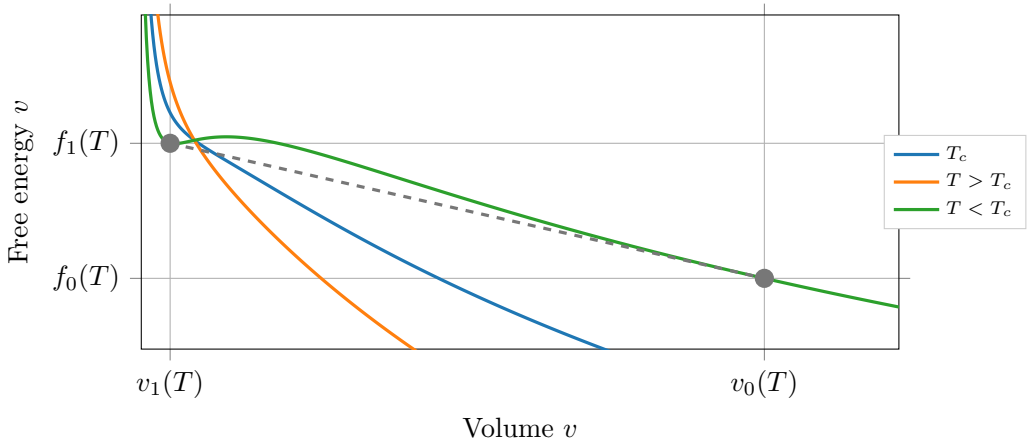

Figure 1.12: A system minimizes the free energy $f(v, T)$ by realizing phase coexistence. Naively, the equation of state, in this case for the *van der Waals* system, would suggest that the free energy is not convex in v. The mixture of both phases is given by a Maxwell constructions and corresponds to the dashed line. For the temperature shown in the green curve, there is a maximum of the free energy. This is however not necessary for phase coexistence, concavity of the curve is sufficient.

As we use DMRG which describes a real physical system, we should observe such linear dependence of the energy on the volume. At the phase transition, this corresponds to

$$\left.\frac{U}{N}\right|_{\text{pt}} = u\big|_{\text{pt}} = c_1 + c_2 \frac{V}{N} \qquad \Leftrightarrow \qquad U\big|_{\text{pt}} = c_1 N + c_2 V, \tag{1.60}$$

where we will use the number of doped holes as particle number N. If we prohibited phase separation, i.e. by *enforcing* a uniform state, we would not see this linear behavior but instead we would find f not to be convex in this region.

2 Numerical results for strongly correlated fermions

Due to the lack of analytic understanding of the Hubbard model at interactions and doping relevant to superconductivity, various numerical methods, in particular *exact diagonalization* and *quantum Monte Carlo*, have been employed since around 1990 (e.g. [30–32]). While there have been great advances in algorithms and technology, understanding of the interacting many-electron problem did not improve much since then.

In the following section we want to argue that the problem of many interacting particles is actually really hard. The rest of this chapter is dedicated to a review of numerical results from other groups. We want to study which methods have been used to gain physical understanding for strongly correlated systems.

2.1 The interacting many-electron problem

The Hilbert space of a many-electron system grows exponentially in the system's size, such that the computational effort for any straightforward approach to solve the system, such as exact diagonalization, will also scale exponentially. These simple methods are thus restricted to system sizes $\lesssim 20$ sites and cannot be used to understand phenomena in the thermodynamic limit.

For classical or also bosonic systems the go-to method is the Monte Carlo sampling where the partition function,

$$Z = \operatorname{tr} \mathrm{e}^{-\beta \hat{H}} = \sum_{|\psi\rangle} \sum_{n=0}^{\infty} \frac{(-\beta)^n}{n!} \langle\psi| \hat{H}^n |\psi\rangle \tag{2.1}$$

is evaluated stochastically. For Fermions however, this is difficult in many cases as the fermionic operators $\hat{c}^{(\dagger)}$ fulfill anticommutation relations, such that the different summands of $\hat{H}^n$ can be of either sign after reordering. This effect is known as the *sign problem* [33] and leads once more to an **exponential scaling of computational effort**.

For these reasons there is still highly active research on rather simple models for strongly correlated electrons, with many new numerical methods being developed. A recent review of results for the two dimensional Hubbard model using various numerical approaches has been compiled by the Simons Foundation, LeBlanc et al. [34]. They only consider observables which are easily accessible with all methods, i.e. the energy per site and the number of double occupations $D \propto \langle \sum_i \hat{n}_{i,\uparrow} \hat{n}_{i,\downarrow} \rangle$. The paper therefore primarily serves as a benchmark to compare new approaches with.

LeBlanc et al. [34] find good agreement of the different methods in the cases of

- half-filling—the system can be approximated by a Heisenberg model, as we found in section 1.2 and particle-hole symmetry cancels the sign problem in Monte Carlo simulations,
- small interaction U and

- far away from half-filling—in these cases particles (holes) behave much like free particles.

Conversely, the different numerical methods do not agree very well in the case of large interaction ($U \gtrsim 8$) and low doping ($1 > n \gtrsim 0.875$) which might explain the physics of high-T_c superconductors and is thus most interesting. The authors reason that a strong competition between different phases makes this regime difficult to assess numerically.

2.2 Review of published results

Numerical studies of strongly correlated many particle systems have often been performed using t-J or t-t'-J like models. We consider these Hamiltonians as approximations to the more physically motivated Hubbard model. However, they are potentially easier to compute numerically as their local Hilbert space is smaller and they have also been used for analytic calculations of high-T_c cuprates, e.g. see Lee, Nagaosa, and Wen [6].

As the Hubbard model and t-(t')-J models can be studied in terms of the same observables, we want to review results for the latter models as well. We find it particularly interesting to see which physical effects are "robust" enough to appear in both models—as these phenomena might just be the most relevant ones for the class of high-T_c superconductors.

Our review will **focus on tensor network methods** which makes it particularly easy to compare results with our approach. We do not consider this to be too much of a restriction, as e.g. the review by LeBlanc et al. [34] proves DMRG to be on par with any other numerical method. While the system sizes considered are strictly limited in width, DMRG gives access to the full ground state wave function to calculate observables.

In this section we will start by discussing the "simplest" t-J model, we will proceed by introducing a next-nearest neighbor hopping rate t' and finally we will come to the model we are actually studying, the Hubbard Hamiltonian. For all systems, we will in particular discuss properties of the particle density distributions. They are frequently used to determine *stripe formation* and to find signs for *phase separation*—for the latter one expects to find phases of different particle densities.

There has been an extensive discussion on whether the ground state of t-t'-J models exhibits stripes characterized by higher hole concentrations. A review of mostly DMRG results on this question has been published by Scalapino and White [35]. It is stated that stripes are found in experiments on cuprates and also that Hartree-Fock calculations indicate stripes in the Hubbard model—however, both kind of stripes appear to be incompatible. The authors note that the formation of stripes might be related to whether there is phase separation in Hubbard and t-J models: if there is separation into regions with different hole densities, these regions might form stripes if they repel each other through long ranged Coulomb interaction.

Early DMRG simulations for the **2D t-J model** by White and Scalapino [12] found a striped density pattern as shown in fig. 2.1. They considered the commonly used filling of $n = 7/8$ and interaction strength $2/U \approx J = 0.35$ with hopping rate set to $t = 1$. One can observe how antiferromagnetic regions, drawn in green and blue, are separated by hole rich domain walls with a phase shift of π. We note the cylindrical boundary conditions broke translational symmetry along one axis such that one finds inhomogeneous particle number expectation values $\langle \hat{n}_{\boldsymbol{r}} \rangle$. Furthermore, a staggered magnetic field was applied to the open ends to break spin symmetry, such that finite expectation values $\langle \hat{S}^z_{\boldsymbol{r}} \rangle$ could be observed.

In a later publication White and Scalapino [37] found that stripes are sensitive to the physical parameters of the t-J model. For small doping $x := 1 - n \lesssim 1/8$ they find

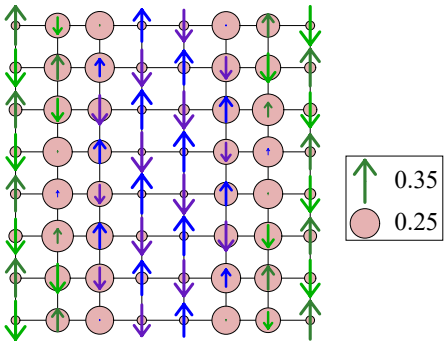

Figure 2.1: Hole rich stripes separating antiferromagnetic regions in the 2D t-J model. Diameters of the circles are proportional to hole densities $(1 - \langle \hat{n}_{\boldsymbol{r}} \rangle)$, the arrows correspond to local spin expectation values $\langle \hat{S}^x_{\boldsymbol{r}} \rangle$. Simulation result by White and Scalapino [36] using DMRG on a 16×8 site cylinder (only center region is shown).

the previously discussed domain walls along the periodic y-axis with spacing $\propto 1/x$. At larger hole doping there are also diagonal domain walls with higher linear density. These phases can separate in areas with different hole densities for long lattices (i.e. 40×6). A superposition of both kinds of domain walls is also possible and shown in fig. 2.2. However, additional fields were required during the buildup of the state and pinning fields to break the translational symmetry along y were applied.

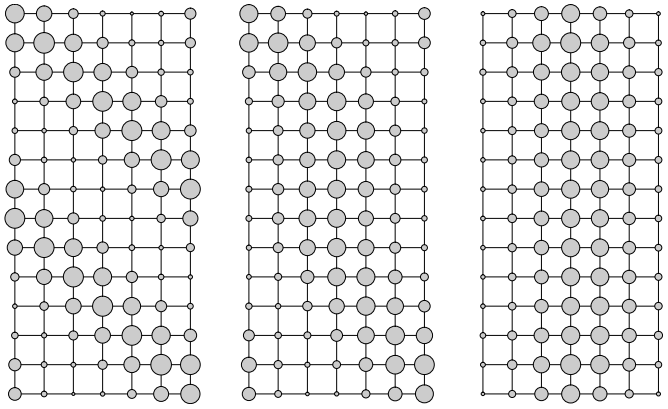

Figure 2.2: Domain walls along different directions in the 2D t-J model. External fields enforced the orientation of the domain walls during initial sweeps, but the system was allowed to relax at later stages. DMRG result at doping $1 - n = 1/7$ by White and Scalapino [37].

The stripes parallel to the lattice vectors generally appeared along the y direction—which is due to the cylindrical boundary conditions. However, domain walls along the x direction with open ends could be enforced by making the nearest neighbor interaction anisotropic, i.e. $J_x/J_y \approx 1.2$ [35].

These observations show that the t-J model is sensitive to boundary conditions and that there might be competing phases. The authors argue that the last DMRG sweeps for which there were no additional fields applied give the system a chance to relax to its true ground state. It is very well possible for the optimization algorithm to get stuck in local minima and influencing convergence behavior has to be done with great care. However, White and Scalapino [38] were unable to stabilize a uniform wave function making the argument for stripes more robust.

As the systems sizes achievable with DMRG are strictly limited, the influence of finite size effects remains an important question. Corboz, Rice, and Troyer [39] addressed this using iPEPS, an inherently two dimensional tensor network approach which describes systems of infinite size. For an introduction to this method see e.g. the review by Orús [40]. They were able to reproduce hole density stripes in qualitative agreement with DMRG results [41].

However, there is bias in the iPEPS method as well. One needs to choose a unit cell of the infinite, two dimensional tensor network; possible unit cells are shown in fig. 2.3a. Thus, the ground state can break translation symmetry, but only in a way which is compatible with the symmetry of the unit cell of tensors. This limits the variational space, but it can be advantageous as it allows for direct comparison of ground states with different spatial symmetries.

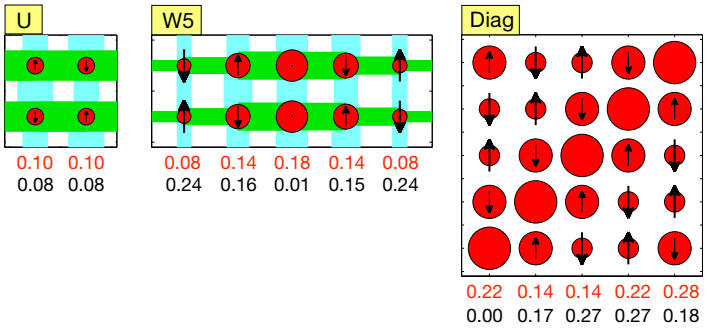

(a) Different unit cells of tensors allow for different states of the infinite system. Shown is the uniform state "U" with only two different tensors, the 5×2 supercell "W5" which allows stripes and a diagonal 5 unit cell made up from 5 different tensors. Local hole densities (magnetic moments) are denoted by the diameter of the red circles (length of black arrows) and their values are shown below. Bond thickness corresponds to the singlet pairing amplitude with different signs for x and y direction.

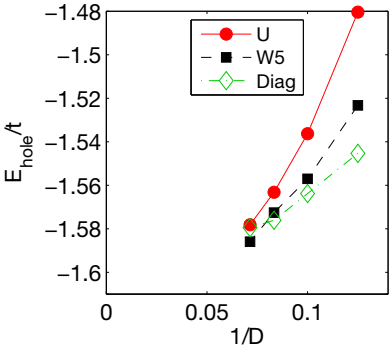

(b) Energy per hole versus reciprocal bond dimension for the different unit cells shown on the left. Results are given for doping $x = 0.12$ and interaction $J/t = 0.4$.

Figure 2.3: Ground state energies using iPEPS for different tensor network unit cells and bond dimensions D. From Corboz, Rice, and Troyer [39].

Using different unit cells of tensors, the energy for uniform, striped and diagonal states can be compared directly. iPEPS does not require extrapolation to infinite size, however, due to the different tensor network geometry, the bond dimension of the tensors is about a thousand times smaller than for DMRG. While a two dimensional tensor network can store correlations much more efficiently, extrapolation in the bond dimension is crucial. The ground state energy for the mentioned geometries versus the reciprocal bond dimension is shown in fig. 2.3b. At the largest achievable bond dimensions the striped state has the lowest energy, however the difference to a uniform state is closing with increasing bond dimension.

We note that iPEPS seems to be a good approach to distinguish stripes and uniform states, however it fails to describe phenomena like **phase separation**. White and Scalapino [38] reviewed arguments about phase separation in the t-J models and their own DMRG calculations. They considered the range of hole doping $0.07 \leq x \leq 0.25$—higher doping is not relevant for cuprates, very low doping is more difficult to realize numerically. They compared results for the energy per site, respectively per hole, in dependence of doping. If there was phase separation, the energy should go *exactly* linear with hole density in the thermodynamic limit, as we discussed in section 1.5. Using DMRG, White and Scalapino [38] found nearly linear results, especially for doping $x \leq 0.12$. However, there are only few

possible values of x which can be calculated on small lattices such that the authors did not claim to have observed phase transition. They argue that this near linearity is due to the very weak repulsion of stripes, which they consider the ground state to be made up of. They also compare to quantum Monte Carlo results which seem to indicate phase separation, as the energy per hole is not convex with doping. However, the energies found with variational Monte Carlo approaches were generally higher than DMRG results, especially higher than the difference between uniform and striped state. Thus, they were not considered to be trustworthy by White and Scalapino [38].

We want to note that if quantum Monte Carlo enforced a uniform state, without stripes but in particular without phase separation, it would actually be possible to observe a local minimum for the energy versus doping. As DMRG simulates an actual physical system, uniformity of the wave function is not enforced and one would not observe local extrema, but instead a linear region. The fact that DMRG energies are lower than for calculations of a uniform state might be due to stripe formation but might also actually be an indication *for* phase separation.

For larger values of J, which are however not of physical interest, phase separation can be observed. Shih, Chen, and Lee [42] performed Monte Carlo simulations for a variety of exchange rates J and could observe phase separation clearly for e.g. $J = 2.5$. When J approaches the value of 0.4 the energy versus doping curves became almost linear such that they could not find a conclusion within error bars. Rommer, White, and Scalapino [43] studied phase separation at large J using DMRG on ladders. As the method gives access to the ground state wave function, the separation into regions of different hole densities can be observed directly, see fig. 2.4a. They found that the critical value of J for phase separation depended on the total electron number as depicted in fig. 2.4b. Rommer, White, and Scalapino [43] could find phase separation only for larger exchange rates than the previously discussed Monte Carlo study. This might be due to the different geometries and system sizes considered. We expect the results of Shih, Chen, and Lee [42] on larger lattices with periodic boundaries to be more precise.

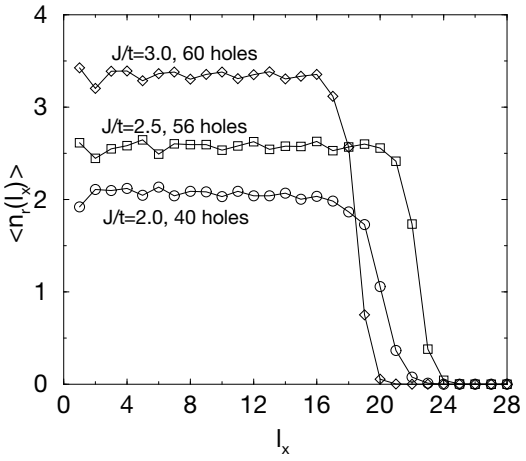

(a) The hole number per rung $\langle n_r \rangle$ for a 4×28 t-J ladder. The separation in a half-filled phase and a phase where the hole density is dependent on exchange rate J is clearly visible.

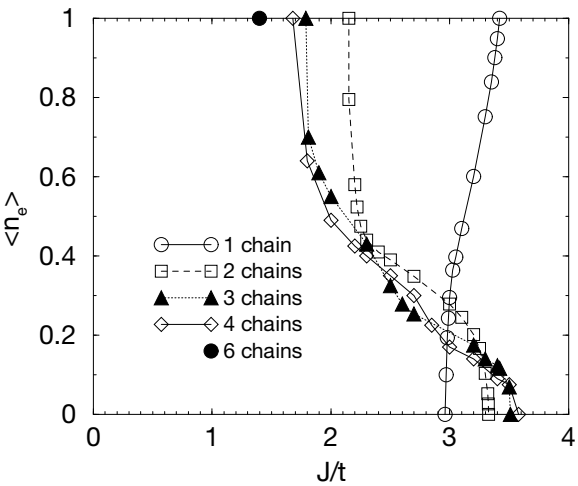

(b) Critical values of exchange rate J and total electron density $\langle n_e \rangle$ for ladders with different number of legs (chains). Phase separation occurs to the right of each line.

Figure 2.4: Phase separation in the t-J model for large J. Results were obtained using DMRG on a lattice with open boundary conditions. From Rommer, White, and Scalapino [43].

The t-J model is a rather crude approximation to the physically motivated Hubbard model, as was shown in section 1.2. There are physical arguments to include next-nearest neighbor hopping and we expect such a term to change the dynamics significantly, especially close to half-filling. **The t-t'-J model** with the additional hopping rate t' is also restricted to the Hilbert space of singly occupied sites but the introduction of an addition parameter makes studying this problem more complex.

The first question when considering the t-t'-J model is whether there is a relative sign for both hopping rates. From band-structure calculations one expects [12] $t' < 0$ in the case of hole doped materials, which we consider, but a positive t' for electron doped materials. While we are not aware of intuitive reasoning for this distinction, it could help explain the asymmetry of the phase diagram in fig. 1.2.

White and Scalapino [12] simulated different lattice geometries for both positive and negative hopping rates t'. While their DMRG calculations for the t-J model always gave a state with stripes running around the cylinder, stripes are suppressed for finite $|t'|$. Ground state occupation numbers and $\hat{S}^z$ expectation values for 12×6 cylinders are shown in fig. 2.5a. The π shifted antiferromagnetic regions begin to merge at $t' = 0.2$ and the state becomes uniform at $t' = 0.3$. In fig. 2.5b one can see that the decay of stripes is qualitatively identical for either sign of t'/t.

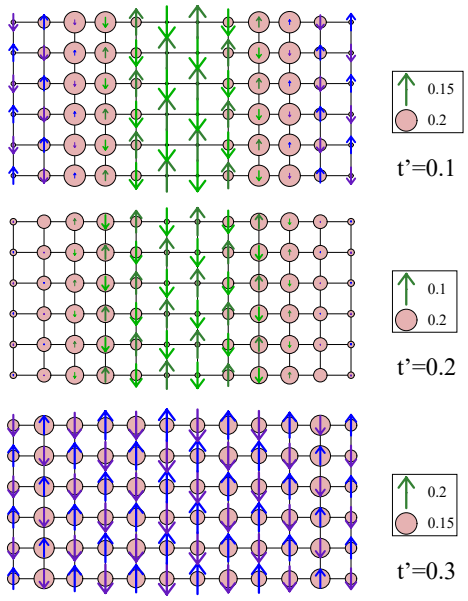

(a) At small t', there are hole-rich domain walls which separate π shifted antiferromagnetic regions. These stripes are reduced as t' increases and one finds a more uniform, antiferromagnetic state.

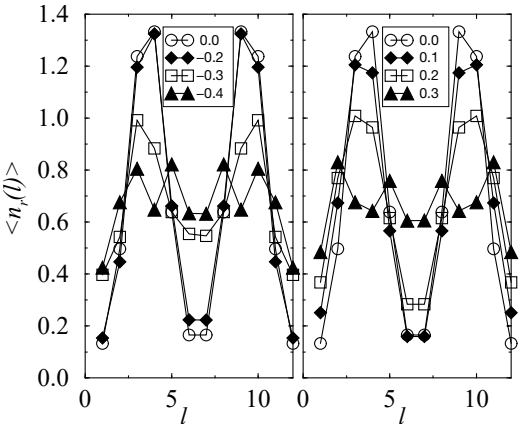

(b) The hole number per ring $\langle n_r \rangle$ shows stripes at $t' = 0$, but they are reduced for finite next-nearest neighbor hopping rates. There is little difference for either sign of t'.

Figure 2.5: Stripes are destabilized for next-nearest neighbor hopping $t' \neq 0$. Results from DMRG simulation with $J/t = 0.5$ for cylindrical boundaries by White and Scalapino [12].

While stripes were found to be destabilized for either sign of t', the ground state has different properties. To classify these states White and Scalapino [12] measured $d_{x^2-y^2}$

pairing correlations (see section 1.4),

$$\hat{\Delta}_{d_{x^2-y^2}}(\boldsymbol{r}) = \frac{\Delta_0}{4}\big[\,(\hat{c}_{\boldsymbol{r}+\boldsymbol{x},\uparrow}\hat{c}_{\boldsymbol{r},\downarrow} - \hat{c}_{\boldsymbol{r}+\boldsymbol{x},\downarrow}\hat{c}_{\boldsymbol{r},\uparrow}) - (\hat{c}_{\boldsymbol{r}+\boldsymbol{y},\uparrow}\hat{c}_{\boldsymbol{r},\downarrow} - \hat{c}_{\boldsymbol{r}+\boldsymbol{y},\downarrow}\hat{c}_{\boldsymbol{r},\uparrow}) + (\hat{c}_{\boldsymbol{r}-\boldsymbol{x},\uparrow}\hat{c}_{\boldsymbol{r},\downarrow} - \hat{c}_{\boldsymbol{r}-\boldsymbol{x},\downarrow}\hat{c}_{\boldsymbol{r},\uparrow}) - (\hat{c}_{\boldsymbol{r}-\boldsymbol{y},\uparrow}\hat{c}_{\boldsymbol{r},\downarrow} - \hat{c}_{\boldsymbol{r}-\boldsymbol{y},\downarrow}\hat{c}_{\boldsymbol{r},\uparrow})\,\big], \tag{2.2}$$

$$D(\boldsymbol{l}) \coloneqq \sum_{\boldsymbol{r}} \left\langle \hat{\Delta}_{d_{x^2-y^2}}(\boldsymbol{r}+\boldsymbol{l})\hat{\Delta}^{\dagger}_{d_{x^2-y^2}}(\boldsymbol{r}) \right\rangle . \tag{2.3}$$

They restricted $\boldsymbol{r}$ to one leg and calculated displacements $\boldsymbol{l}$ along this leg. They found d-wave pairing correlations to be enhanced for positive t'/t, but no such effect exists for $t' < 0$. The influence of t' on $D(\boldsymbol{l})$ and the decay of correlations with spatial distance is shown in fig. 2.6.

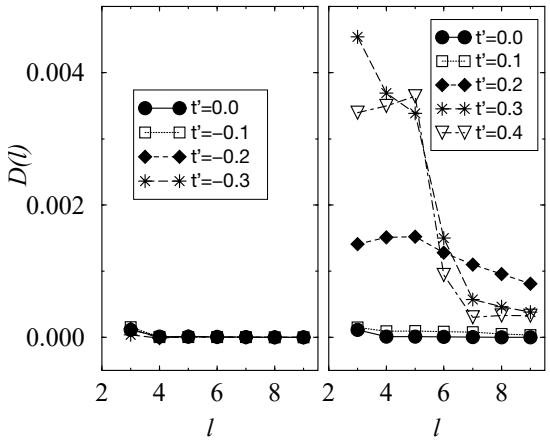

Figure 2.6: d-wave pairing correlations in the t-t'-J model for either sign of t'. Pairing is enhanced for positive t' but there is no such effect for $t' < 0$. DMRG result on a 12×6 cylinder by White and Scalapino [12].

It is somewhat counter-intuitive that $\boldsymbol{t' < 0}$ ***suppresses d*-wave pairing**, as the authors noted. One might think that a hole gaining a relative phase as it hops to a *next*-nearest neighbor site would correspond directly to the $(+-+-)$ phase pattern of the $d_{x^2-y^2}$ symmetry. But this is precisely the point Scalapino and Trugman [26] made and which we discussed in section 1.4: the d-wave phase is present in the pair creation operator, thus the relative sign is between *states* with particle numbers N and $N-2$, respectively. One can therefore interpret this result in such way, that d-wave pairing operators actually create a s-wave symmetric state or, the other way around, that $t' < 0$ favors a $(+-+-)$ phase pattern but therefore suppresses d-wave *pairing*.

Thus, the authors found that both d-wave pairing and stripes are suppressed for negative t'/t. This can also been seen indirectly from the energy per hole for different configurations: in fig. 2.7 systems with one or two holes and stripes are compared. The pair binding energy is commonly defined as

$$E_b = 2E(1\text{ hole}) - E(2\text{ holes}) - E_0, \tag{2.4}$$

which is twice the energy difference between the curve for "1 hole" and "2 holes". One can observe that holes attract[1] each other more strongly with $t' > 0$ and that pairing becomes more favorable than a striped state. As stripes barely interact with each other, the

[1] *Attraction* in the sense of a negative contribution to the energy. It does not imply spatial attraction as e.g. BCS pairs are non-local.

energy per hole for a striped state is only weakly dependent on doping x for $x \lesssim 0.15$ [38]. For negative next-nearest neighbor hopping the energy per hole is constant with doping, meaning that there is no measurable interaction between holes. The striped state becomes least favorable.

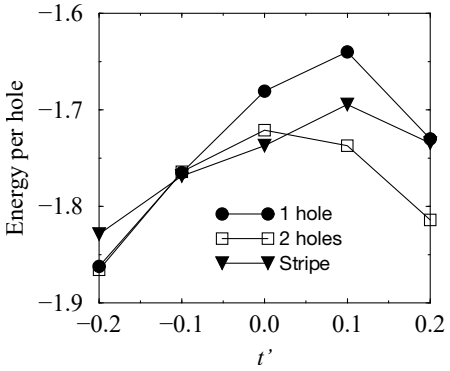

Figure 2.7: Energy per hole, compared for a single hole, a pair of holes and stripes. Different values of t' in the t-t'-J model are shown. From White and Scalapino [12].

Further attempts to find states which allow for both striped phases and pairing have been made. White and Scalapino [44] simulated the t-t'-J on different lattice geometries and measured expectation values of pairing operators,

$$\hat{\Delta}_{\boldsymbol{r},\boldsymbol{r'}} = \Delta_0 \left(\hat{c}_{\boldsymbol{r},\uparrow}\hat{c}_{\boldsymbol{r'},\downarrow} + \hat{c}_{\boldsymbol{r'},\uparrow}\hat{c}_{\boldsymbol{r},\downarrow}\right), \tag{2.5}$$

on bonds between adjacent sites. As these operators do not conserve particle number, one cannot restrict the calculation to a subspace of well defined particle number but requires a chemical potential to control doping. Thus, larger bond dimensions for the MPS state are necessary and computations are more difficult. To explicitly break the symmetry, they did not only apply staggered magnetic fields on the open boundaries, but also pair fields $\hat{D}_{\boldsymbol{r},\boldsymbol{r'}}$ with different amplitudes on selected bonds,

$$\hat{D}_{\boldsymbol{r},\boldsymbol{r'}} \coloneqq \frac{1}{2}\left(\hat{\Delta}^{\dagger}_{\boldsymbol{r},\boldsymbol{r'}} + \hat{\Delta}_{\boldsymbol{r},\boldsymbol{r'}}\right). \tag{2.6}$$

They were able to stabilize stripes with a finite pair field response, as shown in figs. 2.8a and 2.8b for a cylindric 12×8 system. We note that this simulation was actually for the t-J model, i.e. $t' = 0$. This is due to the computational difficulty of the problem: White and Scalapino [44] used bond dimensions $m \approx 3000 \ldots 6000$ for the simulations which might barely be sufficient to describe systems of such size.

For their further simulations with $t' \neq 0$ they considered slimmer systems of width $w = 5$ with open boundaries. They applied a staggered magnetic field along one outer leg and a pair field along four bounds on rungs close to one boundary. Furthermore, the chemical potential was varied to control the doping.

They observed how pairing depends on next-nearest neighbor hopping t' and doping, the results are shown in fig. 2.9. As it was expected from their older paper, pairing is enhanced for positive t' but suppressed for $t'/t < 0$. One can also observe that pairing is stronger for larger exchange rates—"usually" values of $J/t = 0.3$ are chosen to represent cuprates (compare White and Scalapino [44]), for $J/t = 0.5$ there might already be separation of phases, as we discussed before.

The curves might indicate that the ideal filling for stripes in a pairing field depends on t'/t but we do not consider the data to be conclusive. Eventually, these simulations show

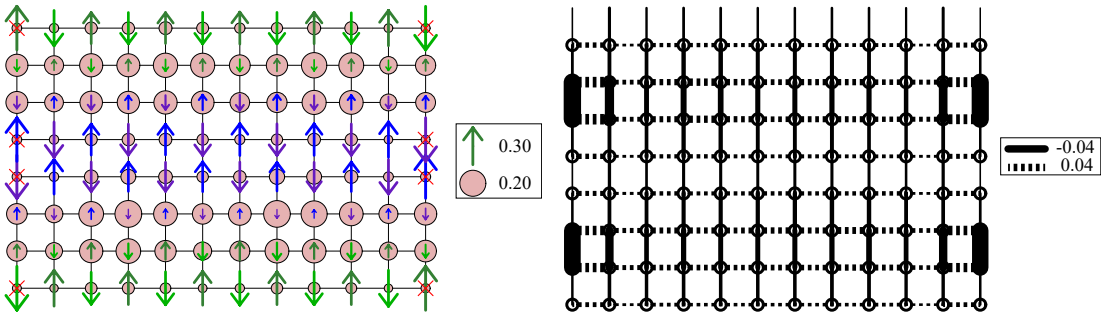

(a) Hole densities are expressed by circle diameter and spin expectation values by arrow length and direction. There is a staggered magnetic field $h = \pm 0.2$ applied on sites at the open ends, denoted by a red 'X'.

(b) Expectation value of the pair field $\langle \hat{D}_{\boldsymbol{r},\boldsymbol{r}'} \rangle$ evaluated on nearest neighbor bonds. Fields with strength $\Delta_0 = 1$ (0.5) have been applied at four bounds on the open ends (four bonds adjacent to open ends), denoted by the thickest solid lines.

Figure 2.8: Pairing and stripes in the t-J model on a 12×8 cylinder. Anisotropic exchange rates $J_x = 0.55$, $J_y = 0.45$ were chosen to favor horizontal stripes and to enhance pairing. From White and Scalapino [44].

that stripes and pairing can be *stabilized* for some values of $t'$and J. However, the system strongly depends on these parameters. But as very special boundary conditions on rather small lattices are required it is not at all clear if these states actually describe the ground state of the t-t'-J model.

So far we have considered approximations to the **two-dimensional Fermi-Hubbard model**. We have seen that the ground-state is made up from d-wave pairs or stripes and might exhibit phase separation. However, after about 25 years of research, technological and algorithmic development not even the ground state of the most "simple" t-J model is known definitely. The Hubbard model is more difficult to study numerically: its local dimension is larger since double occupation is possible and thus it allows for much more dynamics close half filling. This could be reproduced by effective long range interactions, i.e. $(\text{next})^n$-nearest neighbor hopping terms in t-t'-$\ldots$-J model—but long range terms might be relevant at low doping. It is not clear to us for which cases effective strong coupling models describe the same physics as the Hubbard model. However, if there are effects like stripes, phase separation or $d_{x^2-y^2}$ pairing present in the Hubbard model, we assume that we can observe them in the same way as for approximate Hamiltonians.

There are only few reliable results for the two-dimensional Hubbard model, especially at strong interaction and small but finite doping. We had mentioned the review paper by the Simons foundation [34] which gives benchmark results from the most relevant numerical methods. We will use their results to compare them with our approach in section 4.1.1. The authors however hardly consider physical properties of the ground state: not all methods can access the same observables such that comparison would be more difficult. Ground state methods like DMRG work by minimizing the state's energy and thus seem to converge well in terms of energy, while other observables are not necessarily as well behaved. Therefore, also extrapolation to the "accurate" and infinite size limit can be more difficult for physical quantities other than energy.

We want to stress that extrapolation is a delicate task—but it is crucial to achieve good results even for quantities as the energy. For the case of iPEPS calculations, this was recently shown by Corboz [45]. Although iPEPS describes an infinite system, i.e. extrapolation in length and width is not necessary, any state is approximated by a two-dimensional tensor network with finitely many parameters which can only approximate the true ground state.

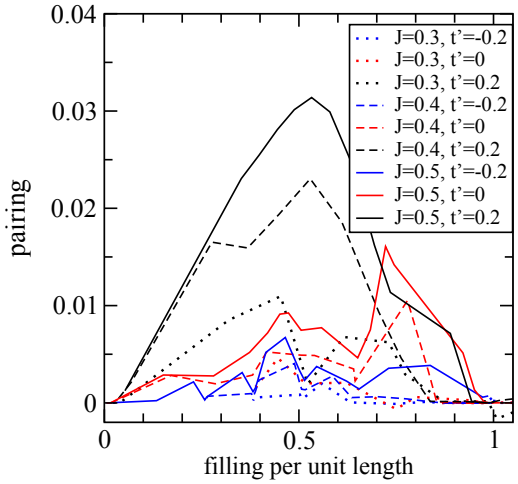

Figure 2.9: The pair field response measured on a bond on the 12^{th} rung in the hole-rich stripe. Calculations were performed on a 16×5 site lattice with open boundaries and a staggered magnetic field to form a hole-rich stripe on second and third leg. 'Filling per unit length' is the average hole number per rung and varied by changing the chemical potential. From White and Scalapino [44].

As the approximation becomes more precise with increasing tensor bond dimension D, one might extrapolate physical quantities in $1/D$ to find an estimate for the exact state. However, there is not necessarily a clear dependence on $1/D$ as shown for the Hubbard model in fig. 2.10a. Corboz [45] instead considers the *truncation error* w which is introduced in each simulation step: a single tensor is evolved by applying a matrix product operator to it, eventually yielding the updated tensor. This procedure however increases the tensor's size exponentially and thus truncation is necessary in each step. The energy versus truncated weights w is also shown in fig. 2.10—the curves are smoother and can be fitted with a third order polynomial. On a side note, these plots indicate that the ground state of the doped Hubbard model is more difficult to describe: while at half-filling we always have $w < 1/D$, the truncation error for the doped system is roughly $w \approx 2/D$, significantly larger than $1/D$ for all points[2].

Further, we want to discuss a paper by White and Scalapino [46] who observed stripes in the Hubbard model, much like they did for t-(t'-)J models. They performed DMRG calculations on a 7×6 cylinder with maximal bond dimensions $m \approx 4000 \ldots 7500$. The odd length was chosen to favor the formation of a single stripe, while an even length, at least for periodic boundary conditions, is said to frustrate the formation of a stripe. They chose interaction strengths $U = 3 \ldots 12$ and put 4 holes into the system, corresponding to $n = 0.905$.

For all interaction strengths they found density profiles as depicted in fig. 2.11a which remind of stripes we had observed in the t-t'-J model, see figs. 2.1, 2.5a and 2.8a—except for the fact that the stripe in the Hubbard model is centered at a site and not a bond. White and Scalapino [46] started from a state with two separated pairs of holes. As the bond dimension is increased, see fig. 2.11b, pairs merge into a single stripe. The fact that DMRG "tunnels" between these states which are not related only through local changes makes the

[2]The reader of this paper might have noticed that $w \approx 2/D$ is also true in the noninteracting case, $U = 0$. Our statement is therefore only that some state is difficult to describe *in a given basis*—a better choice of basis could greatly simplify it.

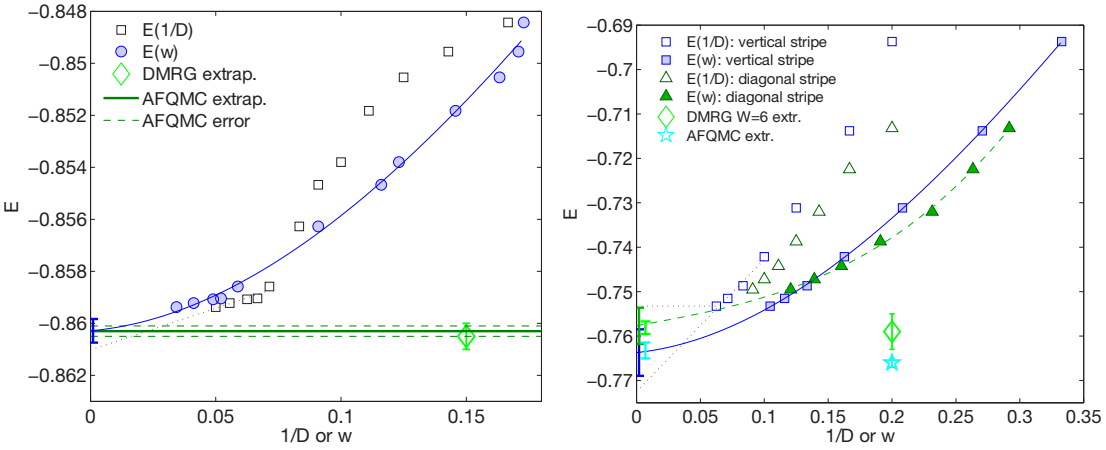

(a) Using the truncation error gives a smoother curve and allows for more reasonable extrapolation to the exact state. There is good agreement with DMRG and auxiliary-field quantum Monte Carlo (AFQMC). The latter is considered to be the benchmark result at half-filling as there is no sign problem.

(b) The doped state at $n = 7/8$ is more difficult to compute, the error bars for all methods are much larger. An extrapolation in the reciprocal bond dimension $1/D$ would probably underestimate the system's energy.

Figure 2.10: Energy extrapolation for iPEPS in the 2D Hubbard model at $U = 4$ (a) and $U = 8$ (b). Energy per site is plotted versus reciprocal bond dimension $1/D$ and truncation error w, respectively. From Corboz [45].

statement, that the stripe is energetically favorable, more robust. Unlike for many of their t-J calculations, they did not apply external fields to enhance antiferromagnetic order.

As the system length is rather short, the influence of the cylinder's open ends has to be considered: open ends generally attract electrons and thus cause Friedel oscillations (see e.g. Bedürftig et al. [47]). White and Scalapino [46] argue that the stripes they observed in longer t-J cylinders are not just due to the open ends for the following reasons:

- For longer systems, the amplitude does not decay away from the end—Friedel oscillations should decay polynomially [47].
- The oscillations at fixed width barely depend on system length.
- Anisotropic exchange rates $J_{x,y}$ cause similar, but *longitudinal* stripes.

After this chapter had been completed thus far, a paper was published by Ehlers, White, and Noack [48] on the DMRG results for the Fermi-Hubbard model at $n = 7/8$. In order to overcome limitations of DMRG in system *width*, they use the same approach as we do and transform the system in mixed real and momentum space (see section 3.3.1). They can therefore exploit quasi-momentum conservation as an additional symmetry and achieve larger MPS bond dimensions as the matrices become more sparse.

Ehlers, White, and Noack [48] were able to achieve to find lower energies than the real space simulations we discussed before. An in depth comparison of energies calculated by this paper, by LeBlanc et al. [34] and by us is presented in section 4.1.1. We will therefore not discuss these results here.

Furthermore, Ehlers, White, and Noack [48] tried to answer the question of stripe formation. They were able to *stabilize* stripes of wavelength $\lambda = 8.0$ and $\lambda = 5.3$ as shown in fig. 2.12a. Using hybrid space DMRG they can simulation cylinder widths of $w = 4$ and $w = 6$. However convergence is apparently hard to achieve for the wider system: in fig. 2.12a

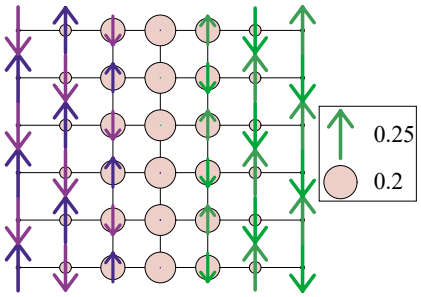

(a) Antiferromagnetic regions with a relative π shift at the open ends, a hole-rich domain wall in the center—the phenomenology is comparable to stripes observed in the t-J model. Note that the stripe is site-centered while it was bond-centered for all previous diagrams.

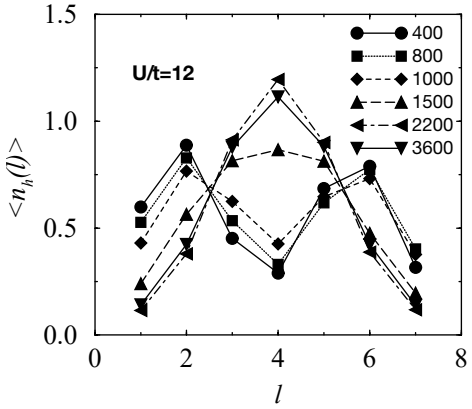

(b) The number of holes per cylinder ring for different stages of the calculations, i.e. different bond dimensions m. The two hole pairs which were separated initially merge into one stripe at dimension $m = 1500$.

Figure 2.11: The ground state of a 7×6 Hubbard cylinder at interaction $U = 12$. DMRG calculation by White and Scalapino [46].

one can see gray curves which are what they actually measured and black ones which are extrapolated to zero truncation error. For $w = 4$ they agree reasonably well, but there are quite some differences for the $\lambda = 8.0$ system of width $w = 6$.

It appears that the amplitude of "stripes" increases as the system gets wider, making it plausible that stripes are present in the thermodynamic limit. However, Ehlers, White, and Noack [48] do not find a clear dependence of stripe amplitude on cylinder length, as shown in fig. 2.12b.

Ehlers, White, and Noack [48] also measure correlator for particle densities, spin and pairing-fields. We show their results in fig. 2.13. We are unable to compare directly to their results as spin and pair-field observables are not $SU(2)$ invariant and we cannot measure them. However, qualitatively their results agree with ours, which we will discuss in section 4.2: they find exponential decay on what appears to be two different length scales. Although one might assume to find longer range order if there are periodic stripes, the authors conclude that stripes, in particular at $\lambda = 8.0$ are a robust feature of the ground state of the Hubbard model and thus likely also present in the thermodynamic limit.

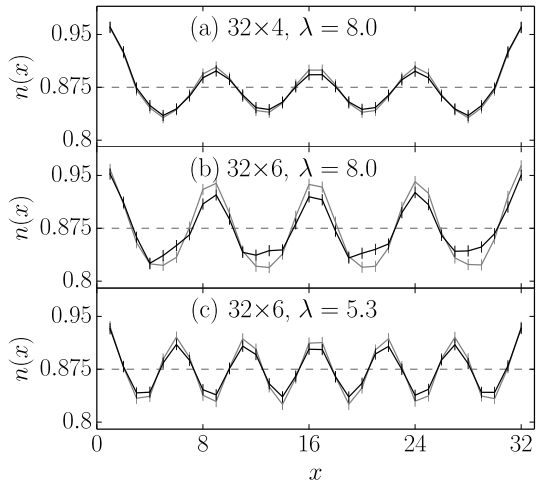

(a) Stripes for on different lattice sizes. Two wavelengths could be stabilized. Black lines are extrapolated density profiles to zero truncation error, gray curves are the best variational results.

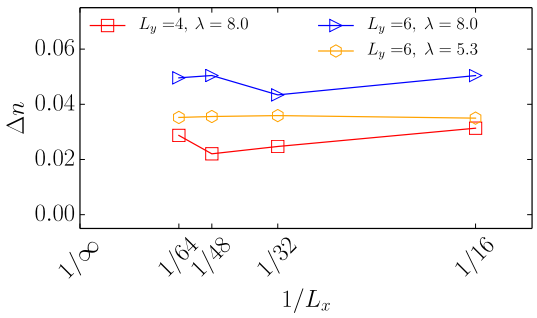

(b) Amplitude for stripes shown in fig. 2.12a for different system sizes. The oscillation seems to be stronger for the wider cylinder but there is little dependence on system length.

Figure 2.12: Stripes in the doped $n = 7/8$, strongly interacting $U = 8$ Hubbard model. Hybrid space DMRG calculations from Ehlers, White, and Noack [48].

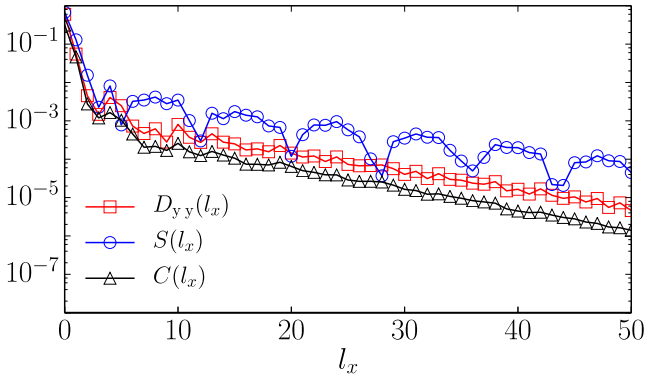

Figure 2.13: Pair-field D_{yy}, spin S and charge C correlators for the doped $n = 7/8$ Hubbard model with intermediate interaction $U = 4$. All correlations decay exponentially but at different rates. The decay is particularly fast over the first ≈ 5 sites. Spin correlations show a periodic modulation, the other curves are rather flat. Hybrid space DMRG results from Ehlers, White, and Noack [48]

3 The DMRG algorithm in hybrid space

In this chapter we want to explain the numerical methods used in this thesis. We will start by defining *matrix product states* (MPS) which are, broadly speaking, a generalization of product states—however, they are dense in the full Hilbert space. We will show that numerical computations can be performed efficiently on these states and explain why MPS are particularly useful to describe ground states with low entanglement. Matrix product states can be constructed such that they transform according to a given symmetry sector. We will show how we can enforce symmetries to make computations more efficient.

We will then explain the DMRG algorithm in the language of matrix product states, in which it appears most natural. This description will be based on a review by Schollwöck [49] but we will try to keep it brief. The improved, *single site* DMRG algorithm used for our calculations will also be outlined.

Lastly, we consider our approach to simulating two dimensional systems with DMRG. The implementation of momentum conservation along the rings of cylindric systems as an additional symmetry will be explained. The thus constructed one-dimensional chain of *matrix product operators* (MPO) is inhomogeneous—we will discuss the influence of different 2D $\rightarrow$ 1D mappings computational efficiency.

3.1 Matrix product states

Any state of a quantum many body system on a lattice can be written in terms of *local basis states*. We consider a system made up from Hilbert spaces $\mathcal{H}_i$ at site $i \leq l$ which is spanned by a complete local basis $\{|\sigma_{i,1}\rangle, |\sigma_{i,2}\rangle, \dots\}$,

$$\mathcal{H} = \bigotimes_{i=1}^{l} \mathcal{H}_i, \tag{3.1}$$

$$\mathcal{H}_i = \operatorname{span}\left(\{|\sigma_i\rangle\}\right). \tag{3.2}$$

A state in the entire Hilbert space $\mathcal{H}$ can thus be written as a sum of tensor products of local basis vectors,

$$|\psi\rangle = \sum_{\sigma_1,\dots,\sigma_l} c^{\sigma_1,\dots\sigma_l} |\sigma_1\rangle \otimes \cdots \otimes |\sigma_l\rangle \equiv \sum_{\boldsymbol{\sigma}} c^{\boldsymbol{\sigma}} |\boldsymbol{\sigma}\rangle \in \mathcal{H}, \tag{3.3}$$

where we have introduced the state $|\boldsymbol{\sigma}\rangle$ as tensor product of all local basis states. The coefficients $c^{\sigma_1,\dots\sigma_l}$ are complex and only need to fulfill the constraint that $|\psi\rangle$ is normalized,

$$\sum_{\boldsymbol{\sigma}} |c^{\boldsymbol{\sigma}}|^2 = 1. \tag{3.4}$$

We can thus interpret the coefficients $c^{\boldsymbol{\sigma}}$ as a tensor[1] of rank l with dimensions $\{d_i\}$. We depict such a tensor graphically in fig. 3.1, each of the legs corresponds to the physical state $|\sigma_i\rangle$ at site i.

[1] For now a "tensor" is just a higher dimensional array, without any special transformation properties.

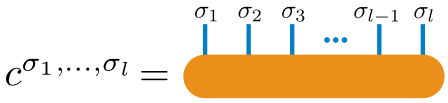

Figure 3.1: Graphical representation of a coefficient tensor in terms of local states $|\sigma_i\rangle$.

Thus, there are $\prod_i d_i$ many complex numbers[2] required to describe a "typical" many body state. As the number of parameters thus growths exponentially with system size, calculations with such states are generally impossible. Instead, one frequently considers product states,

$$|\psi_{\text{product}}\rangle = \sum_{\boldsymbol{\sigma}} c^{\sigma_1} c^{\sigma_2} \cdots c^{\sigma_l} |\boldsymbol{\sigma}\rangle = \sum_{\sigma_1} c^{\sigma_1} |\sigma_1\rangle \otimes \cdots \otimes \sum_{\sigma_l} c^{\sigma_l} |\sigma_l\rangle \,. \tag{3.5}$$

While these states can be handled easily, they cannot encode correlations, i.e. entanglement, between different sites—thus they are generally useless to describe *strongly interacting* systems.

This is where ***matrix* product states** (MPS) come into play. The idea is to generalize the *scalar* coefficients c_{σ_i} in eq. (3.5) to matrices A^{σ_1},

$$\begin{aligned} |\psi_{\text{MPS}}\rangle = \sum_{\boldsymbol{\sigma}} A^{\sigma_1} A^{\sigma_2} \cdots A^{\sigma_l} |\boldsymbol{\sigma}\rangle \,, \\ A^{\sigma_i} \in \mathcal{M}(m_{i-1} \times m_i,\ \mathbb{C}), \end{aligned} \tag{3.6}$$

where we will call m_i the *bond dimension* between sites i and $i+1$. In this way we can describe states with $\mathcal{O}\left(\sum_i m_{i-1} \cdot m_i\right)$ many parameters[3] which, at fixed m, increases only *linearly* in system size. However, we can still encode correlations of local observables: e.g. the maximally entangled singlet state of two spins,

$$\begin{aligned} \left(A^{\uparrow_1}\right)^\top = A^{\downarrow_2} = \frac{1}{2^{1/4}} \begin{pmatrix} 1 \\ 0 \end{pmatrix}, \qquad & \left(A^{\downarrow_1}\right)^\top = -A^{\uparrow_2} = \frac{1}{2^{1/4}} \begin{pmatrix} 0 \\ 1 \end{pmatrix}, \\ c^{\uparrow,\uparrow} = A^{\uparrow_1} A^{\uparrow_2} = 0, \qquad & c^{\downarrow,\downarrow} = A^{\downarrow_1} A^{\downarrow_2} = 0, \\ c^{\uparrow,\downarrow} = A^{\uparrow_1} A^{\downarrow_2} = \frac{1}{\sqrt{2}}, \qquad & c^{\downarrow,\uparrow} = A^{\downarrow_1} A^{\uparrow_2} = -\frac{1}{\sqrt{2}}. \end{aligned} \tag{3.7}$$

Matrix product states are actually dense in the Hilbert space $\mathcal{H}$ for arbitrarily large bond dimensions m_i [40]. We can construct an MPS representation for any state using *singular value decomposition* and we can find "good" approximations at finite bond dimensions m using *truncation*.

3.1.1 Singular value decomposition

The singular value decomposition (SVD) is a very basic "tool" of linear algebra as seen as a generalization of eigenvalue decomposition. But it is also very useful for quantum physics: in the next subsection we will see how it is related to Schmidt coefficients and entanglement.

Any matrix $M \in \mathcal{M}(N_A \times N_B, \mathbb{C})$ can be decomposed as

$$M = USV^\dagger, \tag{3.8}$$

[2] There are constraints due to normalization but a single condition does not change much.
[3] Eventually, the state needs to be normalized and there is a gauge freedom at each bond which we will use to make tensors left- and right-normalized. Therefore, the number of *free* parameters is smaller.

where:
- $U \in \mathcal{M}(N_A \times \min(N_A, N_B),\ \mathbb{C})$ has orthonormal *column* vectors, $U^\dagger U = \mathbb{1}$.
- $S \in \mathcal{M}(\min(N_A, N_B) \times \min(N_A, N_B),\ \mathbb{R}_0^+)$ is diagonal with positive singular values s_a, $S_{a,b} = \delta_{a,b} s_a$.
- $V^\dagger \in \mathcal{M}(\min(N_A, N_B) \times N_B,\ \mathbb{C})$ has orthonormal *row* vectors, $V^\dagger V = \mathbb{1}$.

Only if U ($V^\dagger$) is a square matrix it is also *unitary*, $UU^\dagger = \mathbb{1}$ ($VV^\dagger = \mathbb{1}$).

Using SVD we can represent an arbitrary quantum state, defined through its coefficient tensor $c^{\sigma_1,\ldots,\sigma_l}$, as matrix product state. We start by *reshaping* the tensor into a matrix $c^{\sigma_1,(\sigma_2,\ldots,\sigma_l)}$ as shown in the upper left of fig. 3.2. We can decompose this matrix as,

$$c^{\sigma_1,(\sigma_2,\ldots,\sigma_l)} = \sum_{\alpha_1} U^{\sigma_1,\alpha_1} S_{\alpha_1}{}^{\alpha_1} (V^\dagger)_{\alpha_1}{}^{(\sigma_2,\ldots,\sigma_l)} \equiv A^{\sigma_1} c^{(\sigma_2,\ldots,\sigma_l)}, \tag{3.9}$$

$$A^{\sigma_1,\alpha_1} := U^{\sigma_1}{}_{\alpha_1} \quad \text{and} \quad c_{\alpha_1}{}^{(\sigma_2,\ldots,\sigma_l)} := S_{\alpha_1}{}^{\alpha_1} (V^\dagger)_{\alpha_1}{}^{(\sigma_2,\ldots,\sigma_l)} \tag{3.10}$$

where we have written the matrix product explicitly for the intermediate step. A^{σ_1} is the first MPS tensor we are looking for and we can continue by reshaping the $c_{\alpha_1}{}^{(\sigma_2,\ldots,\sigma_l)}$ "matrix",

$$c_{(\alpha_1}{}^{\sigma_2)(\sigma_3,\ldots,\sigma_l)} = \sum_{\alpha_2} U_{(\alpha_1}{}^{\sigma_2),\alpha_2} S_{\alpha_2}{}^{\alpha_2} (V^\dagger)_{\alpha_2}{}^{(\sigma_3,\ldots,\sigma_l)} \equiv A_{\alpha_1}{}^{\sigma_2} c^{(\sigma_3,\ldots,\sigma_l)} \tag{3.11}$$

$$A_{\alpha_1}{}^{\sigma_1,\alpha_2} := U_{\alpha_1}{}^{\sigma_1,\alpha_2} \quad \text{and} \quad c_{\alpha_2}{}^{(\sigma_3,\ldots,\sigma_l)} := S_{\alpha_2}{}^{\alpha_2} (V^\dagger)_{\alpha_2}{}^{(\sigma_3,\ldots,\sigma_l)} \tag{3.12}$$

and decomposing it as shown in the middle row fig. 3.2.

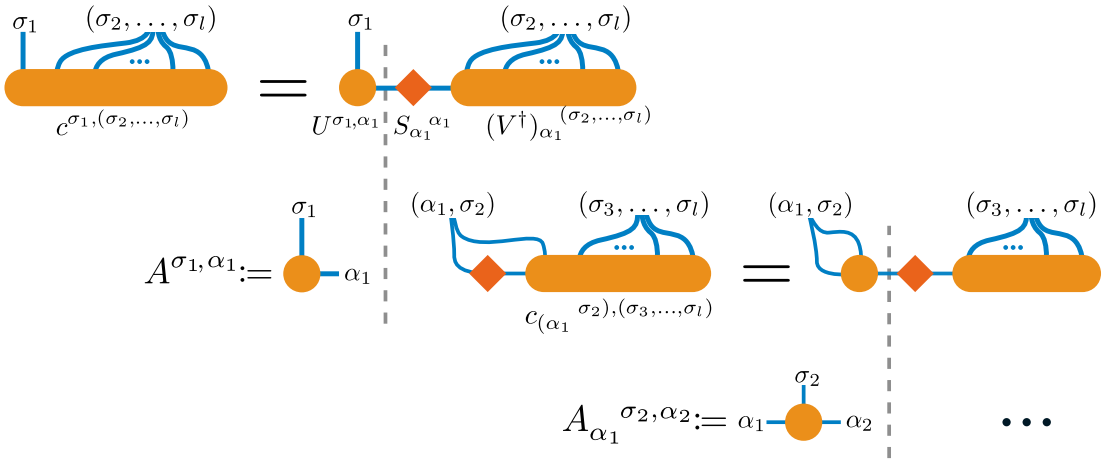

Figure 3.2: Creating a matrix product state from an arbitrary coefficient tensor using SVD. Starting from a rank l tensor as in fig. 3.1 we can *reshape* the tensors into matrices by combining legs and then perform singular value decomposition. As we split the indices again, we find rank three tensors $A^{\alpha_{i-1},\sigma_i}{}_{\alpha_i}$ and we can thus write the coefficients as MPS, depicted in fig. 3.3.

We can continue to do so and arrive at rank three MPS tensors $A^{\alpha_{i-1},\sigma_i}{}_{\alpha_i}$ for all $1 < i < l$. At the end we find a matrix

$$A_{\alpha_{l-1}}{}^{\sigma_l} := S_{\alpha_{l-1}}{}^{\alpha_{l-1}} (V^\dagger)_{\alpha_{l-1}}{}^{\sigma_l}. \tag{3.13}$$

By contracting all tensors along their *correlation legs* α_i as shown in fig. 3.3 we precisely restore the coefficients of ψ and thus the original state $|\psi\rangle$.

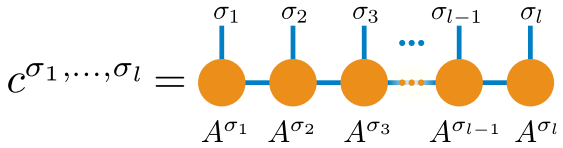

Figure 3.3: Coefficients of a quantum state decomposed into a MPS chain. The horizontal blue bonds indicate contraction over the correlation legs α_i.

The tensors $A_{(\alpha_{i-1}}{}^{\sigma_i),\alpha_i}$, $i < l$ were defined such that they have orthonormal column vectors. If we contract α_{i-1}, σ_i with the complex conjugated MPS tensor, we will therefore find the identity operator,

$$\sum_{\alpha_{i-1},\sigma_i} \left(A_{\alpha_{i-1}}{}^{\sigma_i,\alpha_i}\right)^\dagger A_{\alpha_{i-1}}{}^{\sigma_i,\alpha_i} = \delta_{\alpha_i}{}^{\alpha_i} = \mathbb{1}. \tag{3.14}$$

Such tensors are thus called *left-normalized* and can greatly simplify the contraction of a tensor network. If we contract all tensors A^{σ_i}, $i < j$ left to some site j with their respective complex conjugate, they reduce to the identity. This is shown in fig. 3.4 and it does not only reduce computational cost but also increases numerical stability.

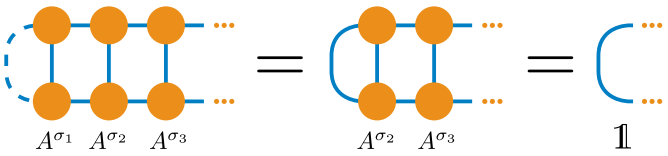

Figure 3.4: Contracting left-normalized tensors with their complex conjugate, $(A^{\sigma_i})^\dagger A^{\sigma_i}$ yields the identity. The dashed line indicates a bond of dimension 1.

Conversely, we could have started from the rightmost leg σ_l and defined our MPS tensors B^{σ_i} such that they have orthonormal *rows*,

$$\begin{aligned} c^{(\sigma_1,\ldots,\sigma_{i-1}),(\sigma_i,\alpha_i)} &= \sum_{\alpha_{i-1}} U^{(\sigma_1,\ldots,\sigma_{i-1}),\alpha_{i-1}} S_{\alpha_{i-1}}{}^{\alpha_{i-1}} (V^\dagger)_{\alpha_{i-1}}{}^{(\sigma_i,\alpha_i)} \\ &\equiv c^{(\sigma_1,\ldots,\sigma_{i-1})} B^{(\sigma_i,\alpha_i)}, \end{aligned} \tag{3.15}$$

$$\begin{aligned} \text{where} \qquad B_{\alpha_{i-1}}{}^{\sigma_i,\alpha_i} &:= (V^\dagger)_{\alpha_{i-1}}{}^{(\sigma_i,\alpha_i)}, \\ c^{(\sigma_1,\ldots,\sigma_{i-1}),\alpha_{i-1}} &:= U^{(\sigma_1,\ldots,\sigma_{i-1}),\alpha_{i-1}} S_{\alpha_{i-1}}{}^{\alpha_{i-1}}, \end{aligned} \tag{3.16}$$

and thus arrive at *right*-normalized tensors such that contractions from the right end,

$$\sum_{\sigma_i,\alpha_i} B_{\alpha_{i-1}}{}^{\sigma_i,\alpha_i} \left(B_{\alpha_{i-1}}{}^{\sigma_i,\alpha_i}\right)^\dagger = \mathbb{1}, \tag{3.17}$$

yield the identity operator. We note that the "last" tensor is different and thus not normalized by construction. However, this last contraction correspond to taking the two norm of the coefficients— $\sum_{\boldsymbol{\sigma}} |c^{\boldsymbol{\sigma}}|^2 = 1$ for any normalized state. Furthermore, it is also possible to represent states with both left- and right-normalized tensors—however, there will always be at least one tensor in between, which has neither normalization. This "mixed-canonical" representation is very useful to normalize a state after changing only one MPS tensor or to calculate local observables as shown in fig. 3.5

We have seen that *any* state can be expressed as matrix product state. But why should we do so? The bond dimensions m_i of the correlation legs α_i are generally of size $\prod_{j<i} d_j$ such that the number of parameters still grows exponential in system size. Also, the costs for singular value decomposition, which for $m \times n$ matrices scales as $\mathcal{O}(\min(m,n)^2 \cdot \max(m,n))$, still grows exponentially. It seems we have introduced a very cumbersome notation without gaining anything worthwhile.

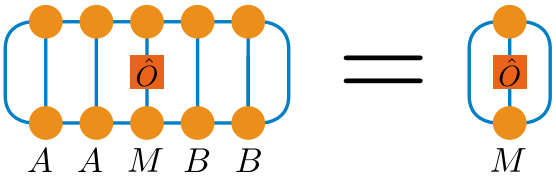

Figure 3.5: Calculation of local observables in mixed canonical representation. If all tensors to the right (left) are right(left)-normalized, local expectation values can be evaluated by contracting three tensors. Note that most observables are usually rather of rank 4 with legs on left- and right side.

3.1.2 Entanglement

We started motivating MPS by building upon product states. The latter are in some sense classical as there cannot be any entanglement between its subsystems. If we consider a bipartite system,

$$\mathcal{H} = \mathcal{H}_A \otimes \mathcal{H}_B, \tag{3.18}$$

any state ψ can be written as a *Schmidt decomposition* into vectors $|\alpha\rangle$ in $\mathcal{H}_A$ and $|\beta\rangle \in \mathcal{H}_B$,

$$\begin{aligned} \mathcal{H} \ni |\psi\rangle &= \sum_i s_i \, |\alpha_i\rangle \otimes |\beta_i\rangle \,, \\ \delta_{i,j} &= \langle \alpha_i | \alpha_j \rangle = \langle \beta_i | \beta_j \rangle \,, \end{aligned} \tag{3.19}$$

where s_i are called the Schmidt coefficients. A product state could be expressed with exactly one finite Schmidt number; in general the coefficients can be chosen real and non-negative and need to fulfill normalization,

$$\langle \psi | \psi \rangle = \sum_i |s_i|^2 = 1. \tag{3.20}$$

The *entanglement entropy*[4] of one part with the other is thus given by

$$S(A) = S(B) = -\sum_i |s_i|^2 \log |s_i|^2. \tag{3.21}$$

This means if the entropy is smaller, the spectrum of Schmidt coefficients decays faster to zero.

But the Schmidt decomposition into A and B is precisely the same as an SVD on the bond separating both subsystems. We can write any state as MPS and thus arrive at a form

$$|\psi\rangle = \sum_{\boldsymbol{\sigma}} \sum_{\alpha_i} \cdots A^{\sigma_{i-1}} A^{\sigma_i, \alpha_i} S_{\alpha_i}{}^{\alpha_i} B_{\alpha_i}{}^{\sigma_{i+1}} B^{\sigma_{i+2}} \cdots |\boldsymbol{\sigma}\rangle \,, \tag{3.22}$$

graphically depicted in fig. 3.6. We can reorder the sums to arrive at the more instructive form,

[4] This is the same as the von Neumann entropy of the reduced density matrix—which we will use in eq. (3.55).

$$|\psi\rangle = \sum_{\alpha_i} S_{\alpha_i}{}^{\alpha_i} \underbrace{\left(\sum_{\sigma_1,\ldots,\sigma_i} A^{\sigma_1} \cdots A^{\sigma_i,\alpha_i} |\sigma_1,\ldots,\sigma_i\rangle \right)}_{\left|\psi_A{}^{\alpha_i}\right\rangle \in \mathcal{H}_A} \otimes \underbrace{\left(\sum_{\sigma_{i+1},\ldots,\sigma_l} B_{\alpha_i}{}^{\sigma_{i+1}} \cdots B^{\sigma_l} |\sigma_{i+1},\ldots,\sigma_l\rangle \right)}_{\left|\psi_{B,\alpha_i}\right\rangle \in \mathcal{H}_B}. \tag{3.23}$$

Due to left-(right-)normalization of the A (B) tensors the vectors $|\psi_A{}^{\alpha_i}\rangle$ ($|\psi_{B,\alpha_i}\rangle$) are also orthonormal. If one contracts from the left as graphically represented in fig. 3.4, we find

$$\langle \psi_A{}^{\alpha_i} | \psi_A{}^{\alpha_j} \rangle = \sum_{\sigma_i} \left(A^{\sigma_i,\alpha_i}\right)^\dagger A^{\sigma_i,\alpha_j} = \delta_{\alpha_i}{}^{\alpha_j}, \tag{3.24}$$

which precisely the condition of A having orthonormal column vectors.

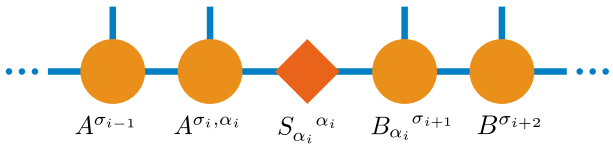

Figure 3.6: An MPS corresponding to the Schmidt decomposition of a bipartite system.

This equivalence of singular value and Schmidt decomposition means that *if* a subsystem has low entanglement, there are only few "significant" Schmidt coefficients and thus only few "large" singular values. We can therefore try to *approximate* such states with *truncated* correlation bonds to keep the MPS tensors manageable.

As all singular values $S_{\alpha_i}{}^{\alpha_i}$ are semi-positive, we can define a *truncation threshold* t and only consider indices β_i for which we find $S_{\beta_i}{}^{\beta_i} > t$. Approximating the state $|\psi\rangle$ in such way by $|\psi'\rangle$ we introduce an error,

$$\begin{aligned} \epsilon^2 = \| \, |\psi\rangle - |\psi'\rangle \, \|^2 &= \left\| \sum_{\alpha_i} S_{\alpha_i}{}^{\alpha_i} |\psi_A{}^{\alpha_i}\rangle \otimes |\psi_{B,\alpha_i}\rangle - \sum_{\beta_i} S_{\beta_i}{}^{\beta_i} \left|\psi_A{}^{\beta_i}\right\rangle \otimes |\psi_{B,\beta_i}\rangle \right\|^2 \\ &= \sum_{\alpha_i \notin \{\beta_i\}} \left(S_{\alpha_i}{}^{\alpha_i}\right)^2 \leq \left(|\{\alpha_i\}| - |\{\beta_i\}|\right) t^2. \end{aligned} \tag{3.25}$$

The truncation of singular values is thus the best approximation of the bipartite state in the two norm.

We are very lucky that states of low entanglement are actually important for physical systems such that **MPS works well** in many cases. The textbook example would be the *AKLT* state (see Schollwöck [49]). The Hamiltonian of this model is similar to the one-dimensional spin-1 Heisenberg Hamiltonian,

$$\hat{H}_{\mathrm{AKLT}} = \sum_i \boldsymbol{S}_i \cdot \boldsymbol{S}_{i+1} + \frac{1}{3} (\boldsymbol{S}_i \cdot \boldsymbol{S}_{i+1})^2. \tag{3.26}$$

The name givers of this model (Affleck, Kennedy, Lieb, Tasaki) found the exact ground state by expressing the spin-1 operator $\boldsymbol{S}$ with two spins-1/2 in a triplet state and assuming

the singlet state between spin-1/2 on bonds. The state is thus not a product state, however it can be represented as a translationally invariant MPS with bond dimension $m = 2$,

$$A^+ = \begin{pmatrix} 0 & \sqrt{2/3} \\ 0 & 0 \end{pmatrix}, \qquad A^0 = \begin{pmatrix} -1/\sqrt{3} & 0 \\ 0 & 1/\sqrt{3} \end{pmatrix}, \qquad A^- = \begin{pmatrix} 0 & 0 \\ -\sqrt{2/3} & 0 \end{pmatrix}. \tag{3.27}$$

While there are few *exact* ground states in MPS representation, ground states of a large class of one-dimensional systems can be represented efficiently as a tensor chain. There are rigorous results regarding the entanglement entropy in ground states of *gapped* and *local* Hamiltonians—one can find a summary by Eisert, Cramer, and Plenio [50]. In one spatial dimension, such states fulfill an *area law*, meaning that the entropy scales like the subsystem's *surface*—as opposed to its area, which would be the case for generic states. In particular, this means that it is *constant* for any "local" separation of a one-dimensional system into two parts, independent of the total length of the chain.

For a matrix product state the entanglement entropy equals the entropy of the Schmidt coefficients (singular values) and is bounded above by its bond dimensions m,

$$S(\rho) = -\sum_{\alpha_i} S_{\alpha_i}{}^{\alpha_i} \ln S_{\alpha_i}{}^{\alpha_i} \leq \ln m. \tag{3.28}$$

Therefore, if the entanglement entropy is constant with system size, so is the required bond dimension—as opposed to the exponentially increasing bond dimension which would be required for a generic quantum state. Conversely, matrix product states with constant bond dimensions fulfill an entanglement area law *by construction*.

Eisert, Cramer, and Plenio [50] note that the area law in one dimension does not hold for critical systems, but one finds a logarithmic correction. For higher dimensions there are fewer rigorous results but the authors conjecture that area laws hold for an equally large class of models. Tensor networks can therefore efficiently represent states of low entanglement in higher dimensions. However, the topology of the tensor network needs to match the topology of the physical system—we need to have the same sense of "locality" in both cases.

Our approach in this thesis is conceptually less advantageous: we map a 2D system onto a one-dimensional MPS chain as shown in fig. 3.10 and discussed in section 3.3.2. Therefore, a bisection parallel to the rings of the 2D cylinder will "cut" width w many physically connected sites but only a single MPS bond. This bond therefore has to encode entropy proportional to the ring width,

$$S \propto w \leq \ln m. \tag{3.29}$$

Thus, exponentially large bond dimensions in system *width* are required, even for states which fulfill an area law. While the exponential cost places strict limits on the achievable system sizes, DMRG is still a competitive method as we saw in section 2.1 and we hope to push the limits a little further.

3.1.3 Symmetries

Matrix product states reduce the full many-body Hilbert space to the states with only area law entanglement. However, we can reduce the space further by enforcing symmetries of the Hamiltonian explicitly. The most important ones for DMRG simulation of the

Fermi-Hubbard model are particle number $\hat{n}$ and spin $\hat{S}^z$ symmetries, which are both $U(1)$. One can show these symmetries by calculating the commutators of conserved observables,

$$\hat{n} = \sum_{\boldsymbol{r},\sigma} \hat{c}^\dagger_{\boldsymbol{r},\sigma} \hat{c}_{\boldsymbol{r},\sigma} \tag{3.30}$$

$$\hat{S}^z = \frac{1}{2} \sum_{\boldsymbol{r}} \left(\hat{c}^\dagger_{\boldsymbol{r},\uparrow} \hat{c}_{\boldsymbol{r},\uparrow} - \hat{c}^\dagger_{\boldsymbol{r},\downarrow} \hat{c}_{\boldsymbol{r},\downarrow} \right), \tag{3.31}$$

with the Hamiltonian, $\hat{H}_{\text{Hub}}$ from eq. (1.2). Commutation is obvious for the on-site interaction terms $\prod_\sigma \hat{c}^\dagger_{\boldsymbol{r},\sigma} \hat{c}_{\boldsymbol{r},\sigma}$ as we always find pairs of fermionic operators. These pairs of fermionic operators also commute with the kinetic term of $\hat{H}_{\text{Hub}}$ because spins can only hop but not flip or explicitly,

$$\sum_{\boldsymbol{r}''} \left[\hat{c}^\dagger_{\boldsymbol{r},\sigma} \hat{c}_{\boldsymbol{r}',\sigma}, \hat{c}^\dagger_{\boldsymbol{r}'',\sigma} \hat{c}_{\boldsymbol{r}'',\sigma} \right] = \sum_{\boldsymbol{r}''} \delta_{\boldsymbol{r}'',\boldsymbol{r}'} - \delta_{\boldsymbol{r}'',\boldsymbol{r}} = 0. \tag{3.32}$$

A more in-depth introduction to the implementation of $U(1)$ symmetries in tensor networks can be found by Singh, Pfeifer, and Vidal [51], in this thesis we only want to motivate our notation. We want to consider eigenstates of $\hat{n}$. A unitary representation of the symmetry group is given by,

$$\hat{W}_\phi = \mathrm{e}^{-i\hat{n}\phi} = \bigotimes_{\boldsymbol{r}} \mathrm{e}^{-\mathrm{i}\,\hat{n}_{\boldsymbol{r}}\phi} = \bigotimes_{\boldsymbol{r}} \hat{W}^{(\boldsymbol{r})}_\phi, \quad \phi \in [0, 2\pi). \tag{3.33}$$

We can thus decompose our entire Hilbert space of L sites into a direct sum of vector spaces with fixed particle number n_i at each site,

$$\mathcal{H}\big|_n = \bigoplus_{\substack{n_1,\ldots,n_L \\ \sum_i^L n_i = n}} \mathcal{H}^1\big|_{n_1} \otimes \cdots \otimes \mathcal{H}^L\big|_{n_L}. \tag{3.34}$$

In our MPS language this means that we will now call tensor legs with upper (lower) indices to be *outgoing* (incoming) and we can label them by the symmetry label, i.e. the number of particles, they are carrying. We can graphically represent this using arrows as shown in fig. 3.7. We must only plug together incoming and outgoing arrows and we obviously need to put labels on the MPO tensors as well. Note that matrix product operators therefore also transform according to a specific symmetry sector, i.e. carry a particle number. This is required for consistency: if we consider a particle annihilator and a state of particle number n, we need to find a state of $n-1$ upon contraction.

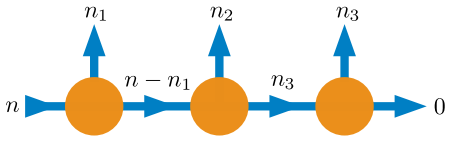

Figure 3.7: Three MPS tensors with particle number labels on their legs.

This means that we do not need to consider *dense* tensors A^{σ_i} at each site but instead we find a tensor block structure,

$$A = \bigoplus_b A_b, \tag{3.35}$$

where each block A_b is uniquely identified through its symmetry labels. In case of a single $U(1)$ symmetry we would only require one label per leg such that we can define the combined

label for a $\hat{n}$ symmetric rank three tensor as $b \coloneqq (n_{\text{in}}, n_\sigma, n_{\text{out}})$. The block structure then stems from the fact that we can only have blocks which conserve particle number, i.e. where all incoming and outgoing particle numbers add up to zero. This greatly decreases computational cost: naively, the complexity[5] of the contraction of two MPS tensors,

$$\sum_{\alpha_i} A_{\alpha_{i-1}}{}^{\sigma_i,\alpha_i} A_{\alpha_i}{}^{\sigma_{i+1},\alpha_{i+1}} \quad \to \quad \bigoplus_{b,b'} \delta_{b_{\text{out}},b_{\text{in}}} \sum_{\alpha_i} (A_b)_{\alpha_{i-1}}{}^{\sigma_i,\alpha_i} (A_{b'})_{\alpha_i}{}^{\sigma_{i+1},\alpha_{i+1}}, \tag{3.36}$$

would be $\mathcal{O}(m^3 d^2)$ for m dimensional bond indices α and d dimensional physical indices σ. But if we can split the bond dimension m into q evenly large[6] tensor blocks b, b', we only need to contract blocks with matching symmetry labels on connected legs, i.e. $\delta_{b_{\text{out}},b_{\text{in}}}$.

Each site can be occupied by at most two particles such that we need to contract each of the q tensor blocks with only three other blocks—corresponding to zero, one or two fermions at this site. The cost therefore reduces to $\mathcal{O}(3q(m/q)^3 d^2)$ where we did not consider that the physical dimension d also decreases: for the cases of zero or two particles at a give site, there is only one corresponding, local physical state. If we also included $\hat{S}^z$ symmetry—which can be done in precisely the same way by introducing a second symmetry label—the physical dimension would also be equal to one for either state with a single fermion. The effort would thus reduce to $\mathcal{O}(4q'(m/q')^3)$, where $q' > q$ is the number of blocks which increases when additional symmetries are considered. We find the same advantages if we consider e.g. cost for SVD: as the matrix is block diagonal, we can perform SVD on individual blocks to find cubic scaling only in block size, but linear costs for the number of blocks.

Although combining particle number $\hat{n}$ conservation and spin $\hat{S}^z$ symmetry to $U(1) \times U(1)$ suffices to reduce the physical dimension of each tensor block to one, we can do better. The Hubbard Hamiltonian conserves all components of the spin operator $\hat{\boldsymbol{S}}$ and we exploit the full $SU(2)$ spin symmetry. To observe spin conservation we introduce spinors,

$$\hat{\boldsymbol{c}}_{\boldsymbol{r}} \coloneqq \begin{pmatrix} \hat{c}_{\boldsymbol{r},\uparrow} \\ \hat{c}_{\boldsymbol{r},\downarrow} \end{pmatrix} \quad \Rightarrow \quad \hat{n}_{\boldsymbol{r}} = \hat{\boldsymbol{c}}^\dagger \cdot \hat{\boldsymbol{c}}, \tag{3.37}$$

and rewrite the Hubbard Hamiltonian such that there is no more explicit spin dependency,

$$\hat{H}_{\text{Hub}} = \sum_{\langle \boldsymbol{r},\boldsymbol{r'} \rangle} \left(\hat{\boldsymbol{c}}^\dagger_{\boldsymbol{r}} \cdot \hat{\boldsymbol{c}}_{\boldsymbol{r'}} + \text{H.c.} \right) + \frac{U}{2} \sum_{\boldsymbol{r'}} (\hat{n}_{\boldsymbol{r}} - 1) \hat{n}_{\boldsymbol{r}}. \tag{3.38}$$

Analogous to eq. (3.33), a two-dimensional unitary representation of the $SU(2)$ group is given by operators

$$\hat{W}_{\boldsymbol{a}} = \mathrm{e}^{-\mathrm{i}\, \boldsymbol{a} \cdot \hat{\boldsymbol{S}}}, \quad \hat{S}^j = \frac{1}{2} \sigma^j \quad \text{where} \quad \boldsymbol{a} \in \mathbb{R}^3, \tag{3.39}$$

where σ_j are Pauli matrices. But in eq. (3.38) we only have two-dimensional scalar products of spinors which are invariant under these unitary transformations.

The implementation of such non-abelian symmetries goes somewhat along the lines of the $U(1)$ symmetric tensor network but the details are much more involved. As this was not part of the thesis, we only want to sketch the procedure. The avid reader may find a very explicit description by Weichselbaum [52] and a possibly more mathematical approach by Singh and Vidal [53].

[5] There are improved algorithms for matrix multiplication but we consider the simple approach to be more instructive.

[6] This is generally not the case but it is a reasonable assumption to estimate the cost.

As for $U(1)$ symmetries, we need to label all legs of all tensor blocks with their respective symmetry sectors. For spin $SU(2)$ two labels $|S, S^z\rangle$ suffice but other symmetries will require additional z-labels[7] or further indices to lift degeneracy. In principle, additional labels do not make our situation more difficult: we can still match legs with corresponding symmetry sectors, we only have to pay attention on how to add up labels when we *split* or *fuse* tensor legs.

But as long as we only consider $SU(2)$ symmetric operators, we need not do everything explicitly. As states of the same S multiplet but with different S^z values are fully degenerate with respect to any $SU(2)$ symmetric operator, we do not have to care about the "internal" multiplet structure of an irreducible representation. The *Wigner-Eckart theorem* states how tensor blocks A which transform according to $|s, s_z\rangle$ on the physical leg factorizes,

$$\langle S_{\text{in}}, S^z_{\text{in}}| A^{(S_\sigma, S^z_\sigma)} |S_{\text{out}}, S^z_{\text{out}}\rangle = \underbrace{\langle S_{\text{in}} \| A^{S_\sigma} \| S_{\text{out}}\rangle}_{=A_b} \underbrace{\langle S_{\text{in}}, S_{\text{in}^z}| \left(|S_\sigma, S^z_\sigma\rangle \otimes |S_{\text{out}}, S^z_{\text{out}}\rangle\right)}_{=C_{b,b_z}}. \quad (3.40)$$

We find a *reduced* tensor block A_b which only depends on the total spin on each leg and *Clebsch–Gordan coefficients* C_{b,b_z} (CGC). The entire tensor is therefore diagonal in blocks $b = (S_{\text{in}}, S_\sigma, S_{\text{out}})$ defined through the S quantum numbers of each leg—but the internal structure, made up of b_z "sub-blocks", is given by Clebsch-Gordan tensors and thus *sparse*.

The advantage of enforcing full spin $SU(2)$ symmetry instead of just S^z is different from simply adding another (abelian) symmetry. We do not find more, and thus smaller, tensor blocks—but instead we require fewer parameters and thus smaller bond dimensions to describe the *same* matrix product state. This can be understood in such way: starting from a reduced tensor, we can restore the explicit S^z dependence by multiplying it with the corresponding, S^z dependent CGC tensor,

$$A = \bigoplus_b A_b \otimes C_b = \bigoplus_{b,b_z} A'_{b,b_z}. \quad (3.41)$$

The resulting tensor blocks A'_{b,b_z} are now larger by a factor of the dimensions of the Clebsch-Gordan tensor. But we still have $b = (S_{\text{in}}, S_\sigma, S_{\text{out}})$ labels for our blocks which we do not know if we only considered S^z symmetry—we therefore need to trace them out. Thus, we arrive at tensor blocks which are dense but still larger than the reduced tensors by a factor of CGC dimensions. In practice, we observe $U(1)$ symmetric bond dimensions to be roughly three times as large as the reduced $SU(2)$ dimensions. This is significantly less than Weichselbaum [52] found in his examples. We interpret it in such way, that multiplets with small S are most relevant for ground states of the Fermi-Hubbard model, as higher spins yield larger CGC tensors.

So far we have only considered tensors of rank three—while even matrix product operators are of rank four and other tensor network approaches require even higher ranks. But as one can build a tensor of rank n by combining $n-2$ tensors of rank three we do not have to work out any additional details but we can leave all further computations to our algorithm. One can obviously consider several abelian or non-abelian symmetries at once—simply by repeatedly breaking apart tensor blocks. For multiple $SU(N)$ symmetries this also implies building the tensor product over several Clebsch-Gordan tensors for the respective symmetries. In practice, this yields an awfully large number of indices and labels and slightly more difficulties for computing the CGC tensors for $N > 2$. We will therefore not dwell on any details but hope to have put the basic ideas of symmetric tensor networks across.

[7] z as in S^z for our case case

3.2 The DMRG algorithm

The *density matrix renormalization group* (DMRG) method for ground state search was invented by White [54] back in 1992. For the rest of this thesis we will however only be using the acronym DMRG. Not only as it is significantly shorter but also because the full name stems from its original derivation. However, DMRG can be explained much simpler in terms of matrix product states such that we do not want to dwell on the past.

The idea of DMRG is to *variationally* optimize a matrix product state by minimizing its energy, "one" MPS tensor at a time. This procedure is performed for one site after another till the end of the chain and back again—which is called one *sweep*. The bond dimension is usually limited to make computations feasible and each optimization thus requires truncation as in eq. (3.25).

In order to calculate the energy of a matrix product state we require an appropriate form of the Hamiltonian. The corresponding *matrix product operator* (MPO) is a chain of rank four tensors—all quantum mechanical operators we want to employ must be represented as an MPO. We employ a generic scheme for creating MPOs from single site operators, which is described by Hubig, McCulloch, and Schollwöck [55]. In particular, the generation of an MPO for the two dimensional Fermi-Hubbard model in hybrid space, which we will outline in the next section, is explained in this paper.

For textbook examples like the 1D Heisenberg or Ising models MPOs can be expressed by small matrices of operators—which are identical for all but first and last sites. But matrix product operators for two-dimensional systems or for inhomogeneous Hamiltonians from quantum chemistry are much more complex. MPOs can also become very large with bond dimensions $w = \mathcal{O}(100 \dots 1000)$ such that truncation becomes necessary, once more. Standard SVD compression is obviously possible—but it introduces a truncation error and it destroys sparsity of the tensors. Hubig, McCulloch, and Schollwöck [55] instead employ *delinearization* which achieves optimal compression for most MPOs, just like SVD, but retains sparsity and avoids spurious terms making MPO application faster and more stable numerically.

There are different approaches to finding the ground state[8] with different advantages and difficulties. *Two site DMRG* is closer to the "original" algorithm and is in some sense more physical. Convergence is "easier" to achieve and the *truncated* singular values can be interpreted in a physically meaningful way. However, the algorithm used for all results discussed in chapter 4 is an optimized version, *strictly single site DMRG*. It is more efficient for very large bond dimensions but requires extra care to avoid getting stuck in local minima. We will start by explaining the two site algorithm and will elaborate on the improved, single site method, later.

We now assume to have a random matrix product state and matrix product operator (MPO) representing the Hamiltonian. We now want to find the ground state by locally updating two MPS tensors. Although we only want to optimize two adjacent MPS tensors at a time, the energy is not a local observable. Therefore, we have to contract the entire MPO with all MPS sites to calculate $\langle\psi| \hat{H} |\psi\rangle$. Finding a two site tensor ${M_{\alpha_{i-1}}}^{\sigma_i,\sigma_{i+1},\alpha_{i+1}}$ which minimizes $\langle\hat{H}\rangle$ is equivalent to finding the lowest eigenvalue λ and "eigenvector" M of the contraction of $\langle\hat{H}\rangle$ *without* the tensor M. The eigenvalue problem is shown graphically in fig. 3.8. Such eigenvalue problems can be solved efficiently by using a *Lanczos* method for some matrix: one can find a reduced basis for the eigenproblem by repeatedly applying

[8] DMRG usually means the variational approach to ground state search. Imaginary time evolution would also be possible, but is rarely used.

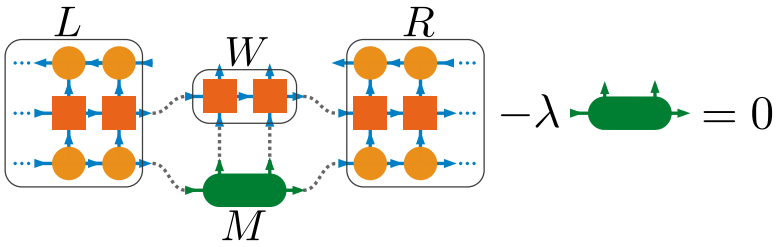

Figure 3.8: Eigenvalue equation for the two-site DMRG algorithm. In each optimization step we try to find the eigenstate M with the lowest eigenvalue (energy) λ. Tensors L, R of rank three can be cached and need not be calculated from scratch for each local optimization.

the matrix onto a single initial vector and reorthonormalizing the resulting vectors. Each application projects onto the subspace of extremal[9] eigenvalues and thus the ground state can be represented efficiently in a very small basis.

The most expensive step in a Lanczos algorithm generally is the application of the matrix to the vector—in our case it corresponds to a contraction of all but two tensors of $\langle \hat{H} \rangle$ as shown in fig. 3.8. The sequence of contractions has to be chosen carefully to reduce cost. Naively, one might contract the entire network except for M such that only a "single" contraction is required for each Lanczos step. But the cost of this contraction is of order $\mathcal{O}(m^4 d^4)$ and thus unfortunate for the typical order $m \gg w \gg d$ of MPS bond dimension m, MPO bond dimension w and physical dimension d. Also, the "matrix" LWR would be of size $\mathcal{O}(m^4 d^4)$ such that memory would restrict the achievable bond dimensions m.

The left (right) contraction L (R) only need to be computed—one at a time—during the right (left) sweep and can be stored for the return. As we primarily care about the cost for each Laczos step we can neglect the contraction of L and R. Generally, the best contraction sequence is then given by first contracting LM, then $(LM)W$ and finally multiplying R to it. The cost of these steps is $\mathcal{O}(2m^3wd^2 + m^2w^2d^4)$ and we do not have to store objects larger than $\mathcal{O}(m^2wd^2)$.

Naively, the Fermi-Hubbard model should have physical dimension $d = 4$ and one would expect $d \geq 2$ for all physically interesting models. However, as we saw in section 3.1.3, the use of symmetries can lead to $d = 1$ tensor blocks and in this case we can do better. For $d = 1$ it is advantageous to first compute the contraction LW which has to be done only once per Lanczos procedure. The following contraction $(LW)M$ and multiplication of R is of order $\mathcal{O}(d^4m^3w + m^3d^2w) = \mathcal{O}(2m^3w)$. We have therefore only improved the subleading terms—in any way, we recommend using a method as described by Pfeifer, Haegeman, and Verstraete [56] to check the efficiency of a contraction sequence.

A conceptual advantage of optimizing two sites is that we require *exactly* one singular value decomposition ${M_{\alpha_{i-1}}}^{\sigma_i,\sigma_{i+1},\alpha_{i+1}} \to {U_{\alpha_{i-1}}}^{\sigma_i,\alpha_i} {S_{\alpha_i}}^{\alpha_i} {(V^\dagger)_{\alpha_i}}^{\sigma_{i+1},\alpha_{i+1}}$ and thus exactly one truncation to find the new normalized MPS tensors. The truncated singular values are therefore the difference between the optimized tensor and the resulting MPS and can be interpreted as *truncation error*. If this error is summed up for the entire sweep, one finds a proxy for the accuracy of the matrix product state—without additional cost.

However, there is no pressing reason to optimize *two* local tensors at a time—at least in the modern approach of matrix product states. After all, the advantage of DMRG over a simple Lanczos method is due to the fact that we can break our system down into small

[9] It projects onto the space of the *largest* eigenvalues but you can always shift and invert your operator.

parts and thus reduce the dimensions of our problem. So the computations would be least expensive if we sweeped through the chain ***one* site at a time**.

But, especially if we introduced symmetries, one needs to be careful in doing so. For some reasons our state—initial or a later stage—might be such that at one *bond* some symmetry sectors, while theoretically possible, are not used, i.e. the corresponding tensor blocks are zero. Optimization of a single site is unable to populate these sectors, even if they could contribute to a lowered energy, because the corresponding blocks in the neighboring tensors are not present. Therefore, a single site approach will require an additional step to avoid getting stuck in local minima.

Our approach is the *strictly single site* DMRG algorithm (**DMRG3S**) published by Hubig et al. [57]. We add tensor blocks to an optimized single site tensor in a process called subspace expansion. Assuming a left to right sweep, we extend a single tensor by P^{σ},

$$M^{\sigma_i} \quad \rightarrow \quad \tilde{M}^{\sigma_i} = \begin{pmatrix} M^{\sigma_i} & P^{\sigma_i} \end{pmatrix}, \tag{3.42}$$

and we need to pad the next tensor to the right with zeros to make the contraction work out,

$$B^{\sigma_{i+1}} \quad \rightarrow \quad \tilde{B^{\sigma_{i+1}}} = \begin{pmatrix} B^{\sigma_{i+1}} \\ 0 \end{pmatrix}. \tag{3.43}$$

So how do we get an appropriate rank three tensor P? We would like to use local tensors Z^{σ_i} of the residual $|Z\rangle$ as they represent the difference to a true eigenstate of $\hat{H}$,

$$|Z\rangle \coloneqq \hat{H}\,|\psi\rangle - E\,|\psi\rangle = \sum_{\boldsymbol{\sigma}} Z^{\sigma_1} \cdots Z^{\sigma_l}\,|\boldsymbol{\sigma}\rangle\,. \tag{3.44}$$

But calculating Z^{σ_i} is too expensive so we need a different rank three tensor with suitable properties. A cheaply available option is the contraction

$$P = \alpha L M W, \tag{3.45}$$

as depicted in fig. 3.9 with some mixing factor α. The resulting tensor P^{σ_i} is of dimensions $(d_i, m_{i-1}, w_i \cdot m_i)$. If the bond dimension is sufficient and we have found the true ground state, applying the Hamiltonian in its MPO form will not change the state—expanding the tensor M^{σ_i} by P^{σ_i} as given in eq. (3.45) would only contribute linearly dependent components. However, if the ground state is not in the space of matrix product states we can consider, subspace expansion will increase the energy. We therefore introduce a parameter α which controls the amount of mixing such that we can find the lowest energy MPS of a given bond dimension, even if it is not the ground state.

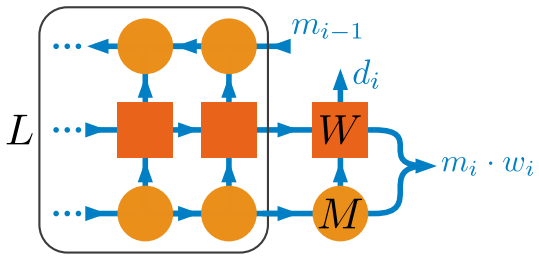

Figure 3.9: The rank three tensor used for subspace expansion in DMRG3S. The contraction is equivalent to projecting $|\psi\rangle$ onto $\hat{H}\,|\psi\rangle$ for all sites left of i. If $|\psi\rangle$ is an eigenstate of $\hat{H}$ we find a multiple of M, otherwise we will find orthogonal components and we will expand the subspace on bond $i+1$.

Hubig et al. [57] compare DMRG3S with another single site DMRG algorithm and with two site DMRG for a spin chain. All algorithms converged to similar results, although the

single site methods achieved lower energies. However, the cost for two site DMRG scales much worse than the single site methods as the bond dimension increases. While we can achieve larger bond dimensions and thus smaller errors, it is more difficult to measure the latter: for the two site algorithm the truncated weights were precisely the distance between optimized and final matrix product state as we saw in eq. (3.25). While truncation is also necessary for single site DMRG, the interpretation is less obvious. The singular values are determined not just through the eigensolver but also by the subspace expansion. While the latter should not introduce any additional errors *if* we found the ground state, the behavior for approximations to the ground state is not clear. And if we turned off subspace expansion, we would see truncated singular values only for the sectors which are allowed by the adjacent tensors.

3.3 DMRG in two dimensions

In this section we want to discuss how we used the DMRG algorithm to find ground states of two dimensional systems. Generally, there are two different approaches: one can either extend the notion of matrix product states to higher dimensional tensor network states (TNS) or one can introduce a mapping to describe a higher dimensional, finite system by a one-dimensional MPS.

The first approach, using two-dimensional tensor network states to describe a 2D system is conceptually striking: by construction we can describe a system which obeys the entanglement area law with constant bond dimension, i.e. we require only a minimal number of parameters to describe 2D ground states. The simplest kind of two-dimensional TNS is called *projected entangled pair states* (PEPS), a description of this method can be found e.g. by Orús [40]. However, PEPS is computationally more complex than DMRG: as the tensor network is two-dimensional one cannot left- or right-normalize tensors and the contraction of a network becomes costly. There are approximations to reduce the effort, see e.g. Phien et al. [58] for the case of infinite projected entangled pair states (iPEPS). However, there is still a sharp limit in the bond dimensions which can be achieved.

We will instead employ the second approach and describe a two-dimensional lattice in terms by a 1D matrix product state. In the following subsection we will write down the Hubbard Hamiltonian from eq. (1.2) in mixed real and momentum space. Then we will consider 2D $\rightarrow$ 1D mapping we use to construct our effective one-dimensional system.

3.3.1 Hybrid space

Unlike most numeric methods, DMRG "prefers" open boundary conditions as there is less long range entanglement, i.e. across the boundaries. While it is possible to make a periodic matrix product state by closing the tensor chain, one can no longer normalize the tensors appropriately and computations would scale worse with bond dimension m. On the other hand we have argued in section 3.1.2 that the required bond dimension scales exponential in system *width*—we can therefore only achieve widths $w \leq 6 \dots 8$. It can hardly be argued that such a narrow system describes the thermodynamic limit such that it would be advantageous to employ periodic boundary conditions along the width, forming a cylindric geometry.

Periodic boundaries also yield (quasi)momentum conservation, a symmetry we obviously want to exploit. We can do so by transforming our Hamiltonian into momentum space—each tensor leg gets an additional label and the total momentum has to be conserved *modulo* 2π. However, taking the Fourier transformation of the entire Hamiltonian is not ideal: $\hat{H}_{\mathrm{Hub}}$ as

given in eq. (3.38) is local in real space such that we can expect a rather small MPO and short range correlations of the ground state. These properties are advantageous for tensor network simulations, and we will lose them as we go to momentum space. Ehlers et al. [59] performed DMRG simulations of the Hubbard model in k-space but were restricted to system sizes of 6×6 for these reasons.

To get the best of both worlds, we transform the Hubbard Hamiltonian to *hybrid* space: we stay in real space along the legs of the cylinder to keep interaction *local* for the long axis, but we perform the Fourier transformation along each *ring* such that we can exploit momentum conservation for the periodic axis. This method is rather new, it has first been published by Motruk et al. [60] for other Hamiltonians and more recently Ehlers, White, and Noack [48] applied this approach to the Fermi Hubbard model.

We transform the spinor operators from eq. (3.38) to hybrid space,

$$\hat{\boldsymbol{c}}_{x,y} = \frac{1}{\sqrt{w}} \sum_{k=1}^{w} \mathrm{e}^{2\pi\,\mathrm{i}\,yk/w}\, \hat{\boldsymbol{c}}_{x,k} \qquad \text{and} \qquad \hat{\boldsymbol{c}}^\dagger_{x,y} = \frac{1}{\sqrt{w}} \sum_{k=1}^{w} \mathrm{e}^{-2\pi\,\mathrm{i}\,yk/w}\, \hat{\boldsymbol{c}}^\dagger_{x,k}, \tag{3.46}$$

where x, y denote real space coordinates, $2\pi k/w,\ k \in \mathbb{N}$ is the quasimomentum along each ring. The Hubbard Hamiltonian now consists of three parts, the on-site interaction term $\hat{H}_{\text{int}} \propto U$ and kinetic terms corresponding to hopping along a leg $\hat{H}_{\text{inter-ring}}$ or a ring $\hat{H}_{\text{intra-ring}}$. The inter-ring hopping term stays basically invariant—intuitively, a particle moving along a leg does not change its intra-ring momentum,

$$\begin{aligned}
\hat{H}_{\text{inter-ring}} &= \sum_{x=1}^{l-1} \sum_{y=1}^{w} \hat{\boldsymbol{c}}^\dagger_{x,y} \cdot \hat{\boldsymbol{c}}_{x+1,y} + \text{H.c.} \\
&= \frac{1}{w} \sum_{x=1}^{l-1} \sum_{y=1}^{w} \sum_{k,k'=1}^{w} \mathrm{e}^{2\pi\,\mathrm{i}\,y(k'-k)/w}\, \hat{\boldsymbol{c}}^\dagger_{x+1,k} \cdot \hat{\boldsymbol{c}}_{x,k'} + \text{H.c.} \\
&= \sum_{x=1}^{l-1} \sum_{k=1}^{w} \hat{\boldsymbol{c}}^\dagger_{x,k} \cdot \hat{\boldsymbol{c}}_{x+1,k} + \text{H.c.}
\end{aligned} \tag{3.47}$$

The intra-ring hopping term does change its shape. The Fourier transform of a tight-binding term makes it diagonal,

$$\begin{aligned}
\hat{H}_{\text{intra-ring}} &= \sum_{x=1}^{l} \sum_{y=1}^{w} \hat{\boldsymbol{c}}^\dagger_{x,y} \cdot \hat{\boldsymbol{c}}_{x,y+1} + \text{H.c.} \\
&= \frac{1}{w} \sum_{x=1}^{l} \sum_{y=1}^{w} \sum_{k,k'=1}^{w} \mathrm{e}^{-2\pi\,\mathrm{i}(y+1)k/w}\, \mathrm{e}^{2\pi\,\mathrm{i}\,yk'/w}\, \hat{\boldsymbol{c}}^\dagger_{x,k} \cdot \hat{\boldsymbol{c}}_{x,k'} + \text{H.c.} \\
&= \sum_{x=1}^{l} \sum_{k=1}^{w} \mathrm{e}^{-2\pi\,\mathrm{i}\,k/w}\, \hat{\boldsymbol{c}}^\dagger_{x,k} \cdot \hat{\boldsymbol{c}}_{x,k} + \text{H.c.} \\
&= 2 \sum_{x=1}^{l} \sum_{k=1}^{w} \cos(2\pi k/w) \left(\hat{\boldsymbol{c}}^\dagger_{x,k} \cdot \hat{\boldsymbol{c}}_{x,k} + \text{H.c.} \right).
\end{aligned} \tag{3.48}$$

So far the transformations have been straightforward and the results are simpler than they were in real space. But the on-site interaction term was already diagonal in real space such

that it will become more complex in hybrid space,

$$\begin{aligned}\hat{H}_{\text{int}} &= \frac{U}{2}\sum_{x=1}^{l}\sum_{y=1}^{w}\hat{n}_{x,y}\left(\hat{n}_{x,y}-1\right) = \frac{U}{2}\sum_{x=1}^{l}\sum_{y=1}^{w}\left((\hat{\boldsymbol{c}}^{\dagger}_{x,y}\cdot\hat{\boldsymbol{c}}_{x,y})(\hat{\boldsymbol{c}}^{\dagger}_{x,y}\cdot\hat{\boldsymbol{c}}_{x,y}) - \hat{\boldsymbol{c}}^{\dagger}_{x,y}\cdot\hat{\boldsymbol{c}}_{x,y}\right)\\ &= \frac{U}{2w}\sum_{x=1}^{l}\sum_{y=1}^{w}\sum_{k,k'=1}^{w}\mathrm{e}^{2\pi\,\mathrm{i}\,y(k'-k)/w}\\ &\qquad\times\left(\frac{1}{w}\sum_{q,q'=1}^{w}\mathrm{e}^{2\pi\,\mathrm{i}\,y(q'-q)/w}(\hat{\boldsymbol{c}}^{\dagger}_{x,k}\cdot\hat{\boldsymbol{c}}_{x,k'})(\hat{\boldsymbol{c}}^{\dagger}_{x,q}\cdot\hat{\boldsymbol{c}}_{x,q'}) - \hat{\boldsymbol{c}}^{\dagger}_{x,k}\cdot\hat{\boldsymbol{c}}_{x,k'}\right)\\ &= \frac{U}{2w}\sum_{x=1}^{l}\sum_{k=1}^{w}\sum_{k'=1}^{w}\sum_{q=1}^{w}\left((\hat{\boldsymbol{c}}^{\dagger}_{x,k}\cdot\hat{\boldsymbol{c}}_{x,k'})(\hat{\boldsymbol{c}}^{\dagger}_{x,q}\cdot\hat{\boldsymbol{c}}_{x,q+k-k'}) - \hat{\boldsymbol{c}}^{\dagger}_{x,k}\cdot\hat{\boldsymbol{c}}_{x,k'}\right).\end{aligned} \tag{3.49}$$

The total Hubbard Hamiltonian is then given by,

$$\hat{H}_{\text{Hub}} = \hat{H}_{\text{int}} + \hat{H}_{\text{intra-ring}} + \hat{H}_{\text{inter-ring}}, \tag{3.50}$$

and can be created as matrix product operator via methods described by Hubig, McCulloch, and Schollwöck [55]. The new operators $\hat{\boldsymbol{c}}^{(\dagger)}_{x,k}$ do not only carry symmetry labels for particle number and spin on their legs but also quasi momentum labels corresponding to k. We can thus also use these labels for MPS tensors and further break down the tensor block structure to reduce the computational costs. Following Ehlers, White, and Noack [48], we can estimate the cost assuming constant bond dimensions: in section 3.2 we found the cost for each Lanzcos step to be $\mathcal{O}(d^2m^3w)$, where w was the MPO bond dimension. We can resolve the conflicting usage of the letter w by assuming the MPO bond dimension to be proportional to system width. This assumption is reasonable because the interaction terms are delocalized over the cylinder's circumference and it coincides with observations by Hubig, McCulloch, and Schollwöck [55]. If we assume that we require K Lanczos steps on each site to achieve convergence, this yields costs $\mathcal{O}(Km^3w^2ld^2)$ without considering symmetries. If we employ momentum conservation, we will find *width* w many symmetry sectors which we assume to be of equal size. The tensor contractions for each Lanczos step therefore simplify to $\mathcal{O}(d^2w^2(m/w)^3)$ such that w cancels for the estimated total cost, $\mathcal{O}(Km^3ld^2)$.

This estimate is obviously highly misleading: in order to accurately represent a two-dimensional ground state, we require MPS bond dimensions $m \propto \exp(w)$. Using symmetries we can reduce costs and make accurate calculations on *slightly* larger systems possible—but we cannot beat the exponential scaling in system width. We furthermore note that the estimate by Ehlers, White, and Noack [48] was made for the comparison of *hybrid* space calculations with and without explicit momentum conservation. In purely real space the MPO dimensions might scale more favorable as there are only local terms. Unfortunately, this interaction term which makes our hybrid space approach hard is most important in the interesting regime of strong interactions $U \gtrsim 8$.

3.3.2 Site reordering

By construction of a matrix product state, correlations between adjacent tensors can be described most efficiently. This is why DMRG is particularly efficient for 1D Hamiltonians with local interaction, ideally only between neighboring sites. While the interaction in the Hubbard model on the 2D cylinder surface is only between nearest neighbors,[10] there is no

[10] In a real space basis—in hybrid space things get more "ugly", anyway.

way to map this system onto 1D without introducing longer range terms: we could put all sites on a ring next to each other, but then the respective nearest neighbors are separated by cylinder's circumference.

As we want to employ momentum conservation by going to hybrid space as described in section 3.3.1, the question of how to map 2D $\rightarrow$ 1D becomes more important. The Hamiltonian eq. (3.50) is non-local in momentum space and there are four-site interaction terms.

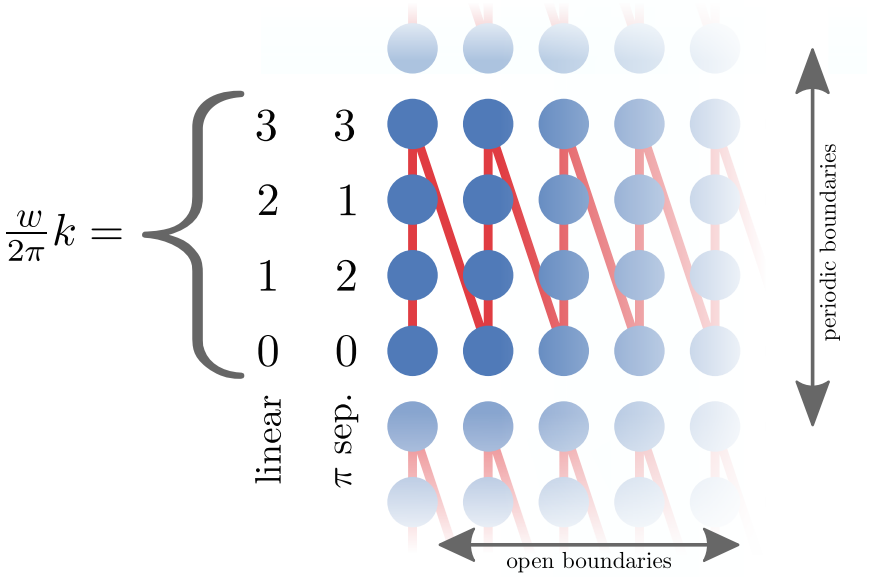

Figure 3.10: The "Z" mapping from a 2D lattice to a 1D MPS. Blue dots are 2D lattice sites and 1D MPS tensors, respectively. The red line indicates the 1D matrix product state chain. We consider a cylinder with *periodic rings* and *legs* with *open* boundaries. The momenta on each ring can be ordered linearly or such that neighboring sites differ by momentum π ("π sep."). Other ring orderings were considered but are not shown in this section.

The mapping we use for our computations is shown in fig. 3.10. We will call it "Z" mapping as the 1D tensor chain forms this letter when drawn in the two dimensional lattice. In this mapping all sites on one ring are placed next to each other in the matrix product state. Previous studies of the Hubbard model in momentum space by Ehlers et al. [59] showed that there are strong correlations between momentum space sites separated by $k = \pi$—especially so in the case of half-filling. Therefore, it might be most efficient to put these sites next to each other in the MPS. This ordering of the momenta on one ring is indicated in fig. 3.10 and will in the following be denoted by "π separation".

Other mappings we consider in this section are shown in fig. 3.11. The ordering of momenta on the rings can be chosen for each map—we will only use linear and π separated orderings. There is no obvious reason why these mappings should actually be "good".[11] It is possible that less simple, less "continuous" maps might be advantageous. In the following we will simply start from these maps to study their consequences for DMRG calculations, hoping to find a way to determine the optimal map.

[11] We still need to find a way to measure this.

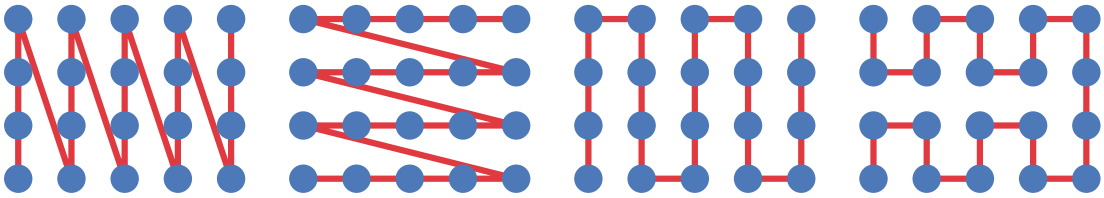

(a) "Z" map. (b) Flipped "Z" mapping. (c) "S" map. (d) Two-site meander map.

Figure 3.11: 2D → 1D mappings we compare in this section. As in fig. 3.10, the real space axis with open boundaries is to the right, the momentum space axis with periodic boundaries is in y direction. The meander map requires one system size to be odd, the other one to be even. We thus chose odd lengths for this comparison—the system width should be even, such that momenta separated by $\Delta k = \pi$ can be represented.

We start our comparison by studying small systems at half-filling which is the simplest case computationally. The energies we found on a $w = 4$, $l = 3$ cylinder for the different mappings at various bond dimensions are plotted in fig. 3.12. We ran one calculation for each map where we held the maximal $SU(2)$ bond dimension fixed for three consecutive stages. Energies after the last two stages are shown to indicate whether the maximal bond dimension had already been exhausted and whether there is convergence.

As the system is very small, most mappings find convergence with relative errors in energy less than 10^{-12} for bond dimensions $m \gtrsim 1500$. For "S" and "Z" mappings there is no significant difference for linear or π separated ordering of momenta—however there is a significant difference for the flipped "Z" and the meander mapping. For the latter cases, sites which are connected through the four-site interaction term in eq. (3.49) are separated by a number of sites proportional to the system length. Therefore the ordering of momenta on each ring makes a much greater difference and only the π separated orderings converge.

Judging from this first plot and for bond dimensions $m \lesssim 1000$ it appears that the flipped "Z" mapping might be the best one and that the meandering shape might also be competitive. As we consider a longer cylinder length $l = 7$, these impressions turn out to be wrong. The corresponding dataset is plotted in fig. 3.13. For a longer system the separation between the sites contributing to the interaction term increases which we assume to be disadvantageous. If we order the momenta with π separation we gain some accuracy—more so for the meandering map. This is quite possibly because the strongly correlated sites which are separated by momentum $\Delta k = \pi$ are once again nearest neighbors in the meandering MPS chain. "S" and "Z" mappings show little difference in convergence.

From these observations we conclude that "S" and "Z" mappings are clearly advantageous for systems where $l > w$, but also not significantly worse for short cylinders than any other map we tried. As we always consider an anisotropic geometry with open ends on the x-axis but a periodic y-axis, it might be reasonable to chose cylinders of longer width than height. Studies of the Heisenberg model with mixed open and periodic boundaries by White and Chernyshev [61] suggest an aspect ratio of $L_x/L_y \approx 1.76$ for fastest convergence to the thermodynamic limit. As the Heisenberg model is an effective description of the Hubbard model with strong interaction at half-filling, we suppose their results are applicable to our problem.

We consider the same system parameters, $l = 7$, $w = 4$, $U = 8$ also with doping, $n = 0.875$. In fig. 3.14 only results for "S" and "Z" maps are shown. However, we also want to have

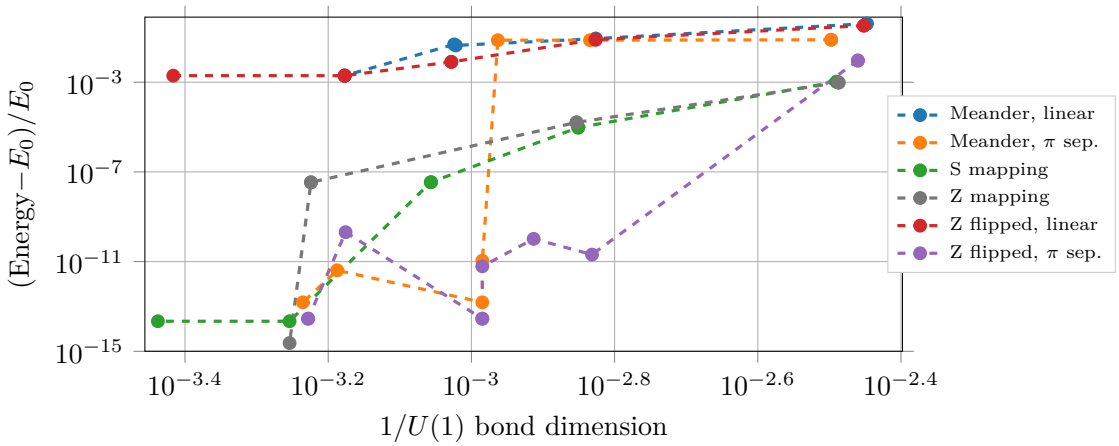

Figure 3.12: Energies for different 2D $\to$ 1D mappings on a $w = 4$, $l = 3$ cylinder. The energy for each ordering and bond dimension was compared to the true ground state energy E_0. E_0 was obtained using "Z" mapping and significantly larger bond dimensions. At each maximal bond dimension there were three stages with up to 60 sweeps in total. The energies of both last stages are shown such that convergence can be judged. The cubed average of the MPS bond dimensions is shown on the x-axis. The calculations were performed for $U = 8$ at half-filling.

an estimate for the error of the energy. One possible way[12] is to calculate the standard deviation of the energy,

$$\sigma = \sqrt{\langle\psi|\,\hat{H}^2\,|\psi\rangle - \langle\psi|\,\hat{H}\,|\psi\rangle^2}. \tag{3.51}$$

The variance is zero if and only if $|\psi\rangle$ is an eigenstate of the Hamiltonian. Assuming $|\psi\rangle$ is close enough to the ground state such that it can be written as

$$|\psi\rangle = a\,|E_0\rangle + \mathrm{e}^{\mathrm{i}\,\phi}\sqrt{1-|a|^2}\,|E_1\rangle\,, \tag{3.52}$$

then the standard deviation would be given as

$$\sigma = |a|\sqrt{1-|a|^2}(E_1 - E_0). \tag{3.53}$$

The energy difference between $|\psi\rangle$ and $|E_0\rangle$ would then be given as

$$\langle\psi|\,\hat{H}\,|\psi\rangle - E_0 = (1-|a|^2)(E_1 - E_0). \tag{3.54}$$

This is a very conservative estimate of the error if we are close to the ground state and $a \lesssim 1$.

We find a very similar behavior of the energies, the data points lay pretty much on top of each other. The estimated errors are also identical for the mappings with π separated momenta—they decrease faster than linear as the reciprocal bond dimension goes to zero. However we fail to compute the standard deviation of $\hat{H}$: we find negative values of the variance $\sigma^2(\hat{H})$ for different bond dimensions, system sizes and fillings. We do not know where these unphysical results come from. For now, we interpret this observation such that linear momentum ordering is more difficult to handle numerically.

[12] Unfortunately, it is only feasible for very small systems.

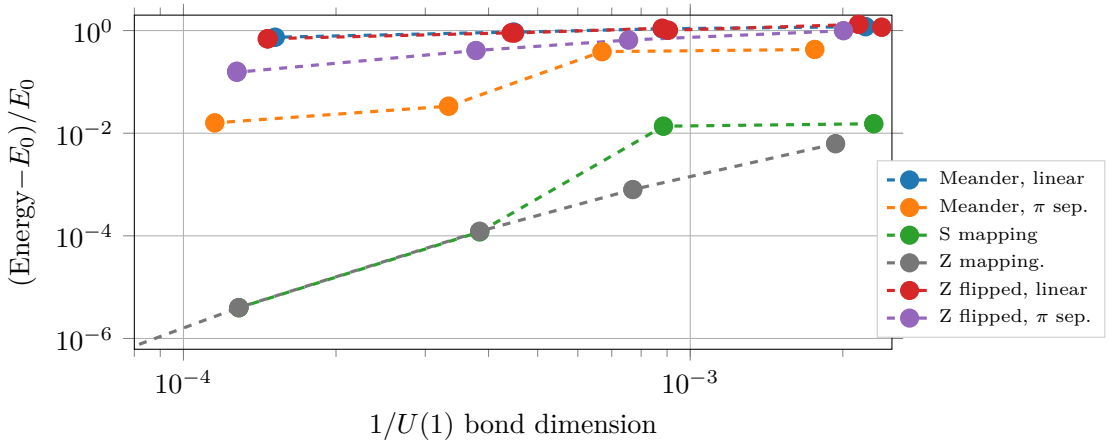

Figure 3.13: Energies for different mappings on a longer $w = 4$, $l = 7$ cylinder. The data was obtained as described for fig. 3.12. As the system is larger, the bond dimensions shown are not sufficient to describe the true ground state. Also E_0 might not be as precise but seems to suffice for this comparison.

However, if we take a closer look at the convergence of the energies for each mapping there are barely any differences. As we do not have a well converged state at large enough bond dimension, we only compare energies of different mappings at fixed bond dimension. The results are shown in fig. 3.15. The linear "S" mapping always produces energies which are larger than average, but the difference is rather small.

So far we have tried to answer the question, which map allows for the most accurate representation of the ground state at fixed bond dimension. However, changing the order of sites on the MPS chain primarily changes the shape of the matrix product *operators*. To find the *optimal* mapping we thus need to consider the **MPO bond dimensions**, as well. In fig. 3.16 the bond dimensions required to represent the total Hamiltonian after truncation via singular value decomposition are shown. We find that π separated momentum reordering *always* decreases the required bond dimension. Furthermore, one can see that "S" and "Z" maps require only a constant bond dimension with increasing cylinder length, whereas other orderings increase linearly.

The cost of applying an MPO to an MPS does not simply depend on the MPO's bond dimensions but rather on the number of tensor blocks and their respective size, as we saw in section 3.1.3. We observe in fig. 3.17 that the size of tensor blocks is actually constant for "S" and "Z" mappings, regardless of momentum ordering. Other orderings yield larger dimensions of the individual blocks which also increase with system width.

From these calculations we conclude that it is best to put sites of the same ring close to each other. Intuitively, this makes sense as we considered the case of strong on-site interaction—and the interaction is given by four-site terms on each ring. We find that momentum reordering can improve performance, especially for the case of half-filling. As we can only consider systems of small width, there are not many possible ring orderings.

There are many possible mappings we did not consider. We do not expect that more "obscure" maps should yield significantly improved energy convergence. But it is likely that systems with different physical parameters and shapes prefer different maps—we suspect that systems with weak interaction $U \lesssim 2$ could be represented more accurately using a "flipped" map. Even if we restrict ourselves to only a hand full of mappings and very small bond dimensions, it is not feasible to perform such analysis on larger systems. It would

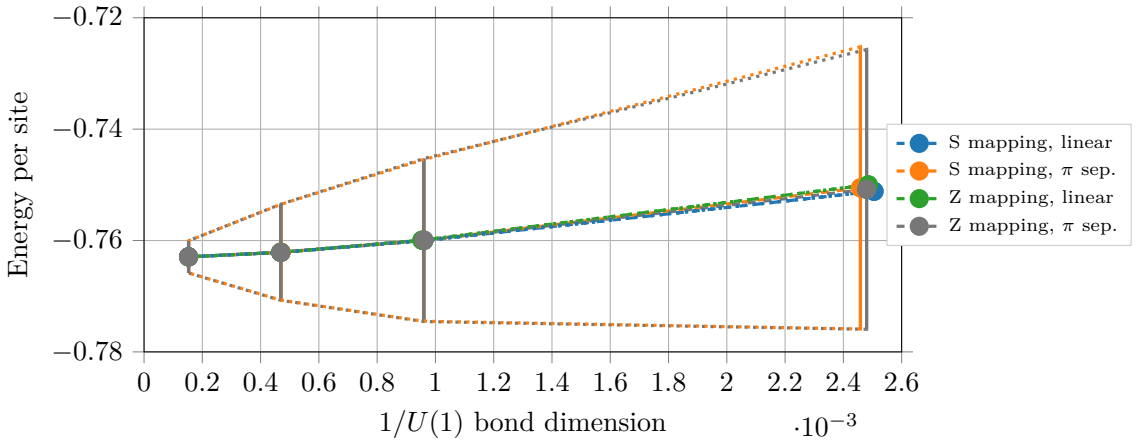

Figure 3.14: Energy for "S" and "Z" mappings for a doped system with strong interaction $U = 8$. The energies are very close for all maps, the standard deviation of $\hat{H}$ is also almost identical for mappings with π separated momenta. Estimated errors for linearly ordered momenta are not shown as their computation failed.

thus be desirable to have an *ab initio* method to predict the optimal map from physical sites to MPS tensors.

As we saw in section 3.1.2, matrix product states can very efficiently encode entanglement between *neighboring sites* in the MPS chain—longer range correlations can only be represented with larger bond dimensions. Therefore, we want to measure the entanglement between any two sites and reorder our sites such that there is strong entanglement only between sites close to each other—thus minimizing the total **entanglement distance**.

We measure the entanglement of a density matrix $\hat{\rho}$ as its von Neumann entropy,

$$S(\hat{\rho}) = -\operatorname{tr}(\hat{\rho} \ln \hat{\rho}), \tag{3.55}$$

and thus define the *mutual information* of systems A and B,

$$I_{A,B} \coloneqq S(\hat{\rho}_A) + S(\hat{\rho}_B) - S(\hat{\rho}_{AB}), \tag{3.56}$$

where $\hat{\rho}_{AB}$ is the density matrix of systems A and B combined. Mutual information has very direct implications on physical quantities: it is an upper bound for correlators of arbitrary observables $\hat{O}_A$, $\hat{O}_B$ [62],

$$I_{A,B} \geq \frac{\left(\langle \hat{O}_A \otimes \hat{O}_B \rangle - \langle \hat{O}_A \rangle \langle \hat{O}_B \rangle\right)^2}{2\|\hat{O}_A\|_1^2 \|\hat{O}_A\|_1^2}. \tag{3.57}$$

Calculating the single site entropy is rather cheap with matrix product states. If one chooses proper normalization, the one-site density matrix can be obtained by contracting a single MPS tensor with its Hermitian conjugate as shown on the left in fig. 3.18. Finding the two-site reduced density matrix requires more effort as the distance between both sites increases. As sketched on the right of fig. 3.18, one needs to contract all physical legs between the considered sites. It is crucial to choose proper normalization and to contract the outer legs on the left and right side, as the resulting tensor would otherwise be of size $\mathcal{O}(m^4)$. The cost of each contraction is $\mathcal{O}(m^3 d^3)$. And even though we can store contractions and build upon them, if we want to calculate *all* two-site entropies, the computational effort is only feasible for small systems and bond dimensions.

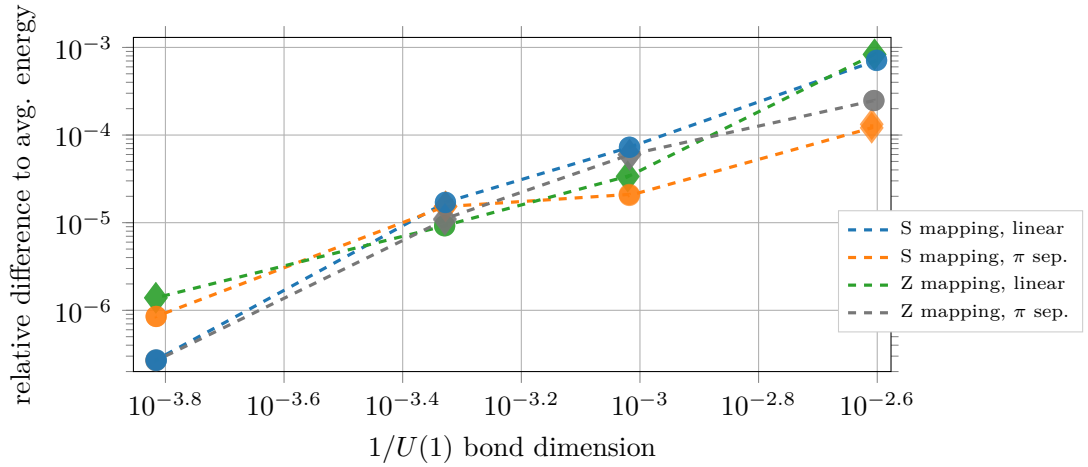

Figure 3.15: Comparison of energies for "S" and "Z" mappings for a doped system. For each bond dimension we plot the relative difference to the mean energy of all four mappings at this stage. Diamond symbols indicate that energy is lower than the mean value, circles denote larger than average energies. The dashed lines are thus only guides for the eye.

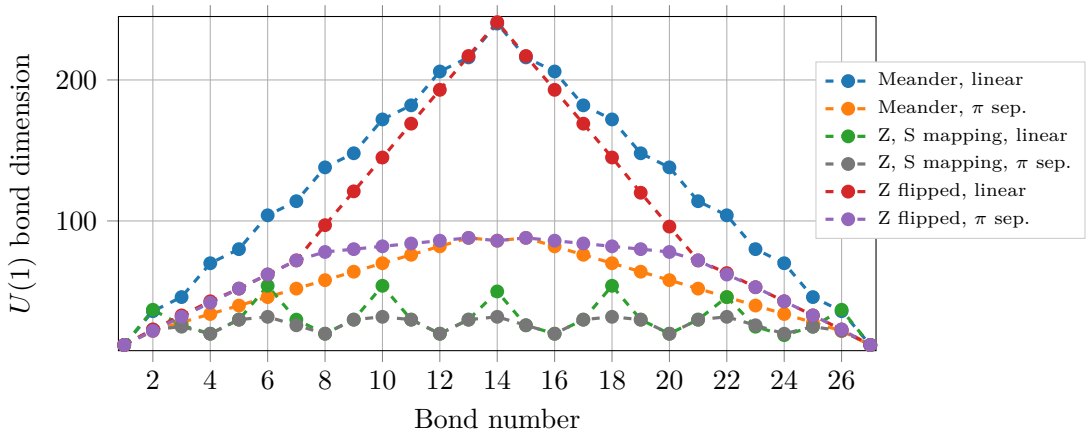

Figure 3.16: $U(1)$ bond dimensions of the Hamiltonian's MPO representation for different mappings. The bond dimensions increase roughly linear in cylinder length for "meander" and flipped "Z" maps. As one can see from the lines for "S" and "Z" maps, this corresponds to the intra-ring interaction terms—the bond dimension is thus constant in cylinder length for these maps. In all cases we find significantly smaller bond dimensions for π separated momentum ordering.

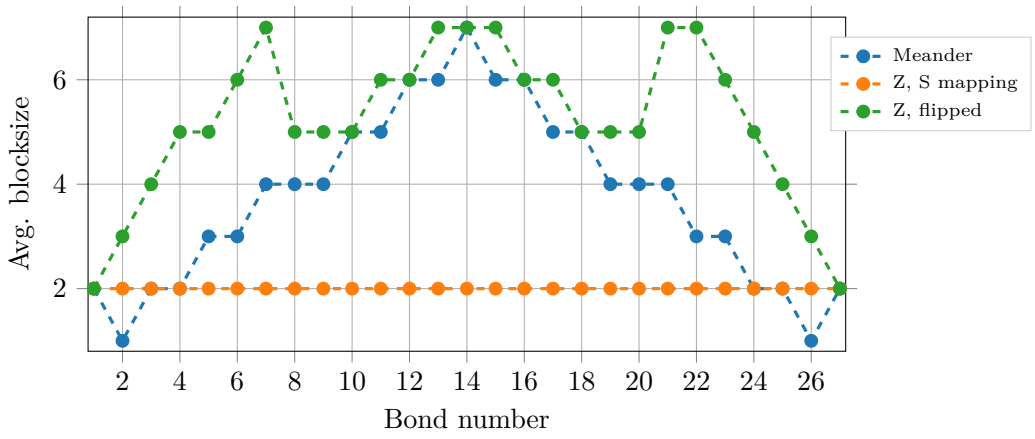

Figure 3.17: The cubed average size of tensor blocks in the MPO representation of $\hat{H}$. "S" and "Z" maps yield a constant and small tensor block size. Meandering and flipped "Z" mappings lead to larger tensor blocks making computations less efficient. There is little difference for linear and π separated orderings (not shown).

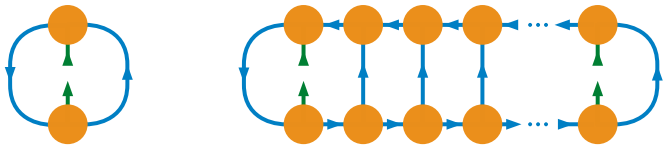

Figure 3.18: Calculation of reduced density matrices from an MPS state. If all sites to the left (right) of the considered site are left (right) normalized, the one-site density matrix can be obtained by contracting the corresponding MPS tensor with its Hermitian conjugate as shown on the left. For the two-site density matrix the physical legs between both sites need to be contracted as shown on the right. The contraction can be stored to simplify the calculation of longer range two-site density matrices—however, the optimal contraction sequence needs to be considered.

We compare results for the two-site mutual information for the strongly interacting ($U = 8$), half-filled system on a $l = 7$, $w = 4$ cylinder in fig. 3.19. The columns (rows) are ordered such that they correspond to "Z" mapping with linear momentum ordering, i.e. $[(x = 1, k = 0), (x = 1, k = 1), (1, 2), \ldots, (2, 0), (2, 1), \ldots]$. We thus expect to find the same distributions for all orderings at large bond dimensions.

The structure of the two-site mutual information is basically the same for both Z mappings, irrespective of their momentum ordering. As we had seen basically the same convergence behavior of the energy for both orderings in fig. 3.13, this is not very surprising. However, if one plots the mutual information using the original order of the MPS, using π separated momenta puts the strongly correlated sites closer to the diagonal.

If we look at the flipped "Z" map in figs. 3.19c and 3.19d, one can actually see a dependence on momentum ordering and bond dimensions. For π separated site ordering in momentum space we can see a similar structure of the mutual information as in figs. 3.19a and 3.19b—however, only for $U(1)$ bond dimensions $m \gtrsim 2.5 \times 10^3$. The state does not converge properly, the upper left corner shows a significantly different entanglement structure, even at the largest bond dimensions considered. The mutual information of the flipped "Z" map with linear momenta also changes significantly with increasing bond dimensions. However, the system does not converge to the ground state.

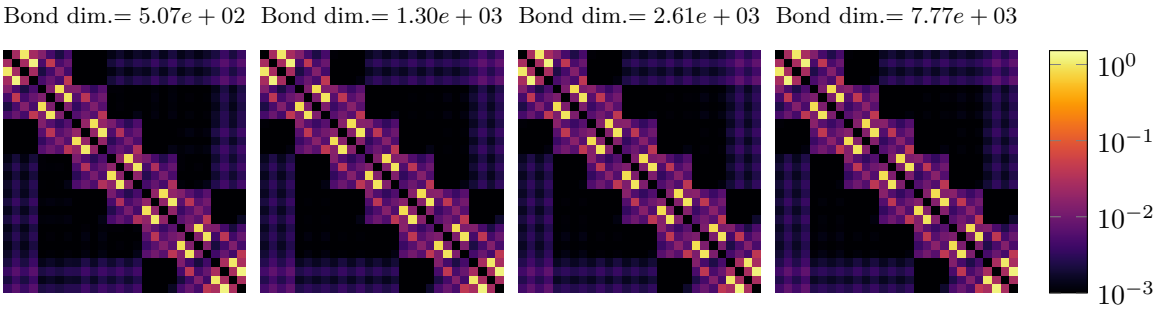

(a) Z mapping with linear momentum ordering.

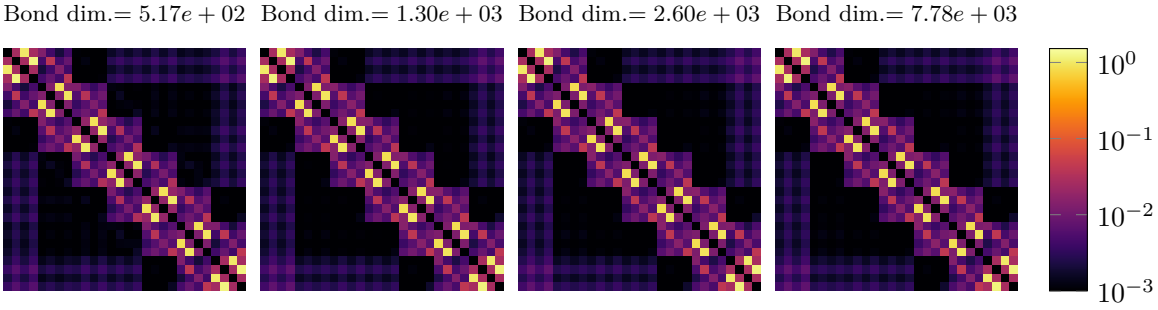

(b) Z mapping with π separated momentum ordering. Reordered to match (a).

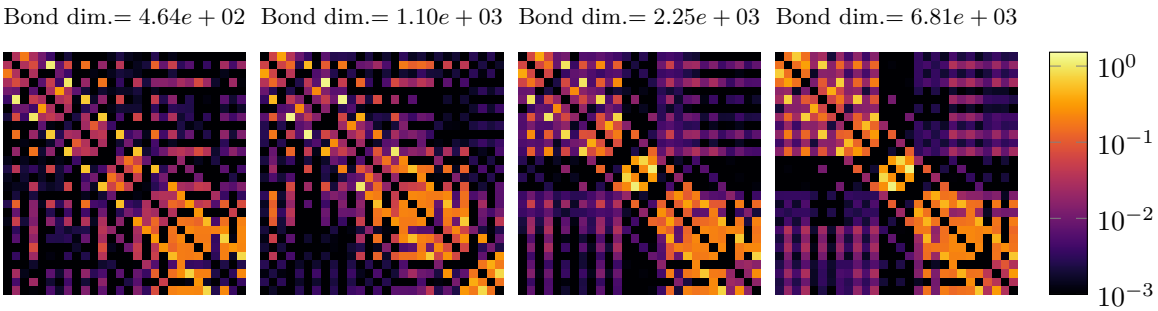

(c) Flipped Z mapping with linear momentum ordering. Reordered to match (a).

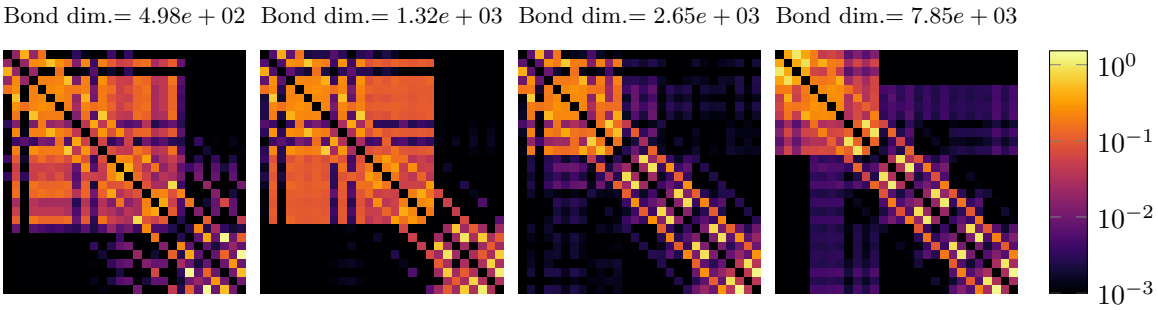

(d) Flipped Z mapping with π separated momentum ordering. Reordered to match (a).

Figure 3.19: Two-site mutual information $\hat{I}_{x,y}$ for different orderings at half filling. We chose strong interaction $U = 8$ on a cylinder of $l = 7$, $w = 4$. The rows and columns of all plots are reordered to match each other—i.e. we should find the same plots for the converged ground state, irrespective of the used map.

To quantify the total entanglement of a state we define the *entanglement distance*,

$$I_{\text{dist}}(\hat{\rho}) \coloneqq \sum_{i,j} I_{i,j}|i-j|^{\eta}, \tag{3.58}$$

where the sum goes over all sites in the MPS chain and the exponent is usually chosen as $\eta \approx 2 \dots 3$—we are not aware of physicals arguments for the choice of exponent. Once we find a reasonably converged state we can calculate the mutual information. We can thus minimize the entanglement distance by reordering the MPS chain. Assuming our inital map is reasonable such that we converge close enough to the ground state, we only need one simulation to find a better ordering.

Minimizing the entanglement distance is a hard problem as the number of permutations growths exponentially. A fast approach to this problem has been described by Fertitta et al. [63], based on a spectral algorithm for seriation from Atkins, Boman, and Hendrickson [64]. They consider R-matrices which are symmetric and decrease away from the diagonal,

$$a_{i,j} = a_{j,i} \qquad \text{and} \qquad a_{i,j} \leq a_{i,k}, \qquad \forall j < k < i. \tag{3.59}$$

If the rows and columns of a matrix A can be ordered such that it becomes an R matrix, it is called *pre-R*. Any such *pre-R* matrix can be reordered by sorting its *Fiedler* vector, which is the eigenvector corresponding to the second smallest eigenvalue of the Laplacian of A [64].

If we can reorder the MPS chain such that the two-site correlations are an R matrix then we have found a minimum of the entanglement distance eq. (3.58) *for any* $\eta > 0$. However, we find that the algorithm *cannot* yield an R-matrix for systems considered here. We therefore conclude that the mutual information matrix for our two dimensional systems is not pre-R. At half-filling there are very strong correlations between sites separated by $\Delta k = \pi$—which might allow for R ordering. For the doped system, see fig. 3.22, there is a wider spread of entanglement on the ring, such that the mutual information cannot be pre-R. We observe that sorting matrix according to the Fiedler vector generally decreases the entanglement distance,[13] anyway. However, the outcome very much depends on the initial order of the sites and if the matrix is not pre-R there need not be an ordering which minimizes the entanglement distance for all η—raising the question if we can motivate the exponent physically.

We want to compare the convergence in energy with a possible change of entanglement distance to see whether this is actually a good measure. In fig. 3.20 we compare the entanglement for different bond dimensions for the half-filled system we compared in fig. 3.12. The qualitative behavior is remarkably similar for the "Z" and "S" mappings with and without π separation, respectively. However, the reordered momenta always yield a lower entanglement distance. We observe barely any changes for "Z" ordering as the bond dimension increases. For "S" mappings the entanglement increases at some point. The behavior is not always monotonic for meander and flipped "Z" maps.

A similar comparison for the doped system can be found in fig. 3.21. For this case "S" and "Z" maps behave qualitatively very similar, the entanglement increases with the MPS bond dimension. From this plot it seems that π separated momenta are clearly advantageous and that the "Z" map would be significantly better than the "S" map. If we judge the different mappings only by the energy they converge to as in fig. 3.15, we do not observe as large differences.

[13] We considered exponent $\eta = 2$.

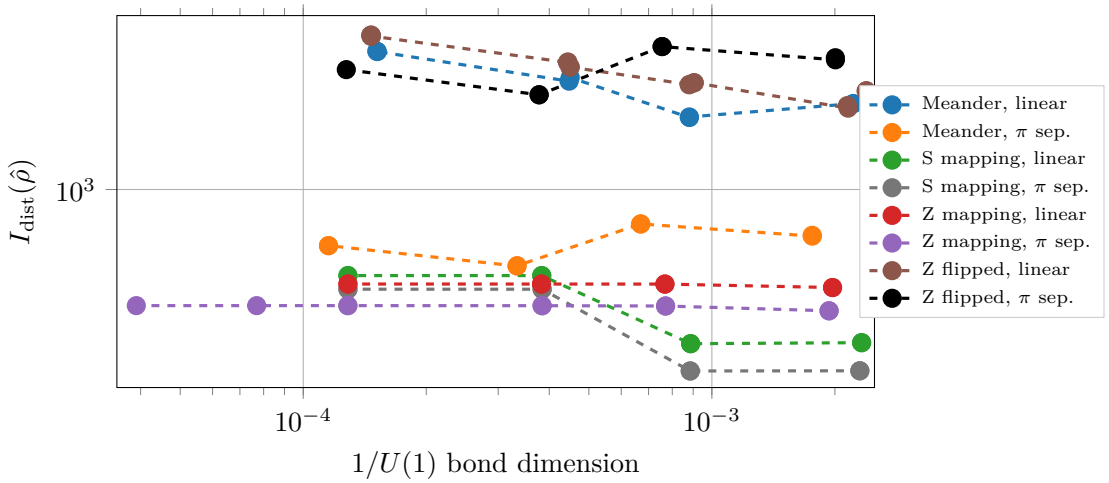

Figure 3.20: The total entanglement distance I_{dist} for different 2D $\rightarrow$ 1D maps varying bond dimension. We considered the same system as for fig. 3.12; strong interaction ($U = 8$) and half-filling on a $l = 7,\ w = 4$ cylinder.

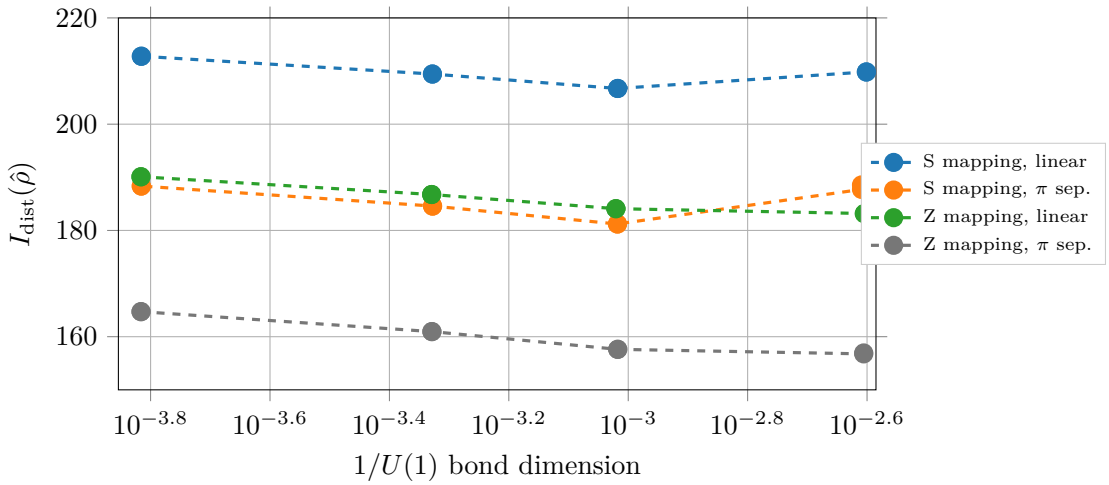

Figure 3.21: Entanglement distance for "S" and "Z" maps in the doped case. The system corresponds to the energies shown in fig. 3.15

If we look at the mutual information directly, we do not see clear advantages for any map. In fig. 3.22 the full two-site mutual information is plotted for the systems in fig. 3.21. For all orderings there is a significant spread of entanglement away from the diagonal. Using the Fiedler vector to reorder the MPS chain does not yield significant improvement (not shown). For all orderings the entanglement close to the diagonal primarily decreases with larger bond dimension and longer range correlations can appear.

Intuitively, we consider a mapping to be good (for the MPS) if the state can be represented most accurately at low bond dimensions. If the entanglement distance was a good measure for the efficiency of a map, we would expect it to grow as the bond dimension is increased, since the state is represented more accurately. It thus puzzles us that for some maps the entanglement decreases as the bond dimensions are increased, see fig. 3.20. We thus want to find a way to tell whether a change of order would be beneficial in that the state can be represented with smaller MPS bonds.

We propose **dynamic reordering** DMRG as a method to find an efficient MPS representation of inhomogeneous systems. The idea is most straightforward in terms of the two-site DMRG algorithm. We obtain a new rank four tensor by finding the minimal eigenvalue λ from the equation in fig. 3.8.

The two-site tensor then needs to be split into two MPS tensors by a singular value decomposition such that we can truncate the smallest values. At this point we have direct access to the singular value spectrum. We can thus easily see how many singular values we need to keep in order to reach a given error. We can also calculate the spectrum of singular values for the case that the order of both sites was switched—the details will be explained in a moment. If switching both sites yields a faster decaying spectrum of singular values, we can represent the state more accurately in a given bond dimension. As the SVD spectra on all other sites remain unchanged, the switched order is *better* than the previous one.

An algorithm for switching two adjacent sites after a variational update is sketched in fig. 3.23. In **A** the "normal" DMRG algorithm is depicted, we perform an SVD and can then truncate the singular values, represented by the diamond shaped matrix. Intuitively, we need to exchange the two physical legs to arrive at the tensor which represents the switched order. As we must not change the physical state described by the MPS chain, we need to change the order of the physical legs of the MPO representation of our Hamiltonian, as well.

In fig. 3.23 (**B**) we denote the MPOs which switch the physical legs by $\hat{X}$. As we consider fermions, switching two operators introduces a minus sign and the appropriate tensor blocks should change their sign to keep MPS and fermionic order the same. We contract with the optimized two-site tensor to arrive at a rank four tensor we perform SVD on, just like in the normal case. To find the new MPO tensors, we need to split the second switching tensors $\hat{X}^{-1}$ into two single-site MPOs using SVD. Contracting these (from below and above) with the MPOs of the original Hamiltonian we find the corresponding new MPO tensors. We can now compare the singular value spectra of **A** and **B**. A spectrum is favorable if it decays more quickly. This can be compared in terms of the Rényi entropy S^α, in particular using the Shannon entropy which is just S^1.

We note that this is a special case of the method for basis optimization described by Krumnow et al. [65]. They consider the application of more general[14] unitary transformations onto the optimized two-site tensor from DMRG. The transformation is chosen such that it minimizes a cost function—the authors use some norm of the Schmidt spectrum of the transformed two-site tensor. This approach has its downsides: finding the optimal unitary

[14] Symmetry protecting.

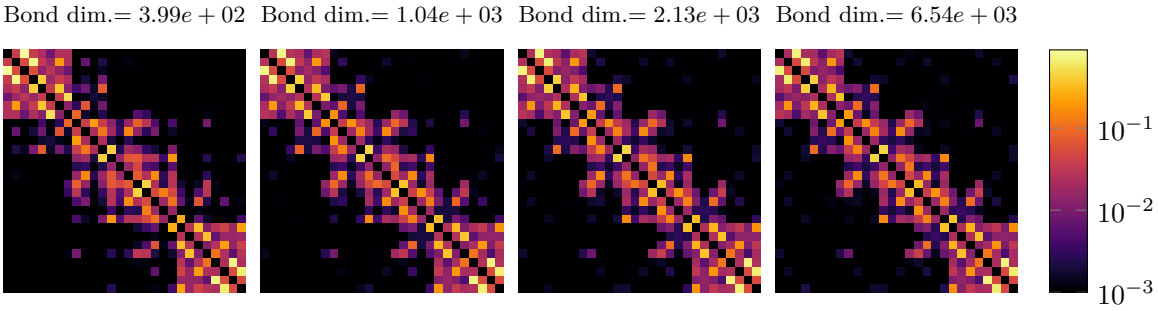

(a) S mapping with linear momentum ordering.

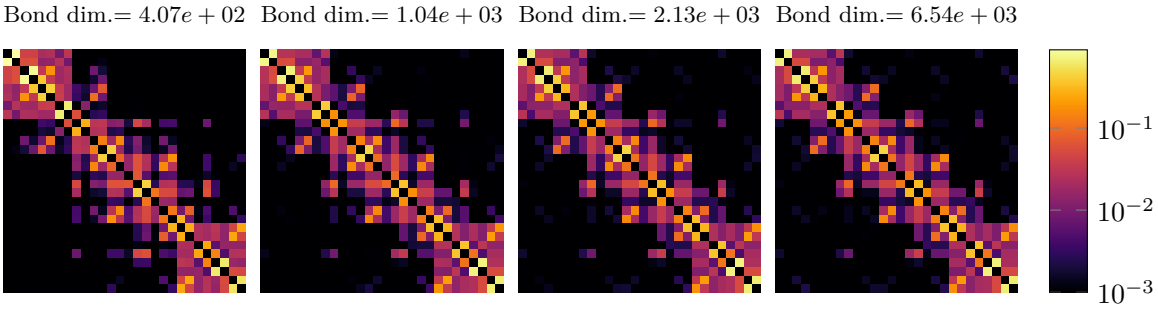

(b) S mapping with π separated momentum ordering.

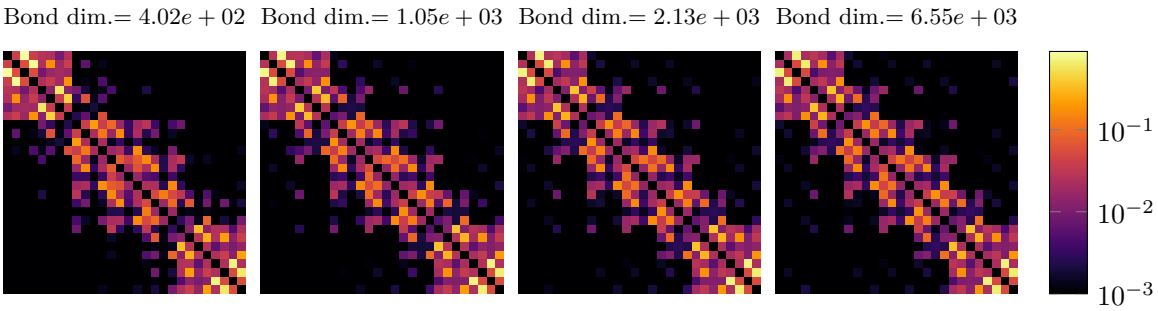

(c) Z mapping with linear momentum ordering.

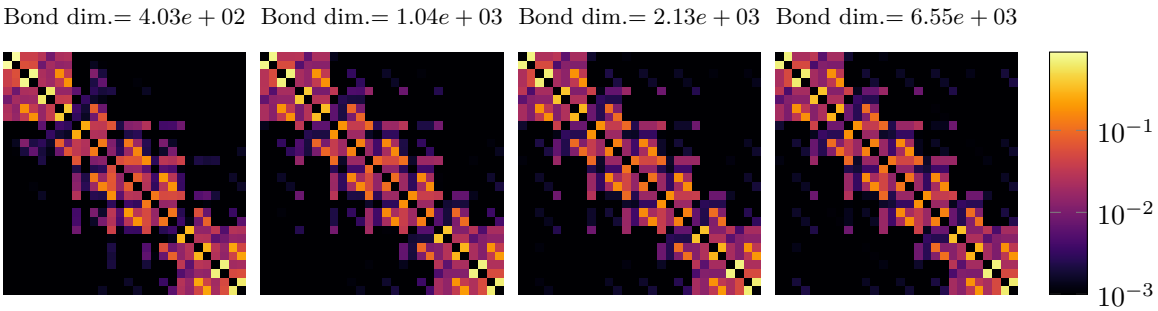

(d) Z mapping with π separated momentum ordering.

Figure 3.22: Two-site mutual information $\hat{I}_{x,y}$ for different orderings at doping $1 - n = 1/7$. We chose strong interaction $U = 8$ on a cylinder of $l = 7,\ w = 4$. Unlike in fig. 3.19, the entries are *not* reordered to match each other. π separated momenta lead to a slightly more diagonal form, but there are no significant advantages for any mapping.

transformation is costly as one needs to calculate the singular value spectrum for every candidate. And while they were able to find unitaries such that the same precision could be reached with MPS bond dimensions over an order of magnitude smaller, this does not *necessarily* speed up calculations. The transformations need to be applied to MPO tensors as well and thus the MPO bond dimensions *generally* increase.

Our approach would only require two SVD operations in order to decide whether to switch both sites. Furthermore, our transformations are not such that they could put all information of the state into the operator: an optimized MPS cannot become a product state, and the MPO bond dimensions should not increase too much. We do not know whether this approach could actually find the optimal ordering, it is very likely to get stuck in local minima. Krumnow et al. [65] additionally employed site reordering based on mutual information patterns. So far, we have only tried dynamic reordering for the single site algorithm DMRG3S. In this case we could not observe convergence to an optimal site-ordering—there were many transpositions during the first sweeps but they seemed rather random and the order stayed mostly fixed for later stages. We have some hope that the two-site algorithm might be advantageous for dynamic reordering: we only optimized a single MPS tensor, thus it is not as obvious that this minimization can actually yield a preferred order of the adjacent sites. Furthermore, single site DMRG requires subspace expansion in order to converge. We consider it to be possible that these mixing terms contribute to the Schmidt spectrum such that switching sites becomes less likely.

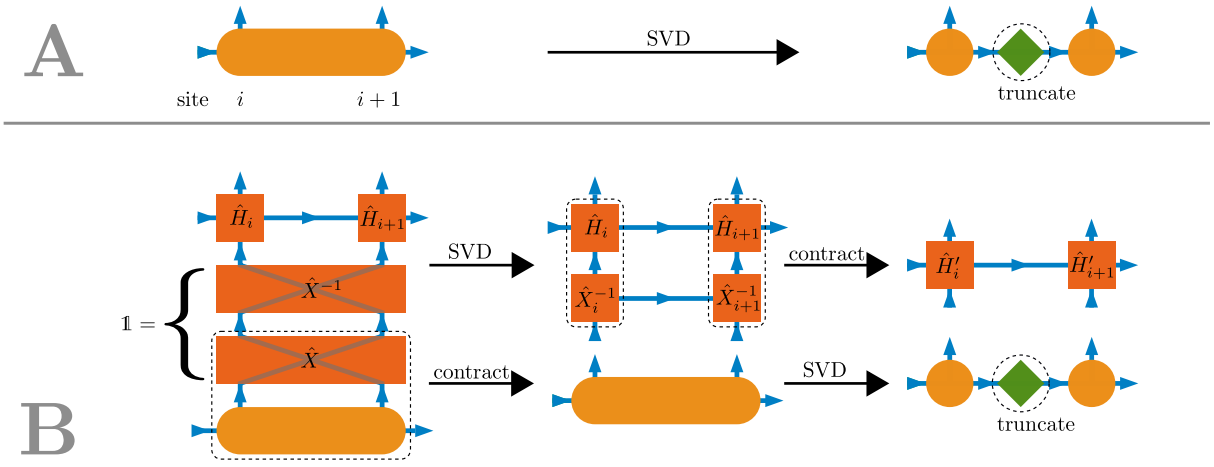

Figure 3.23: Splitting the two-site tensor from fig. 3.8—with (**B**) and without (**A**) exchanging both sites. To change the order of both sites, we introduce unitary operators $\hat{X}$ which exchange both sites in the MPS chain and in the Hamiltonian. Note that these exchange operators also need to be applied on $\hat{H}$ from above. After contractions and SVD the physical state represented by the MPS remains *unchanged*. However, the singular values in the circled, green matrix are not the same.

4 Discussion of results

In this chapter we discuss our own numerical results for the two dimensional Fermi-Hubbard model. We use the hybrid space DMRG method with $SU(2)$ spin symmetry as described in chapter 3. Our computations were performed on clusters of the Arnold Sommerfeld Center and the Leibniz Supercomputing Centre. Depending on system size and thus required bond dimension, each simulation took about a few days to a month of wall time. Our toolkit is parallelized on multiple levels: firstly, we employ several *workers* which perform optimizations simultaneously on different segments of the MPS chain as described by Stoudenmire and White [66]. Furthermore, the tensor contractions reduce to operations on *blocks* which can be performed in parallel and also the dense operations on each single blocks can be parallelized—if the matrices are sufficiently large. For our calculations at very high bond dimensions while employing multiple symmetries, parallelization on tensor block level was most effective. The dense matrices were usually too small to allow for efficient computation in parallel. In many cases the available memory limited the bond dimensions we could achieve.

In the first section we will check our calculations by comparing ground state energies to the previously mentioned benchmark results by LeBlanc et al. [34]. Wherever possible, we will show more recent results by Ehlers, White, and Noack [48] who also did hybrid space DMRG. Furthermore, we will discuss occupation profiles regarding the possible formation of stripes.

Unlike most previous DMRG calculations, we enforce $SU(2)$ symmetry explicitly. While this allows for larger effective bond dimensions, we cannot apply an external field to *pin* the orientation of spins as it would break this symmetry. Therefore, we can only measure vanishing local spin expectation values (e.g. $\langle \hat{S}^z \rangle = 0$). Instead, we measure spin *correlators* of sites on different cylinder rings. These results are shown in section 4.2 for spin and for occupation correlators in real space.

As DMRG gives access to the wave function, we can measure all kinds of local observables. In section 4.3 we project the Hamiltonian onto single cylinder rings to measure local energies of each ring. We show how this method could be used to reduce effects of the open boundaries. Eventually, we discuss the possibility of *phase separation* at small dopings $n \approx 0.9 \ldots 0.93$ in section 4.4. We interpret our results on long but thin cylinders in terms of simple thermodynamic arguments presented in section 1.5.

4.1 Validating our numerical method

In symmetry protected DMRG we need to choose the symmetry sector of the matrix product state explicitly, i.e. the outgoing MPS legs needs to carry the symmetry labels matching those of the true ground state. This is fine for the particle number $U(1)$ symmetry, after all we want to control doping as it is a parameter which can be modified in experiment. Selecting the right $SU(2)$ spin sector does not pose difficulties, either. The ground state is always the $S = 0$ singlet. But for quasi-momentum k we do not know the ground state sector a priori.

One might expect to find the ground state in a low momentum state. Indeed, for half filling $n = 1$ the ground state is always of quasi-momentum $k = 0$. An example for "ground state" energies in different momentum sectors is shown in fig. 4.1. These data points were obtained through simulation of a *diagonal* two-dimensional lattice, but the qualitative behavior is the same for square lattices. We observe that linear extrapolation in reciprocal cylinder length $1/l$ indicates that $k = 0$ would not be the ground state in the thermodynamic limit—however, this is more likely to be an indication for the breakdown of linear extrapolation. We assume that the region where the energy goes as $1/l$ does not depend on the length directly, but rather on the aspect ratio of the cylinder. This would explain why we cannot observe such crossings of linear extrapolations for *wider* cylinders. Nonetheless, the difference in energy between quasi-momentum sectors becomes *smaller* as the system length increases. This can be understood as the difference in quasi momentum spreads over more rings corresponding to smaller changes per ring.

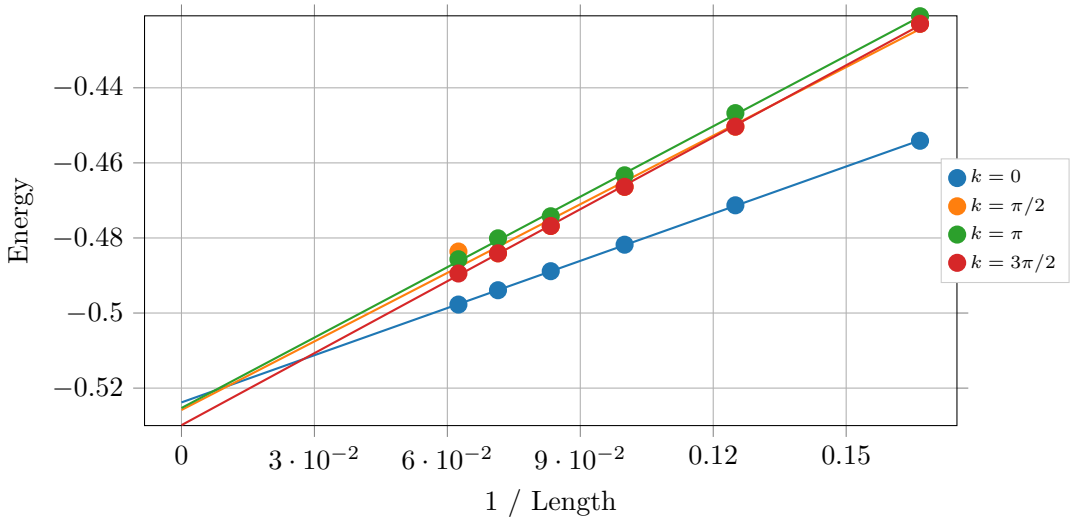

Figure 4.1: DMRG results for different momentum sectors for the half-filled system with strong interaction $U = 8$ in *diagonal* hybrid space. We chose width $w = 4$ and varied cylinder length. The ground state is in the $k = 0$ sector for all systems considered, but the difference vanishes with increasing cylinder length. The linear extrapolation seems to be accurate for all calculations performed, however we assume it breaks down at $l \approx 30$ where the extrapolated lines cross.

Below half-filling the different quasi-momentum sectors become closer in energy. Results for the diagonal lattice at half filling and smaller interaction $U = 4$ is shown in fig. 4.2. While $k = 0$ appears to be the ground state for short systems, quasi-momentum π becomes advantageous for longer cylinders. If the quasi-momentum of the ground actually depends on aspect ratio rather than cylinder length, $k = 0$ might still be the ground state in the thermodynamic limit. The energies of $k = \frac{\pi}{2}$ and $k = \frac{3}{2}\pi$ are degenerate to our precision. We observe this (near) degeneracy for many calculations at $w = 4$, but we cannot make such observations for wider cylinders as our results are not precise enough.

For the square lattice in hybrid space, we find similar results. In fig. 4.3 there are nearly degenerate energies for quasi-momenta $\frac{\pi}{2}$ and $\frac{3\pi}{2}$. There also seems to be a change of ground state momentum sector as the length increases—but we cannot say definitively whether $k = 0$ or $k = \pi$ is the ground state sector.

We conclude that one can assume $k = 0$ to be the ground state *only* at half-filling. As dopants are introduced, this is no longer true, the ground state can be of higher quasi-momentum.

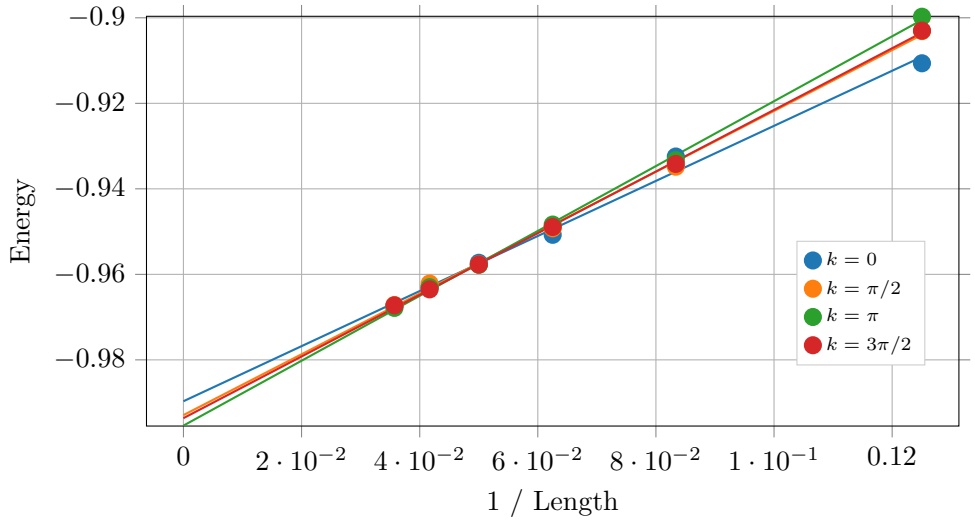

Figure 4.2: DMRG results for different momentum sectors for the doped system $n = 7/8$ with moderate interaction $U = 4$ in *diagonal* hybrid space. The energies are very close, it seems that $k = 2$ becomes the ground state at longer lengths. The other two sectors, $k = 1$ and $k = 3$ are nearly degenerate.

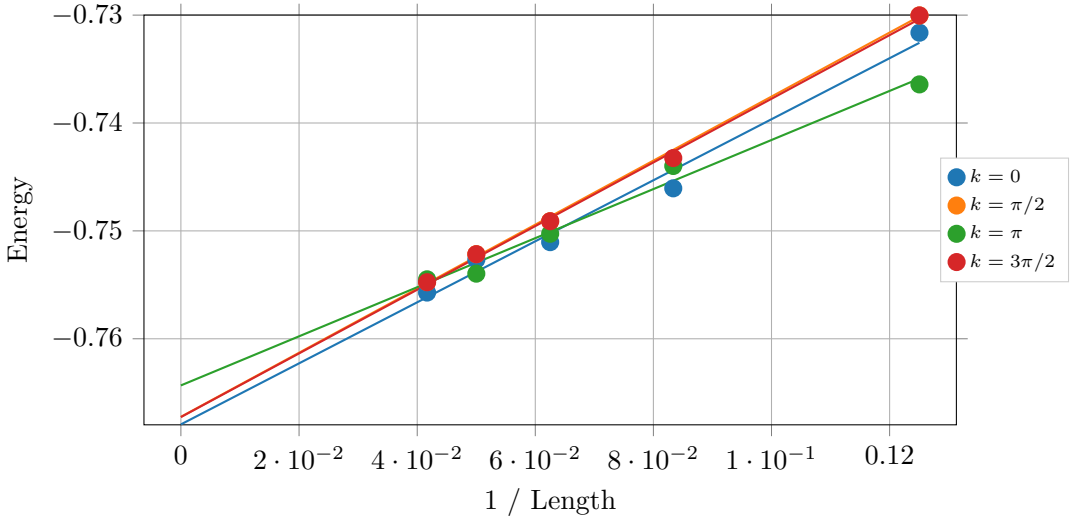

Figure 4.3: DMRG results for different momentum sectors for the doped system $n = 7/8$ with strong interaction $U = 8$ in hybrid space. Quasi-momentum sectors $k = \pi/2$ and $k = 3\pi/2$ are nearly degenerate.

It appears that sectors $\frac{4\pi n}{w}$, $0 \leq n < w/2$ are usually lowest in energy—however our results for cylinders of width $w = 6, 8$ are not very clear. We often restrict ourselves to performing DMRG for this half of the possible momentum sectors and then "choose" the lowest energy result to be the ground state. If there is no a priori method to find the true ground state momentum sector, the computational cost is higher: in section 3.3.1 we presented the estimate by Ehlers, White, and Noack [48], but if we have to perform $\mathcal{O}(w)$ many DMRG calculations, the cost increases by this factor.

4.1.1 Comparison of energy results

During the implementation of the $SU(2)$ symmetric hybrid space DMRG method we have checked that its results agree with both real space calculations and simulations with lesser (i.e. S^z, $U(1)$ symmetry or none at all) spin symmetry. We have also observed that different momentum sectors yield different, but consistent energies—our simulation thus appears to be correct, but how does it compare to numerical results from other groups?

We start by looking at the numerically simple case of half-filling. There is no sign problem for quantum Monte Carlo and also DMRG calculations tend to converge faster and require only smaller bond dimensions. Energies for the case of strong interaction are shown in fig. 4.4. Our results show a very precisely linear dependence of energy on cylinder length—even for real space simulations of width $w = 8$ where we do not usually find well converged results. The diagonal lattices in hybrid space yield significantly higher energies but we assume this to be a result of the different geometry. The diagonal lattice of width $w = 4$ allows for linear extrapolation in reciprocal length, yielding energies very close to the results for square lattices. However, the wider diagonal lattice does not show a clear linear trend. One could explain this behavior by a lack of convergence, but we find results which are not proportional to $1/l$ for most diagonal lattices, even for very small systems of width $w = 2$ (not shown).

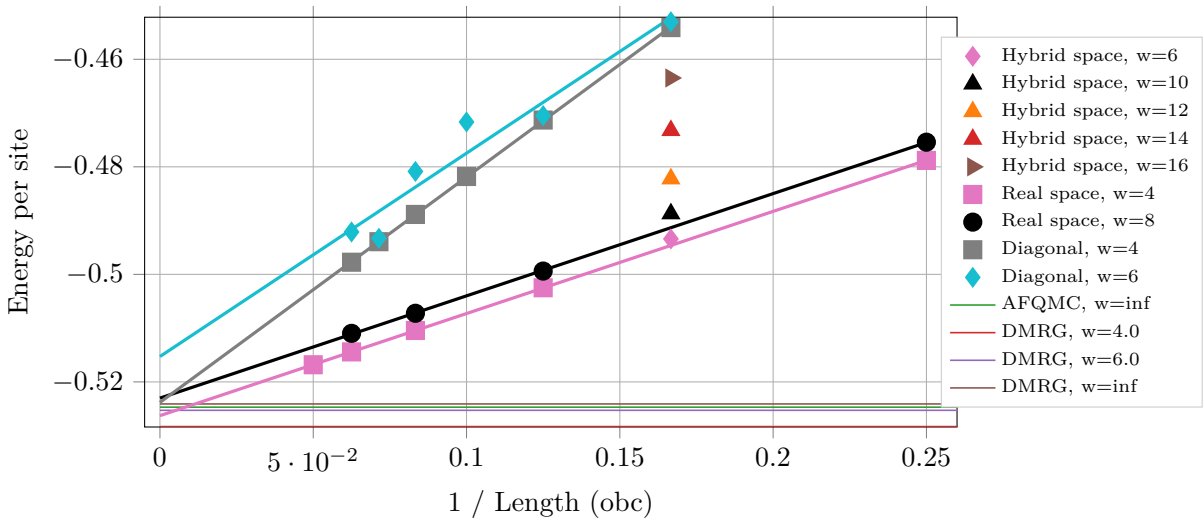

Figure 4.4: Ground state energies for the half-filled Hubbard model with strong interaction $U = 8$. We compare different cylinder lengths and widths. Filled symbols are results from our calculations, the vertical lines are *extrapolated* results from LeBlanc et al. [34].

The energies from LeBlanc et al. [34] using DMRG and auxiliary field quantum Monte Carlo (AFQMC) are slightly lower than our results—the reasons are twofold. For once, they

use a different lattice geometry: instead of using periodic boundaries along the cylinder rings, they average over both periodic and antiperiodic boundary conditions as a simple form of "phase averaging". More importantly, their results are *not variational* but they extrapolate the energies to zero truncation error. For these reasons we consider our energies, even though slightly higher, to be accurate.

In fig. 4.4 there are a few additional data points for wider, but very short $l = 6$ cylinders, calculated in hybrid space. The energies appear to scale quadratic or cubic in reciprocal width. This is consistent with cubic scaling found by LeBlanc et al. [34] and can be motivated by finite-size scaling of the Heisenberg model (see Sandvik [67]).

We find qualitatively identical results for the case of smaller interaction $U = 2$, which are shown in fig. 4.5. For these parameters we compare real- and hybrid-space approaches and find that the hybrid space approach yields better results. For the numerically challenging case of width $w = 8$ the hybrid space energies are always smaller and the difference increases with cylinder length. Compared to LeBlanc et al. [34], our energies for $w = 8$ are rather high, indicating insufficient bond dimensions of our simulation. The energies of the diagonal lattices are significantly larger than for square lattices. While this might be correct, we do not observe a clear $1/l$ proportionality of the energy and can hardly perform accurate extrapolation. For this reason, we did not consider diagonal lattices for any further calculations.

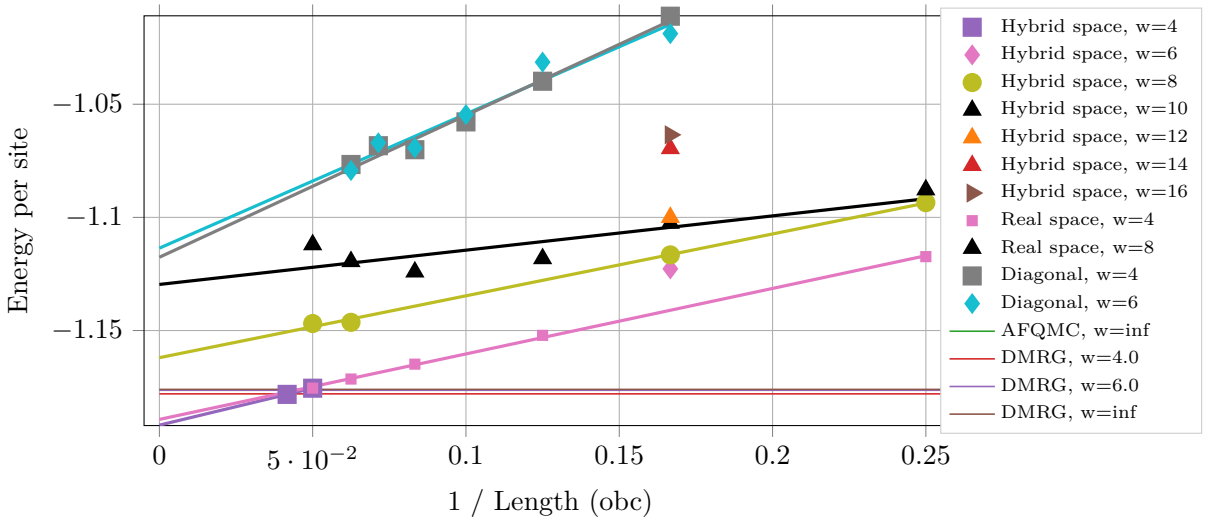

Figure 4.5: Comparison of results for the half-filled Hubbard model at weak interaction $U = 2$. Filled symbols are results from our calculations, the vertical lines are *extrapolated* results from LeBlanc et al. [34]. Extrapolated energies DMRG and AFQMC cannot be discerned at this scale.

We turn to the more challenging case of doped systems. In order to fit the experimentally observed cuprate phase diagram (see fig. 1.2), particle number $n = 7/8$ is a common choice which might exhibit interesting (superconducting) behavior. For weak interaction $U = 2$, shown in fig. 4.6, we once more find lower energies if we use hybrid space rather than real space. But it is likely that the true ground state energy is even lower and would require larger bond dimensions. As there were no AFQMC or DMRG results presented in LeBlanc et al. [34], we instead show energies for the thermodynamic limit computed using fixed-node Monte Carlo and density matrix embedding theory (DMET).

Finally, we consider the parameters which are probably most relevant and most frequently studied: the doped system with strong interactions. This case is particularly interesting

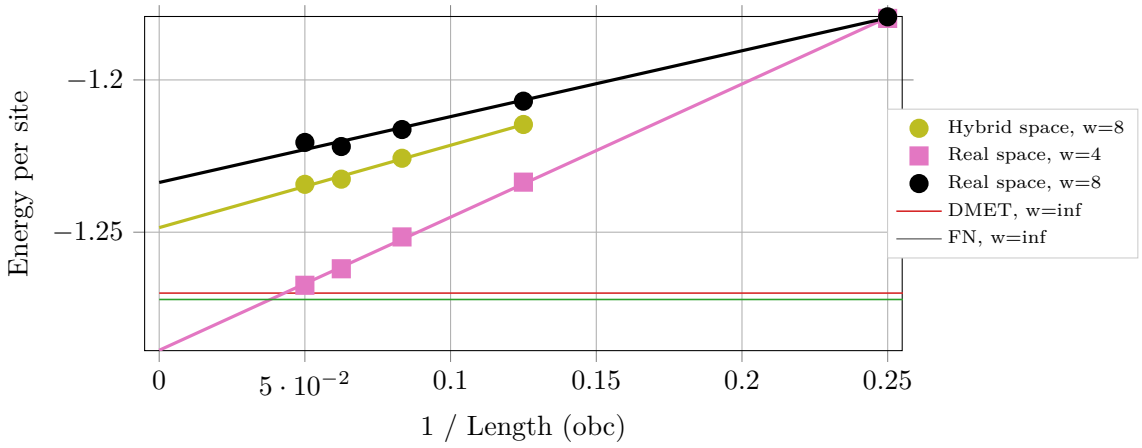

Figure 4.6: Energies for the doped Hubbard system $n = 7/8$ at weak interaction $U = 2$. As there were no DMRG and AFQMC results presented in LeBlanc et al. [34], we compare our results to those from DMET and fixed-node Monte Carlo (FN).

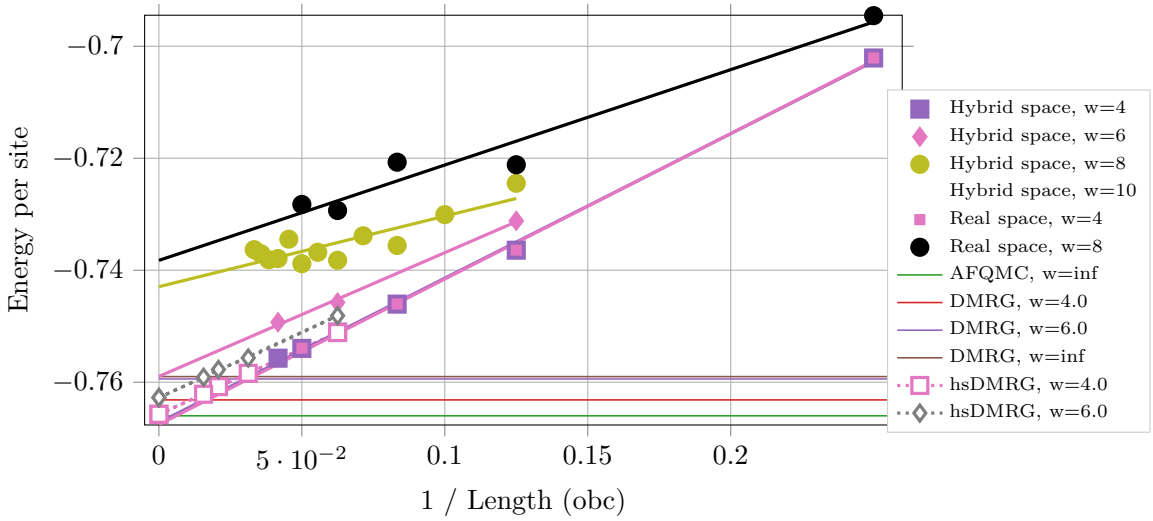

Figure 4.7: Comparison of results for the doped $n = 7/8$ Hubbard model at strong interaction $U = 8$. In addition to results published by LeBlanc et al. [34] (vertical lines) we show hybrid space energies from Ehlers, White, and Noack [48] as hollow symbols (hsDMRG).

for comparison as these parameters have also been studied by Ehlers, White, and Noack [48] in hybrid space. Our results and those by LeBlanc et al. [34] and Ehlers, White, and Noack [48] are plotted in fig. 4.7. For width $w = 4$ all results for finite length agree well, the energy extrapolated to $l = \infty$ by Ehlers, White, and Noack [48] are slightly higher. Their results might be more accurate as they performed calculations on longer lattices where the corrections to $\propto 1/l$ become relevant—possibly $\propto 1/l^3$ as for the extrapolation $w \to \infty$. Both results by Ehlers, White, and Noack [48] and by us (real space and hybrid space) for $w = 4$ indicate lower energies than the corresponding DMRG energy published in LeBlanc et al. [34].

It is more difficult to draw conclusions for wider cylinders. For $w = 8$ we were unable to represent the ground state—while the hybrid space energies are lower than the ones we found in real space simulations, the energies are clearly not converged. To our knowledge there are no DMRG results for such large widths, but initially we had hoped that $SU(2)$ symmetry would make these computations feasible.

However, there are results for width $w = 6$—most notably the hybrid space DMRG results by Ehlers, White, and Noack [48]. As shown in fig. 4.7 (dashed, gray line), they allow for a clear extrapolation to $l = \infty$ and yield a notably lower energy than was published by LeBlanc et al. [34]. Having performed only few calculations at this width, we cannot perform a definite extrapolation—but our energies are clearly higher than the ones published by Ehlers, White, and Noack [48]. The plotted data points seem to indicate that our method is on par with real space DMRG results from LeBlanc et al. [34] but less accurate than the competing hybrid space method.

The differences for the hybrid space calculations solely stem from extrapolation: the results by Ehlers, White, and Noack [48] are extrapolated in truncation error. In fig. 4.8 we add two energies at different bond dimensions from our calculation. As we cannot determine a *meaningful* truncation error, the positioning of the points along the $\Delta\xi$-axis is purely suggestive. We see that our energies match their results very well. One should note that the bond dimensions are given in terms of S^z symmetric states—such that a $U(1)$ bond dimension of $40 \cdot 10^3$ corresponds to $15 \cdot 10^3$ $SU(2)$ symmetric states.

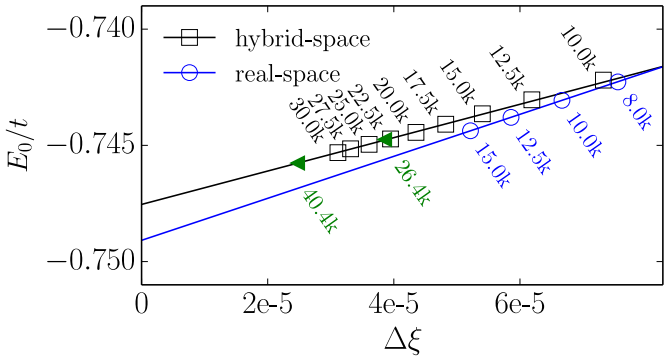

Figure 4.8: Extrapolation in the truncation error performed by Ehlers, White, and Noack [48]. We added two energies (green triangles) our calculations found for the given $U(1)$ bond dimensions—however, we cannot determine the corresponding truncation error $\Delta\xi$. The position of the triangle is thus only meant as guide for the eye.

In conclusion, our method yields variational energies which are smaller than real space results by LeBlanc et al. [34] and on par with those by Ehlers, White, and Noack [48]. Enforcing $SU(2)$ symmetry, we only need to work with reduced tensors and can thus achieve larger bond dimensions. Judging from the comparison in fig. 4.8, exploiting spin symmetry seems to work well—but we do not have further data for a direct comparison.

But there are obvious problems with our method. Most importantly, we cannot determine meaningful errors for our data points. As we pointed out in section 3.2, we cannot properly compute the truncation error with single-site DMRG. While the variance of the energy (see section 3.3.2) could be used as error estimate, its computation is too costly for states at large bond dimensions. Judging from the extrapolated results presented in LeBlanc et al. [34], most other methods also fail to give correct errors. As DMRG is a variational method, at least we know that DMRG energies are an upper bound to the ground state energy of the finite system.

The lack of meaningful truncation errors also means that we cannot perform extrapolation in the truncated weights as done by Ehlers, White, and Noack [48] and most other papers of the authors. However, we can consider the dependence of energy on bond dimensions. Results for the doped, strongly interacting system of width $w = 8$ at different lengths are shown in fig. 4.9. For most other calculations we do not have "converged" intermediate results as we increased the bond dimension too quickly.

The linear fit seems appropriate for some lengths, e.g. for $l = 8$, $l = 16$, $l = 22$ but we should not assume it to be correct. For length $l = 10$ the straight line does not match the measured energies and also the results by Ehlers, White, and Noack [48] shown in fig. 4.8 indicate a non-linear dependence on bond dimension. If we extrapolated the energy to infinite bond dimension before extrapolating the results in system length (as shown in fig. 4.7), we would find a ground state energy very close to -0.76, consistent with results from LeBlanc et al. [34]. But as we employ two extrapolations which are in no way "obvious" or physically motivated, the error would be very large.

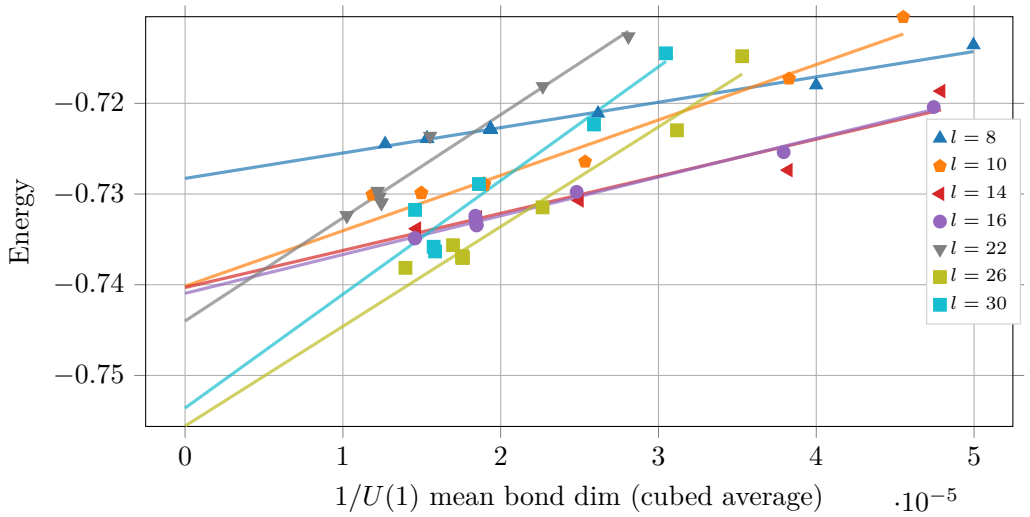

Figure 4.9: Intermediate energies for the doped $n = 7/8$ Hubbard model with strong interactions $U = 8$ on a cylinder of width $w = 8$ for varying bond dimensions and cylinder lengths. Linear fits are shown, however they only match for *some* cylinder lengths. Many energies are likely not converged such that this plot is merely a proof of principle but should not be used for quantitative conclusions.

Matrix product states work particularly well for one-dimensional systems where the spectrum of singular values tends to decay exponentially. In that case we would expect the truncation error defined in eq. (3.25) to decay exponentially, as well,

$$\epsilon^2 = \sum_{\alpha_i=\beta_i}^{\infty} \left(S_{\alpha_i}{}^{\alpha_i}\right)^2 \approx \int_{\beta_i}^{\infty} \mathrm{d}\,\alpha_i\, \mathrm{e}^{-2\gamma\alpha_i} = \frac{1}{2\gamma}\, \mathrm{e}^{-2\gamma\beta_i}\,. \tag{4.1}$$

For example Ehlers, White, and Noack [48] who performed two site DMRG on hybrid space Hubbard cylinders found linear dependence of energy on truncation error. It is thus possible that an exponential fit might have produced more accurate results in fig. 4.9. We also tried this fitting procedure but could not find convincing results: the least-squares fit generally could not determine the decay rate γ accurately. We could choose appropriate values manually, however it seems that the rate depends on system *length*. As we do not have many reliable intermediate results, we cannot improve our extrapolation by introducing additional fitting parameters.

It is also not clear that we can actually assume exponential decay of singular values in two dimensional systems, i.e. if eq. (4.1) is a valid estimate. As an example, we plot the singular value spectrum for the doped 10×4 Hubbard model at intermediate interaction in fig. 4.10. We do not observe a linear decrease in the semilogarithmic plot but the slope gets flatter as the singular values become smaller. The decay rate also tends to decrease for consecutive simulation stages with constant maximal bond dimension. We interpret these observations such that DMRG tries to approximate a polynomially decaying singular value spectrum. While we have calculated various larger systems at higher bond dimensions, these do not allow fast access to the entire spectrum of singular values for technical reasons.

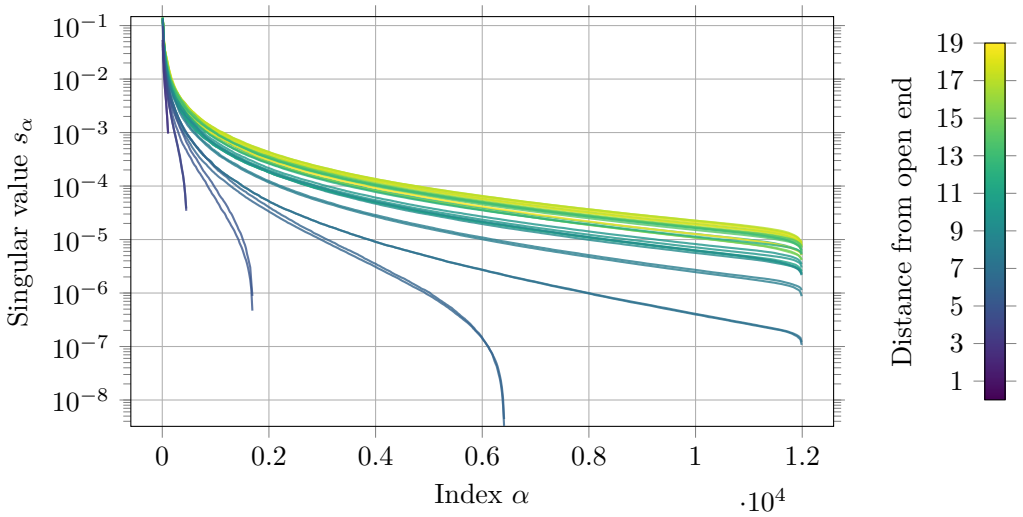

Figure 4.10: Spectrum of singular values for a 10×4 Hubbard system with interaction $U = 4$ at particle number $n = 0.9$. We limited the calculation to 12000 $SU(2)$ states. The bonds close to the open ends do not exhaust the maximal number of states. Apart from the smallest singular values, we can only find polynomial decay.

4.1.2 Occupation densities

We can hardly put error bars on our results, therefore it is particularly important to know that we are at least "close" to the true ground state. We try to judge convergence by measuring cheaply available local observables: if these results are "inconsistent", we probably have not achieved convergence.

As an example, we want to consider the occupation of each ring. We have open boundaries on both ends which tend to attract electrons. Therefore, an eigenstate of $\hat{H}$ need not have

constant particle number,[1] but we might expect the profile to be invariant as we flip the cylinder. A symmetric density profile is neither necessary nor sufficient to tell that we found the ground state: a phase separated state might not be symmetric but a uniform excited state would be.

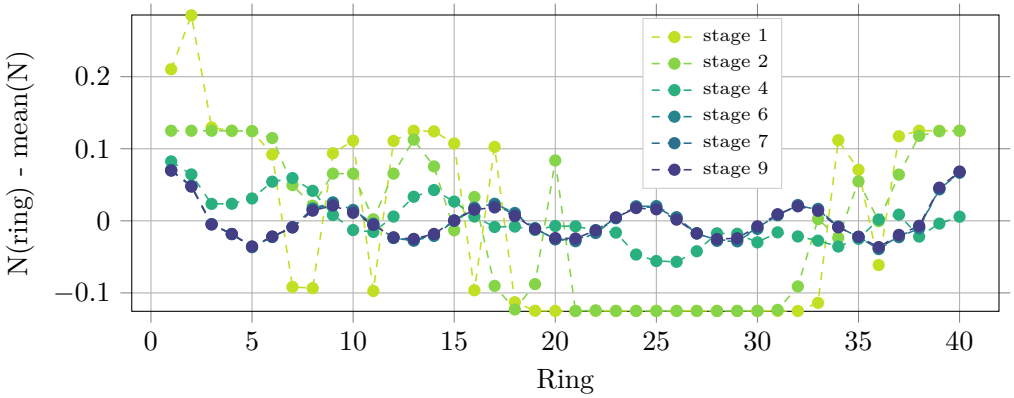

(a) Cylinder of length $l = 40$ and interaction $U = 6$. The profile appears to become periodic.

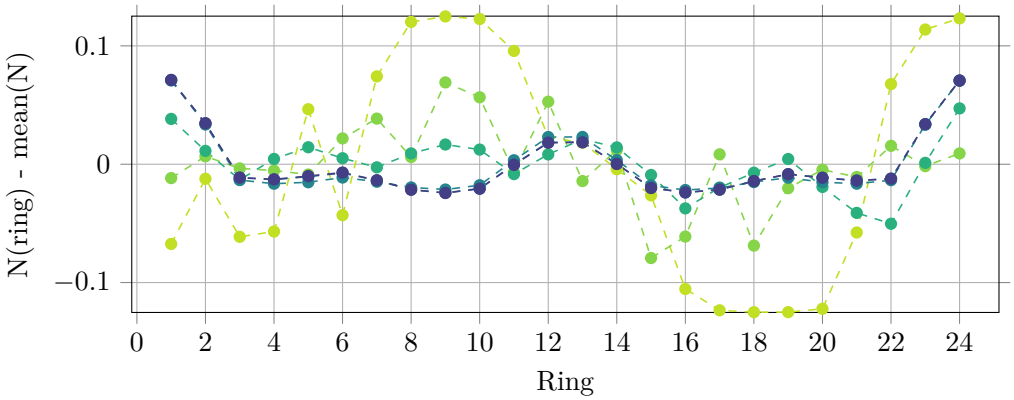

(b) A shorter cylinder at interaction $U = 4$. The profile is not periodic but highly symmetric. Coloring of the stages as above.

Figure 4.11: Occupation profile along the real space axis of the doped $n = 7/8$ Hubbard model of width $w = 4$ for different stages of the computation. Deviation from the mean occupations are summed up along each ring. We can observe how the profile becomes much more symmetric as the calculations converge.

Nonetheless, the fact that *local* DMRG optimizations yield a symmetric distribution on the entire cylinder is a strong sign for convergence. We plot particle numbers of each ring for intermediate stages of our computation in fig. 4.11 for different system lengths and interactions. One can observe how oscillations of the density become smaller and eventually converge to a highly symmetric pattern.

To quantify the inversion symmetry of density profiles, we perform a Fourier transform on the local particle number expectation values. The imaginary part of the Fourier components then corresponds to antisymmetric modes, real components to the symmetric part. We note that our profiles are not "periodic" in the usual sense: for discrete, symmetric data set x one would expect x[j] == x[l−j] where l is the length of the set and we count from zero.

[1] Momentum conservation enforces uniform real space occupation on each ring.

This is not the case for the data shown in fig. 4.11, instead we have x[i] == x[l−i−1] and we have to modify the Fourier transform accordingly.

If we transform such *symmetric* data set x with an even number of entries, we find a complex phase A_k,

$$\tilde{x}_k = \sum_{j=0}^{l-1} x_j \, \mathrm{e}^{-2\,\mathrm{i}\,\pi jk/l} = 2\underbrace{\mathrm{e}^{\mathrm{i}\,\pi k/l}}_{=A_k} \sum_{j=0}^{l/2-1} x_j \cos\left(2\pi k\left(j+\frac{1}{2}/l\right)\right). \tag{4.2}$$

As we multiply by $A_k^\dagger$, we restore the property that (anti)symmetric contributions correspond to purely (imaginary) real Fourier components. But "symmetric" is now defined in terms of trigonometric functions *shifted* by $\pi k/l$ which fulfill our expectations,

$$\cos\left(\pi k/l\right) = \cos\left(2\pi k\left(l-\frac{1}{2}\right)/l\right). \tag{4.3}$$

Note that we can employ the usual methods for fast Fourier transformations and only need to multiply the result with a phase A_k.

The imaginary parts of this Fourier transform are plotted in figs. 4.11a and 4.11b. The plots reflect the qualitative impression that the occupation densities are invariant under spatial inversion: all imaginary parts decay to zero meaning there are no antisymmetric components in the density profile.

Intuitively, one might quantify (anti)symmetry by calculating the norm of the (anti)symmetrized data set,

$$\left(x\big|_{\mathrm{s/a}}\right)_j = \frac{1}{2}\left(x_j \pm x_{l-j-1}\right). \tag{4.4}$$

But multiplying a phase A_k does not change that the Fourier transform is *unitary*.[2] Therefore, calculating the norm of the symmetrized data set $x\big|_{\mathrm{s/a}}$ is identical to calculating the norm of real (imaginary) parts of the transformed $A_k^\dagger \tilde{x}_k$,

$$\begin{aligned}
\|\Re(A_k^\dagger \tilde{x}_k)\|^2 &= \sum_{k=0}^{l-1} \left| \Re\left(\mathrm{e}^{-\,\mathrm{i}\,\pi k/l} \sum_{j=0}^{l-1} x_j \, \mathrm{e}^{-2\,\mathrm{i}\,\pi jk/l} \right) \right|^2 \\
&= \sum_{k=0}^{l-1} \left| \sum_{j=0}^{l/2-1} \cos\left(2\pi(j+1/2)k/l\right) 2\left(x\big|_s\right)_j \right|^2 \\
&= \sum_{k=0}^{l-1} \sum_{j,p=0}^{l/2-1} \left| \left(\cos(2\pi(j-p)k/l) + \cos(2\pi(j+p+1)k/l)\right) \left(x\big|_s\right)_j \left(x\big|_s\right)_p \right| \\
&= \sum_{j,p=0}^{l/2-1} \left| l\left(\delta_{j,p} + \delta_{j,l-p-1}\right) \left(x\big|_s\right)_j \left(x\big|_s\right)_p \right| = 2l \sum_{j=0}^{l/2-1} \left(x\big|_s\right)_j^2 = l \left\| x\big|_s \right\|^2 .
\end{aligned} \tag{4.5}$$

Thus, we plot the norms of symmetric and antisymmetric (real and imaginary) Fourier components for these systems in figs. 4.11a and 4.11b. We disregard the zeroth Fourier component as it corresponds to the mean occupation which is defined through the symmetry. As the bond dimension is increased during computations, these system converge well to the symmetric state and the corresponding Fourier components are two orders of magnitude larger.

[2] For DFT the normalization is typically chosen as $1/l$ in the inverse transformation, compare Press [68].

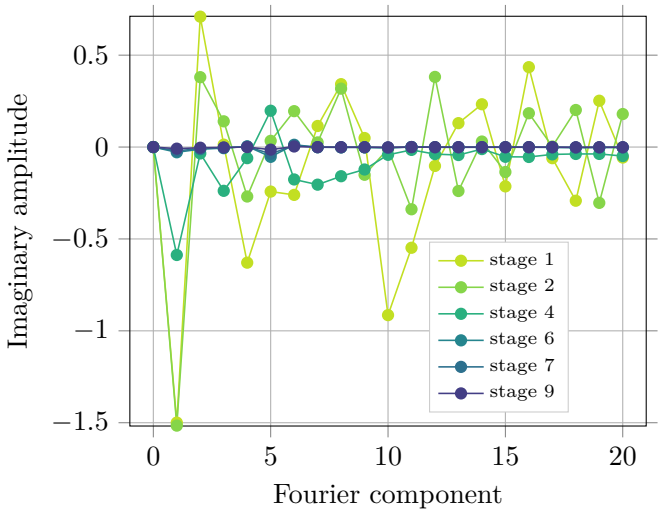

(a) Imaginary part of the Fourier transform of fig. 4.11a.

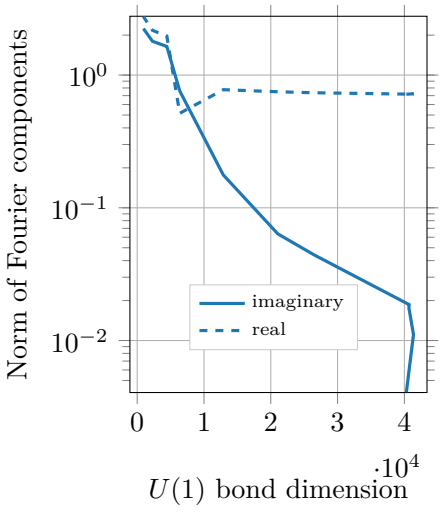

(b) Norm of the Fourier components versus bond dimension. The points are connected in order of the stages but the $U(1)$ bond dimension does not increase monotonously during simulation.

Figure 4.12: Fourier transform of the density profile from fig. 4.11a. The imaginary parts decay to zero, indicating *convergence* to a more symmetric wave function.

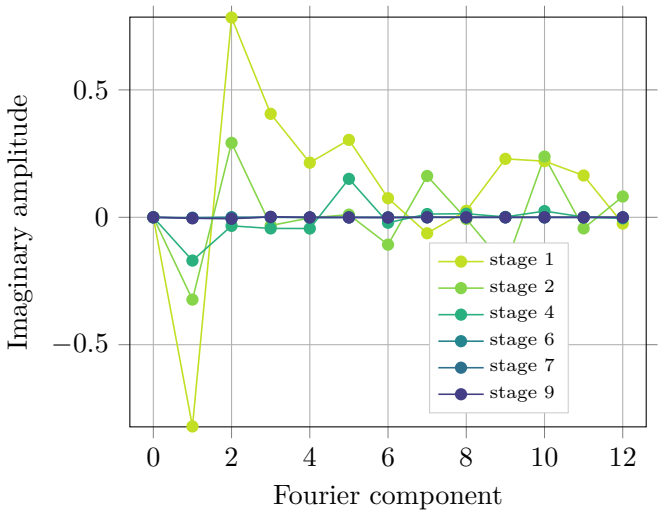

(a) Imaginary part of the Fourier transform of fig. 4.11b.

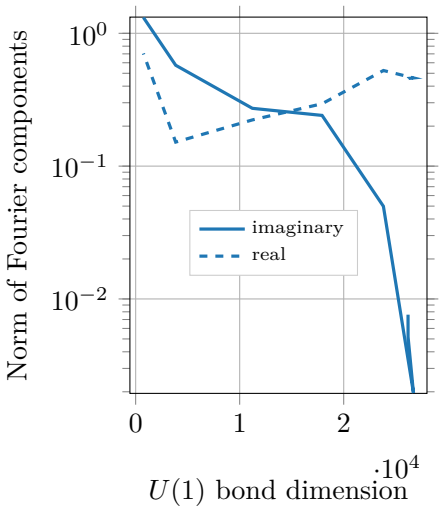

(b) Norm of the Fourier components versus bond dimension. The points are connected in order of the stages.

Figure 4.13: Fourier transform of the density profile from fig. 4.11b. Qualitatively the same observations as for fig. 4.12

Density profiles are not just an approach to estimate convergence—they can be of interest on their own. We need to return to the question of **stripes** we mentioned several times in section 2.2. Ehlers, White, and Noack [48] observe density patterns very similar to ours shown in fig. 4.11—and "obviously" interpret these as stripes. They find a wavelength of eight lattice constants to be most stable, which is not allowed for many cylinder lengths we chose. Density profiles for different system sizes for the strongly interacting Hubbard model are shown in fig. 4.14. Especially for the narrow cylinders of width $w = 4$ the profiles seem to be less "smooth" and periodic as the ones shown by Ehlers, White, and Noack [48]. As these profiles are highly symmetric and appear to be well converged, this could be interpreted as frustration of oscillations at the preferred wavelength.

Nonetheless, we find amplitudes of the density oscillations which are very comparable to results by Ehlers, White, and Noack [48]. For narrow cylinders they are rather small at $\Delta n \approx 0.025$. One might therefore wonder if these oscillations should be classified as "stripes" and to what extend they are present in the thermodynamic limit. In fig. 4.14 we find that their amplitude does not decrease significantly as the system gets longer. However, as there might be preferred wavelengths we cannot extrapolate from three, rather short systems to the thermodynamic limit.

As was observed by Ehlers, White, and Noack [48], the amplitude tends to *increase* with cylinder width. Unfortunately, we have only very few simulations which could verify this claim. As shown in fig. 4.14c, even calculations at width $w = 6$ do not seem to converge very well—Ehlers, White, and Noack [48] had the same difficulties and therefore extrapolated their density profiles in the truncation error. In figs. 4.14a and 4.14b we show two different simulations for cylinders of width $w = 8$. Neither profile seems to be converged and there appears to be a shift between both results. However, the amplitude is very similar for the different calculations and significantly larger than for the narrow $w = 4$ cylinders.

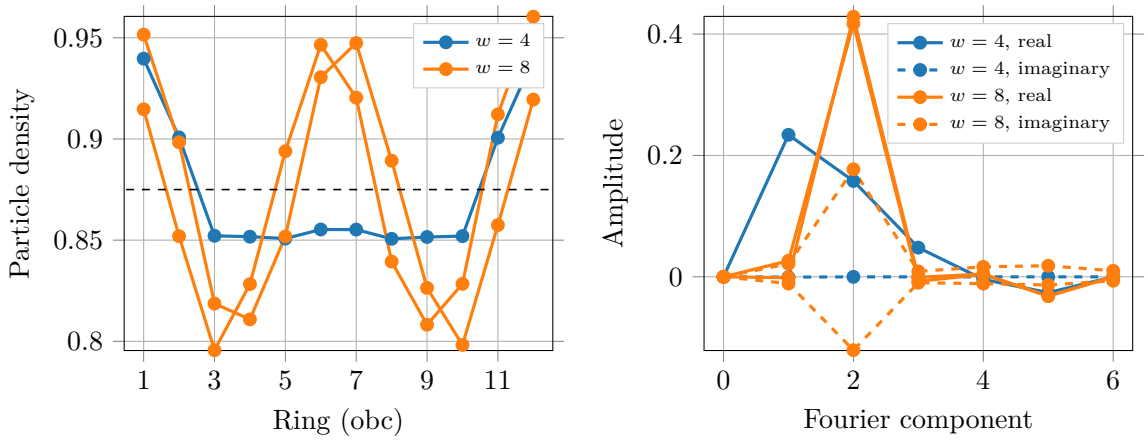

(a) Cylinder length $l = 12$

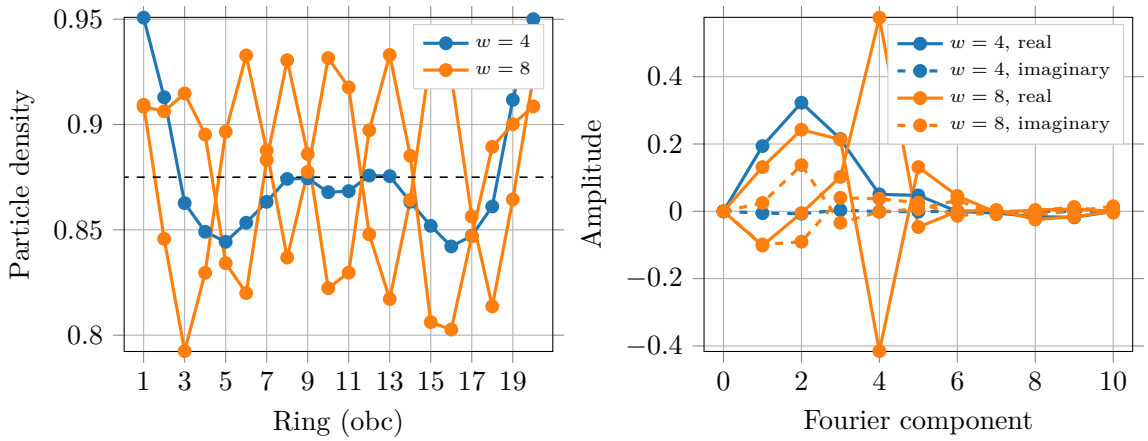

(b) Cylinder length $l = 20$.

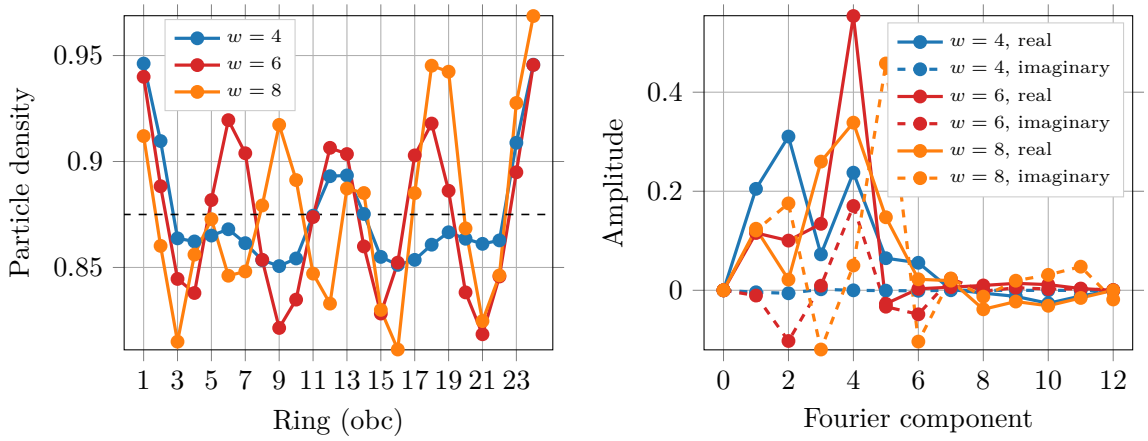

(c) Cylinder length $l = 24$.

Figure 4.14: Density profiles for the strongly interacting $U = 8$, doped $n = 7/8$ Hubbard model on cylinders of different width and length. The amplitude compares well to findings by Ehlers, White, and Noack [48], however the observed wavelengths differ. It appears that oscillations become stronger as the circumference increases, such that we could expect "stripes" to be present in the thermodynamic limit. However, wider cylinders are clearly not well converged.

4.2 Decay of correlations

One needs to be careful when drawing conclusions from measurements of local observables as we did in section 4.1.2. Even if the simulation finds the ground state manifold, we might be looking at the superposition of several different states. While it is not particularly likely that DMRG finds an equally weighted superposition of eigenstates, one might just observe a symmetric density profile even though non of the actual eigenstates features this symmetry. Therefore, we consider looking at *correlators* of local observables to be more physically meaningful.

As DMRG gives access to the full wave function, correlators can be calculated directly. We choose to measure correlators,

$$\langle \hat{n}_{r,1} \hat{n}_{x,1} \rangle - \langle \hat{n}_{r,1} \rangle \langle \hat{n}_{x,1} \rangle, \tag{4.6}$$

for sites $x = 1, l$ on either open end and the center $x = l/2$ with all possible rings r. All sites are on the first leg *in real space*, but as we consider periodic boundaries and enforce momentum conservation, the correlators should be exactly the same on all other legs. Results for a rather small system are plotted in fig. 4.15. The correlators decay exponentially with the distance of both sites and we observe very good agreement for the correlations with a site on either end. For the center site the correlations are slightly asymmetric but follow the same trend.

We note that we did not normalize the correlations properly: one should divide eq. (4.6) by the standard deviations of $\hat{n}$ on both sites such that perfect correlation corresponds to a value of one. We expect that the standard deviations do not depend strongly on the spatial coordinates and thus choose the same normalization for all sites. Therefore, the correlators at $|r - x| = 0$ are not exactly equal to one—we expect to have the same uncertainty for all other plotted values.

In fig. 4.15 we observe exponential decay which is modulated by a cosinusoidal amplitude—yielding local minima e.g. for $|r - x| = 9$. However, it appears there is a very fast decay on the first three sites but the decay rate decreases to a smaller value beyond that. Performing calculations on matrix product states we obviously have to expect an exponential decay of correlations (see Orús [40]) *eventually*. However, as the decay is particularly fast for short separation distances, we expect our observations to be more than just an artifact of DMRG.

To quantify our observations we extract the decay rates by fitting an appropriate function. This is no extremely simple task as we do not only have decay over multiple orders of magnitude but also observe roots due to the cosinusoidal modulation. We start by fitting frequency ω and decay rate d in an ansatz,

$$f(|r - x|) = \mathrm{e}^{d|x-r|} \cos\left(\omega |x - r|\right). \tag{4.7}$$

We use a least-square fit in linear space and therefore only fit the large correlations i.e. we only find the fast decay rate. Dividing through this fit yields a constant function up to the point where the second, slower rate becomes important. In a logarithmic plot this corresponds to a linear increase for $|x - r| > x_0$ and we can fit the parameters x_0 and the slope d',

$$g(|r - x|) = \begin{cases} 0 & |r - x| < x_0, \\ d'(|r - x| - x_0) & |r - x| \geq x_0 \end{cases}. \tag{4.8}$$

Fitting four parameters can be delicate. However, in this case the correlations described by the slower decay rate are so close to zero that they do not influence the first least-squares fit. It appears our fit does not always find the correct frequency of the periodic modulation

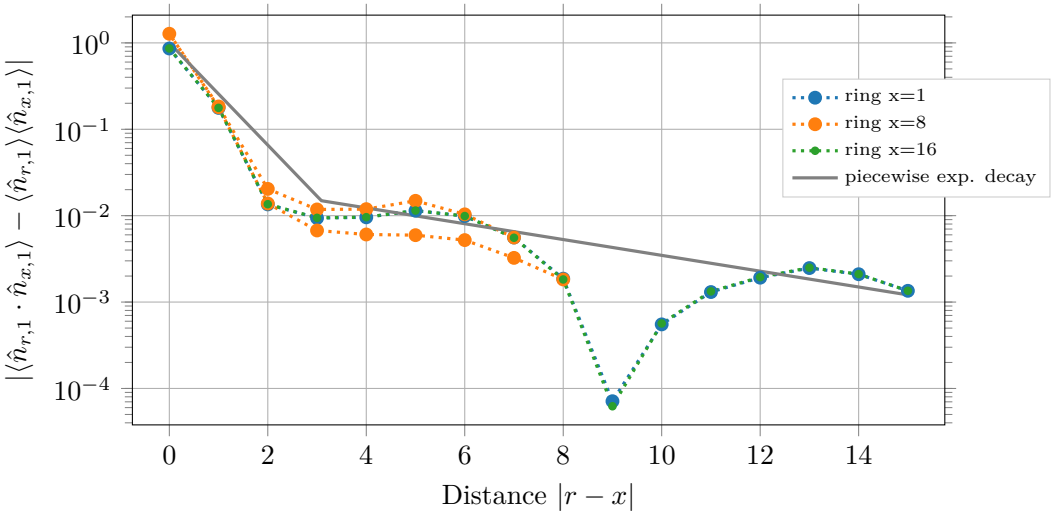

Figure 4.15: Particle number correlators for the doped $n = 7/8$, strongly interacting $U = 8$ Hubbard model of width $w = 4$ and length $l = 16$. We calculate correlators for sites on the first $x = 1$, the last $x = 16$ and a center ring $x = 8$ with all other sites on the same leg. Correlators with a site on either open end agree almost perfectly—indicating converged results. We observe exponential decay of correlations with a cosinusiodal modulation. There appear to be two different rates for the exponential decay which we fitted after removing the modulation. The on-site "correlators" at $r = x$ are not exactly equal to one as we normalize all correlators by the same factor, but the variance might be spatially dependent.

from very few large function values. Nonetheless, the decay rates shown in the following plots seem to match what we would have drawn intuitively.

The decay of correlations we observe is qualitatively identical to findings by Ehlers, White, and Noack [48]. However, they only show occupation correlations for weaker interactions $U = 4$ which we did not compute—a one-to-one comparison is therefore not possible. We show the decay of real-space density correlations for larger systems at the same interaction and doping in fig. 4.16. For longer cylinders, the behavior is pretty much the same, but as the circumference increases the difference between "fast" and "slow" exponential decay rates vanishes. For width $w = 6$ we still observe a transition in fig. 4.16b, which our fitting procedure localizes rather accurately. But for the largest system of width $w = 8$ shown in fig. 4.16c the decay rate is almost constant.

As our simulations exploit $SU(2)$ spin symmetry, expectation values of observables which are not $SU(2)$ symmetric are zero. Therefore, we cannot calculate local spin expectation values $\langle \hat{S}_i^z \rangle$, but we can compute **spin correlators** $\langle \hat{\boldsymbol{S}}_i \cdot \hat{\boldsymbol{S}}_j \rangle$. Note that we calculate correlators in real space, i.e. we Fourier transform real space spin operators to apply them onto our hybrid space state. We performed these calculations only for fewer systems, but we observe a behavior which is qualitatively very similar to the decay of occupation correlations.

In fig. 4.17 we show spin correlators for two systems of width $w = 4$. We observe exponential decay on two different scales, modulated by a cos function. As we do not have results for wider cylinders, we cannot observe whether the differences of long and short distance behavior decrease as the circumference gets larger. We find that the spin correlations decay slower than occupation correlators which agrees with findings by Ehlers, White, and Noack [48].

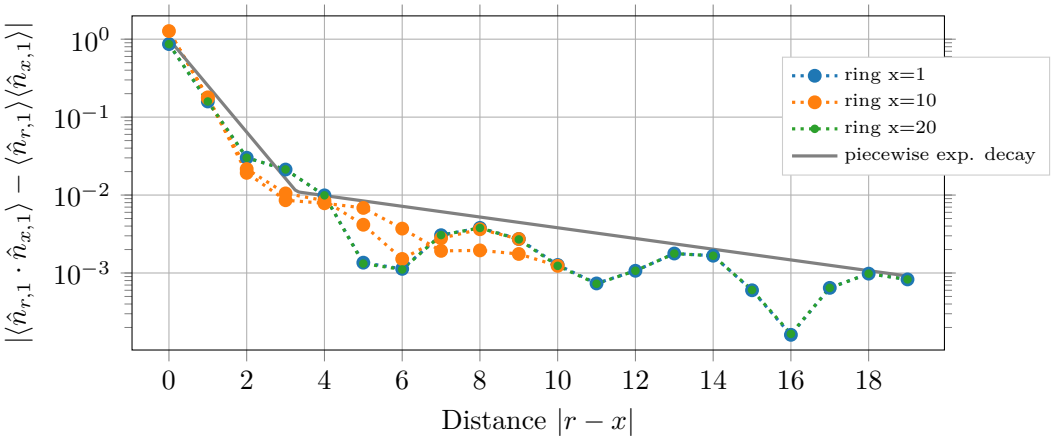

(a) Cylinder of width $w = 4$ and length $l = 20$.

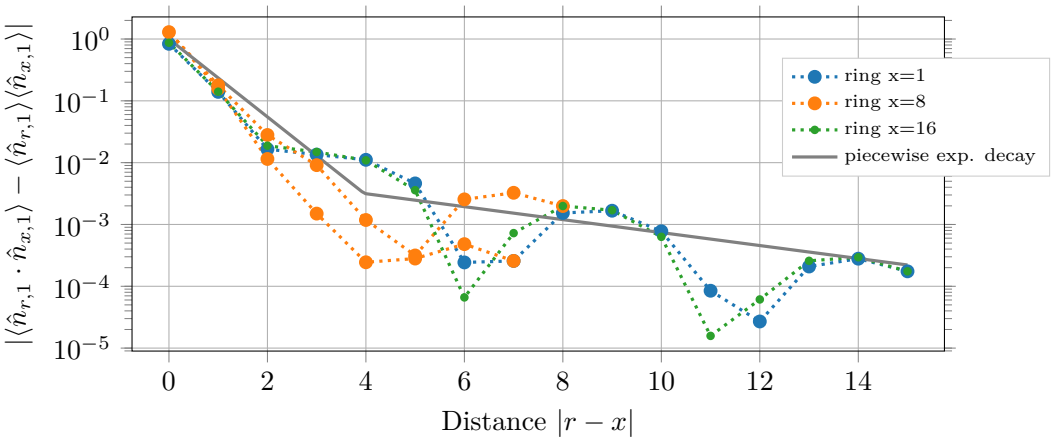

(b) A wider cylinder at $w = 6$, $l = 20$.

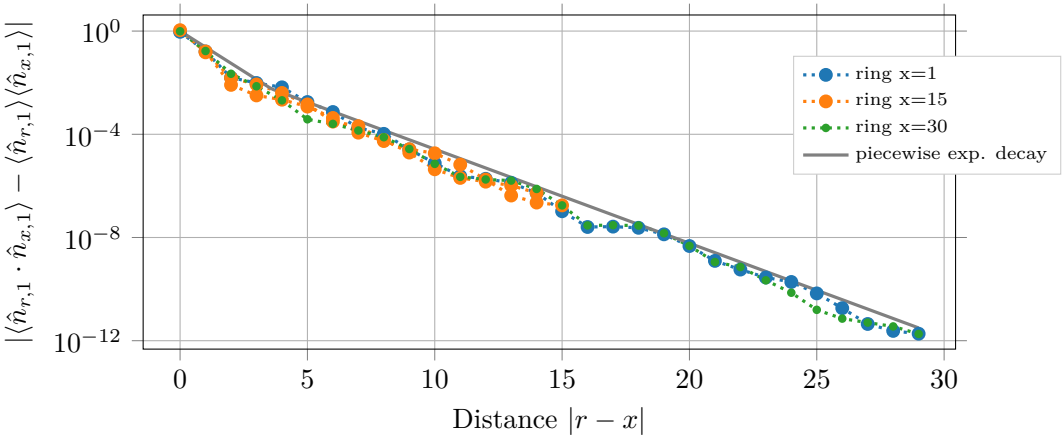

(c) Lattice of size $w = 8$, $l = 30$—thus, likely not converged.

Figure 4.16: Decay of density correlations for the doped $n = 7/8$ strongly interacting $U = 8$ Hubbard model on different lattice sizes. We always find exponential decay, but only narrow systems seem to have two different length scales.

Using the fitting procedure we explained previously, we calculate decay rates for all data sets available. The results for real space occupation correlations are shown in fig. 4.18 as a plot in reciprocal cylinder length. First of all, we observe that the extracted decay rates are rather similar for states in all momentum sectors. This indicates that our fitting procedure yields consistent results. We also like to interpret these different results as alternative error bars.

We find that the initial, fast decay rate barely depends on system size. This indicates that the exponential decay is not caused by too small MPS bond dimensions: for a wider system, there are more tensors on the MPS chain between sites on the same physical leg. The slow decay rate however increases as the system becomes larger. Limitations of matrix product states could be the cause for increasing decay rates with system width. We also observe a nearly linear decrease of the rate with reciprocal system length—which should not be caused by limitations of MPS. A system which fulfills the entropy area law can be represented as matrix product state with constant bond dimensions at arbitrary length.

We show the dependence of spin correlation decay rates on system size in fig. 4.19. As we saw before, the rates are smaller than for particle number correlations. The fast decay rate seems to be independent of cylinder length, but roughly 0.5 smaller than in fig. 4.18. For the slow decay rate we find much larger "errors" than before. We might be looking at a linear decrease in reciprocal length, but we cannot claim with certainty that there actually is a dependence on system length. We do not have the data to compare spin correlation decay rates for wider systems.

In conclusion, we found exponential decay both for spin and occupation correlations. We suppose that these observations are physically correct and no artifact of the DMRG method for the following reasons:

- correlations decay particularly fast on short length scales. If this decay was due to finite bond dimensions, the decay rate should not decrease on longer distances.
- the fast decay rate depends on physical distance, but not on distance in the MPS chain, i.e. it is almost independent of cylinder *width*.
- the slow decay rate depends on circumference—however, more so than if it was enforced by MPS. If the exponential decay was due to limitations of matrix product states, it should depend on the distance in the MPS chain, i.e. $\exp(-dw|x-r|)$ with a system size independent decay rate d. We find decay rates which increase faster than linear in width, which should therefore have a physical reason.
- lastly, the slow decay rate clearly depends on system *length*. This cannot be accounted for by properties of matrix product states and makes it more plausible that the dependence on width has physical reasons as well.

These observations would indicate that the Fermi Hubbard model is not critical at doping $n = 0.875$ and interaction $U = 8$. The absence of long range order seems to contradict the picture of a striped ground state.

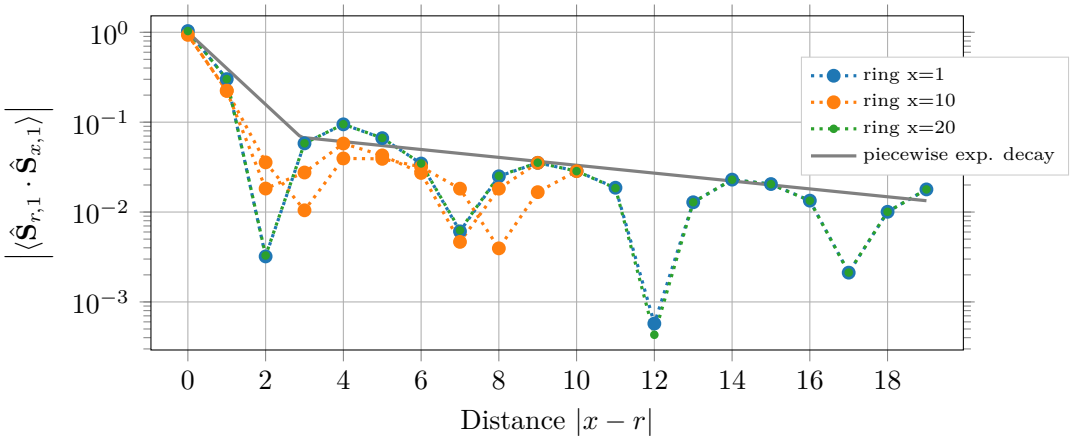

(a) Spin correlations on a cylinder of length $l = 20$. The occupation correlations for the same system are shown in fig. 4.16a. We find that spin correlations decay significantly slower. Also the periodicity is slightly larger for spin correlations, we observe minima at distances $|x - r| \in \{7, 12, 17\}$ instead of $\{6, 11, 16\}$ we saw in fig. 4.16a.

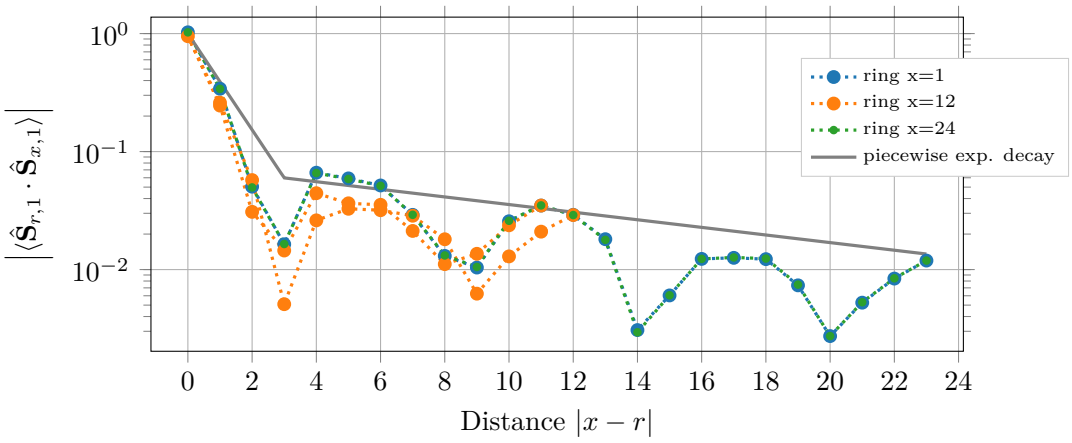

(b) Spin correlations for $l = 24$.

Figure 4.17: Spin correlations for the strongly interacting $U = 8$ Hubbard model at doping $n = 7/8$ on a cylinder of width $w = 4$. The qualitative behavior and the magnitude of correlations is very similar for both cylinder lengths, but the periodicity is different.

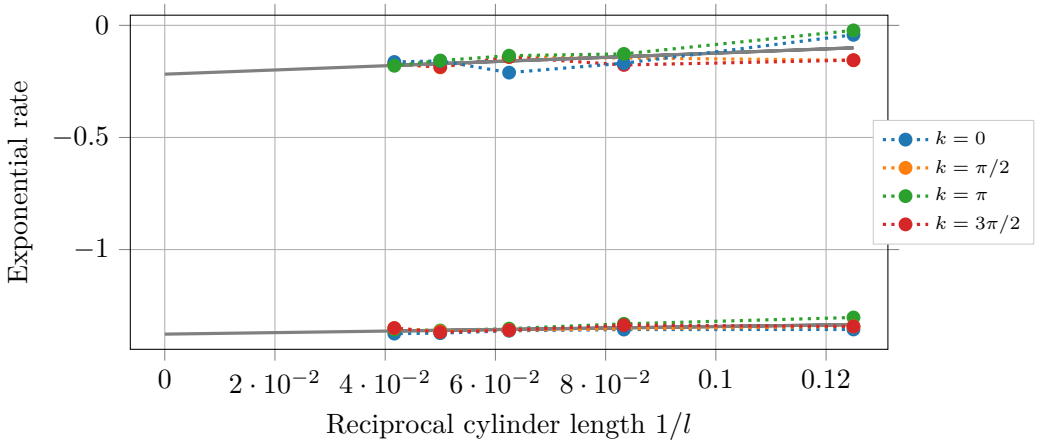

(a) Width $w = 4$.

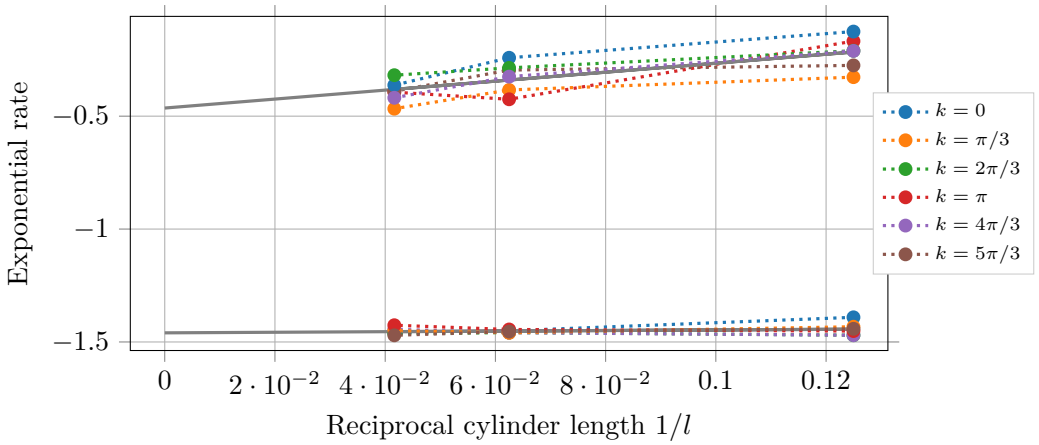

(b) Width $w = 6$.

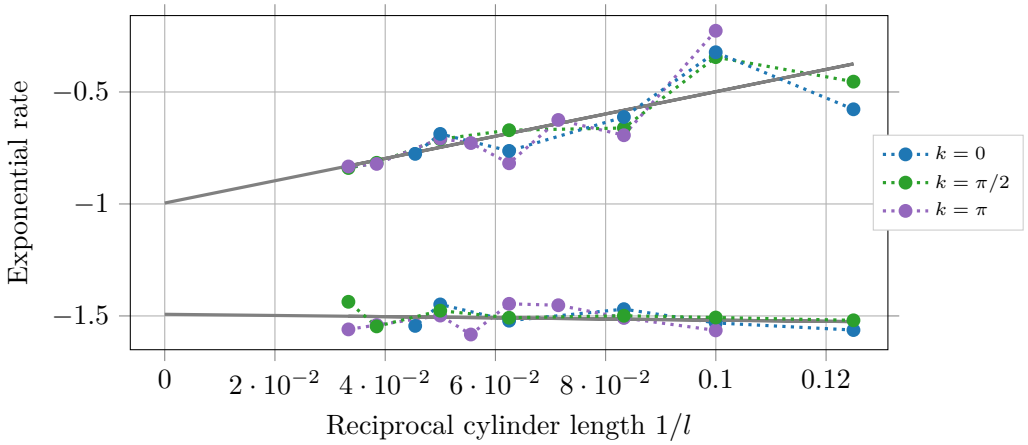

(c) Width $w = 8$.

Figure 4.18: Exponential decay rates for real space occupation correlations. For all plots we consider the strongly interacting $U = 8$ Hubbard model at doping $n = 7/8$. We find the initial, "fast" decay rate to be rather independent of both system length and width. The "slow", long range decay rates seem to decrease linearly in reciprocal cylinder length. The "slow" rate also increases as the circumference gets larger making it questionable whether there are actually two different decay rates in the thermodynamic limit.

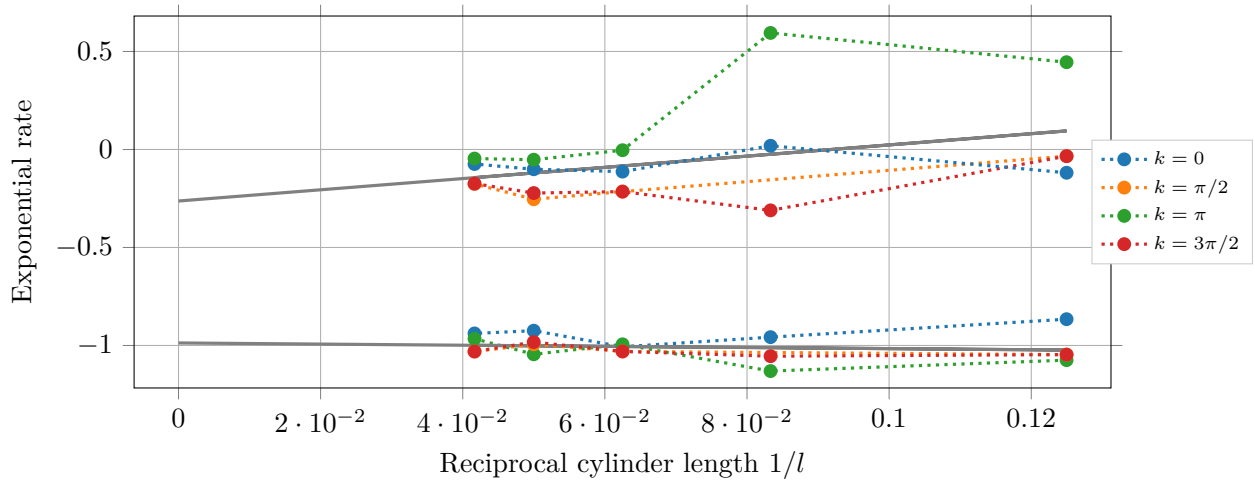

Figure 4.19: Decay rates for real space spin correlations for the systems considered in fig. 4.18a. Qualitatively, the dependence on system size is the same as we saw before: the fast decay rate is constant, the slow one decreases linearly in system length. Spin correlations appear to be longer range than occupation correlations but the error is much larger.

4.3 Ring-wise energies

We saw in section 4.1.1 that ground state energies of finite systems depend linearly on reciprocal length. This is simply due to the positive energy contribution of the open ends: the marginal term $E_m > 0$ for the entire cylinder does not depend on its length, such that we find an additional energy $E_m/(lw)$ for each site. Note that this has nothing to do with the finite size scaling of the two-dimensional Hubbard model. We saw e.g. in fig. 4.1 that the linear extrapolation breaks down for larger lengths.[3] However, beyond this point we expect to find the same scaling $E(l \to \infty)$ as we observe for $E(w \to \infty)$ which is a nonlinear, probably cubic in $1/w$, *increase* to the energy of the thermodynamic limit.

Fitting a linear slope into the energy plot in section 4.1 usually gave us very accurate results. This procedure can also serve as indication whether simulations are converged. Nonetheless, it would be appreciable if we could estimate the infinite size ground state energy from a single simulation. This would not just reduce the computational effort, but it could also help comparing results for systems of different lengths: due to the entire state being a spin singlet, we can only perform simulations for particle densities n which fulfill

$$n \cdot l \cdot w = 2M, \quad M \in \mathbb{N}. \tag{4.9}$$

However, we also require the width w to be even, such that quasi momentum π can be represented. Therefore, only $w = 4$ and $w = 6$ are feasible and the possible choices for particle density n at a given length are limited.

In order to quantify the influence of open ends, we measure local terms of the Hamiltonian individually. The hybrid space Hubbard Hamiltonian eq. (3.50) is made up of an on-site interaction term—which is non-local in hybrid space—and kinetic terms describing hopping along either a leg or a ring. Each of the summands in the interaction and the intra-ring hopping term acts only on sites of the same ring. As we have full access to the wave function, we can compute each of these ring energies separately. The results for one system are shown in fig. 4.20. The terms of the inter-ring part however act on sites of two adjacent rings such that we can only calculate the corresponding energy for a bond instead of a ring. As we want to find the total energy per *ring*, we add half of the inter-ring hopping contribution to the ring on either side of the bond—corresponding to a linear interpolation. The hopping energies per bond and the interpolated ones are also shown in fig. 4.20.

We observe in fig. 4.20 that both interaction energy and intra-ring kinetic terms are not effected strongly by the open boundaries. The hopping energies between rings however show a strong spatial dependence and oscillatory behavior. As we interpolate the bond energies to find energies per ring, the oscillations mostly cancel, but there are strong effects on the open ends.

A simple approach to finding the energy of $l = \infty$ would be to consider only the average energy of the center rings—but we hope we can do better than this. In fig. 4.21 the total energies per ring are shown for different cylinder lengths as a function of distance to the open end. We find oscillating behavior with a period of two lattice constants, which decays quickly. Eventually, we are only interested in the value it decays to for infinity distance from the open end. Yet, to estimate this value we would ideally understand the behavior of the entire function.

For the data shown in fig. 4.21 we find that a function $f(x)$ of distance x to the open end,

$$f(x) = E_0 + a\cos(x\pi)\exp\left(dx^b\right), \tag{4.10}$$

[3] It might rather depend on aspect ratio l/w than on length alone, compare White and Chernyshev [61].

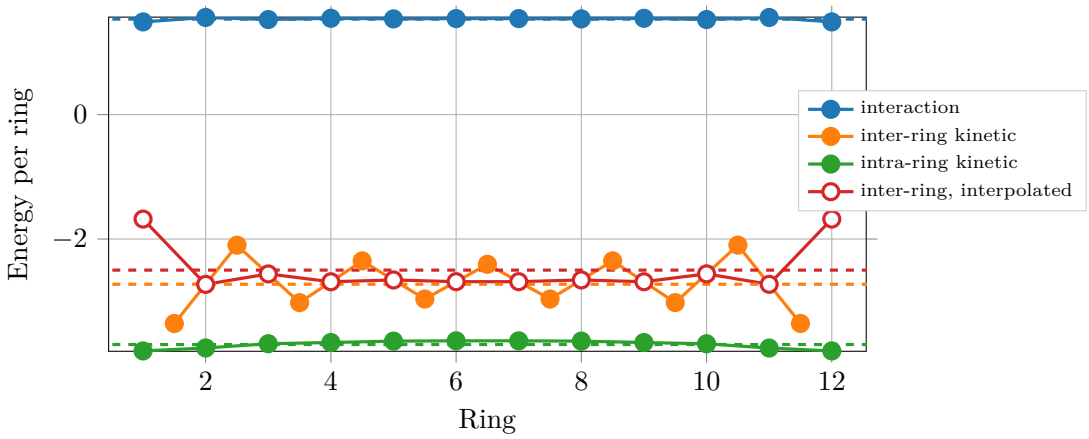

Figure 4.20: Energy contributions of the different terms of the Hamiltonian for each ring. We chose half-filling, weak interactions $U = 2$ and width $w = 4$ to reduce the computational effort. Inter-ring hopping terms act on *bonds* instead of rings. To make results comparable, we add half of their contribution to either neighboring site ("interpolated").

with fitting parameters a, b, d, E_0 can describe the measured values well. Obviously, using four parameters in order to describe 4 to 14 measurements[4] seems like overfitting. However, we only care about the resulting offset E_0 which does not depend significantly on details of the fitting procedure. Initially, we did not use the exponent b as fitting parameter and found almost the same values for E_0, even though the curve barely matched any results of the computation.

In fig. 4.21 we do not only find the fit to describe all measurements well, but we also find consistent results for the fitting parameters. Therefore, the extrapolated energies E_0 according to eq. (4.10) are also shown. The results are not quite independent of cylinder length[5] but the differences are small compared to the "center" energies $E(r = l/2)$.

In fig. 4.22a we compare total energies of finite systems with the ring-wise extrapolated results. The former show the usual linear increase of energy in $1/l$. The ring-wise extrapolated energies are much less dependent on system length, but are slightly lower than the extrapolation of the total energies. To show the differences more clearly, we subtract the linear fit from the finite size energies and plot the results in fig. 4.22b. As the energy for the shortest $l = 8$ system is an outlier in either extrapolation method, we also show results where this value is ignored. It appears that the ring-wise extrapolations yields energies monotonically increasing with length l. But only if we extrapolated this trend to $l = \infty$ we might find agreement with the more straightforward approach of extrapolating energies of finite systems.

In conclusion we think that calculation of local projections of the Hamiltionian separately can be helpful to study the level of convergence by measuring symmetry of the results. Local energies could also help to understand properties of stripes and other spatial inhomogeneities. Originally, we wanted to reduce finite size effects and find a way to extrapolate $E(l = \infty)$ from a single simulation. We are able to reduce the influence of the open ends and find consistent results. However, our results depend on details of the fitting procedure which

[4] Actually 8 to 28 measured ring-wise energies—but the results are almost perfectly invariant under inversion of the system.

[5] They cannot ever be if we do not have appropriate error bars...

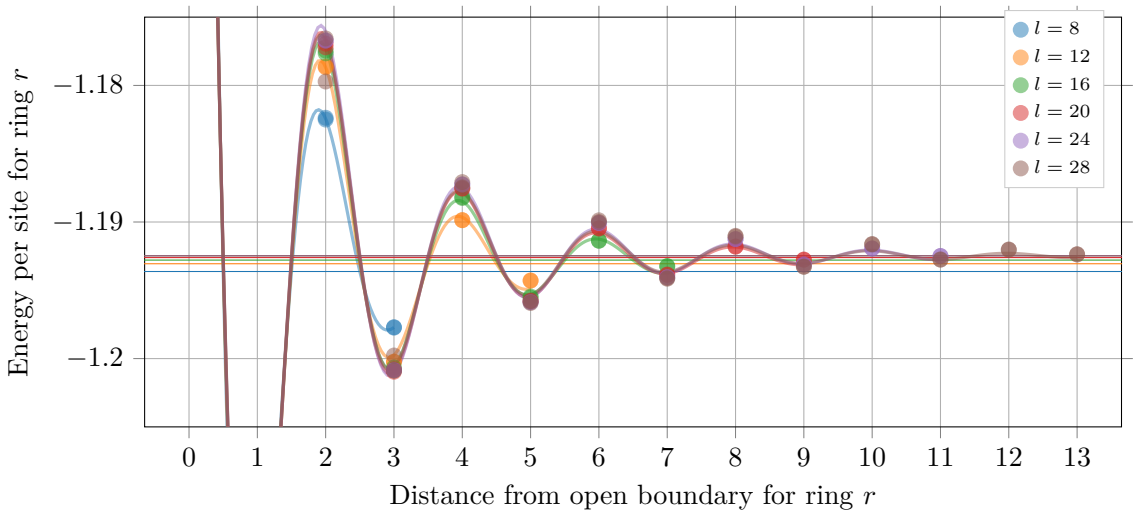

Figure 4.21: Fits for the ring-wise energies as a function of distance from the open end. The data corresponds to the system considered in fig. 4.20, i.e. $U = 2,\ n = 1,\ w = 4$, but we consider several cylinder lengths. As there are two open ends, we show two points for each distance and cylinder length—however, the results are well converged, such that the differences are generally not visible.

lacks theoretical motivation. For example, it might be more accurate to interpolate the different energy terms in fig. 4.20 separately. It is likely that we find qualitatively different results for doped and strongly interacting systems. While we currently lack data for other parameters, we suppose that this approach can also be used to compare systems of different lengths. The results could e.g. demonstrate which wavelengths are energetically favorable for stripes. Or, having in mind the next section, the results could be used to compare energies of dopings which are not allowed at the same system size.

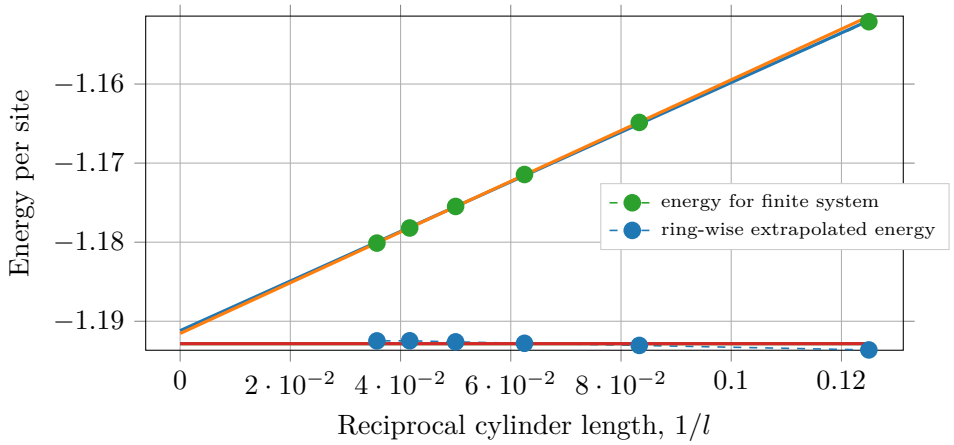

(a) The energies per site either for the entire systems we simulated and the values extrapolated by measuring energies of each ring separately.

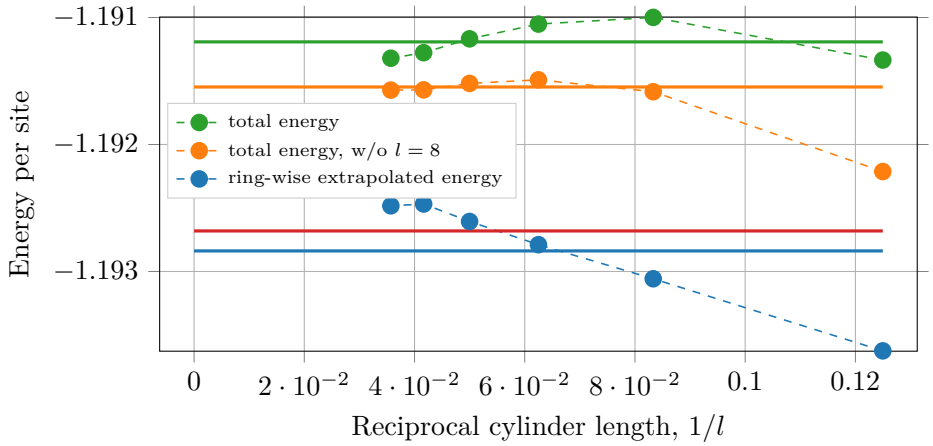

(b) The same energies as in fig. 4.22a but with the linear slope subtracted. The ring-wise extrapolated energies seem to decrease linearly in $1/l$ but all measured values are smaller than the linear extrapolation of total energies would predict.

Figure 4.22: Energies per site for the half-filled weakly interacting $U = 2$ Hubbard model at width $w = 4$. We compare for different cylinder lengths the direct results from our simulation and the values for E_0 we find by measuring energies per ring and fitting eq. (4.10).

4.4 Phase separation

We want to discuss the possibility of phase separation in the two-dimensional Fermi-Hubbard model. Our analysis is inspired by results from Simkovic et al. [69]. They find evidence for separation into phases of different particle density for intermediate interaction strengths and slightly below half-filling. We want to interpret DMRG results in terms of the simple thermodynamic considerations from section 1.5. We saw that the energy needs to be a *convex* function of molar volume and that phase separation could be observed as a flat segment in this curve.

As DMRG energies strongly depend on the lattice size (see sections 4.1 and 4.3), we do not actually vary the volume, but we perform simulations for different fillings for the same lattice geometry. However, a function being convex in molar volume $v := V/N$ is equivalent to it being convex in hole density $n := N/V$. In order to find converged results with acceptable computation effort, we consider only a narrow $w = 4$ cylinder. However, we require a rather long system to reduce effects of open ends but also such that there are many possible dopings which fulfill eq. (4.9).

The energy per site for the Hubbard model at interaction $U = 6$ on a cylinder of size 40×4 is shown in fig. 4.23 for particle numbers $1 \geq n > 0$. Obviously, the curve appears to be convex, but close to half filling the curvature is pretty small. In this most interesting region close to $n = 1$, we computed all possible values of n for a 40×4 system. We show results for all quasi-momentum sectors. Close to $n = 0$ there are large energy differences for the different momentum sectors. For the rest of the curve, there are no differences visible on this scale.

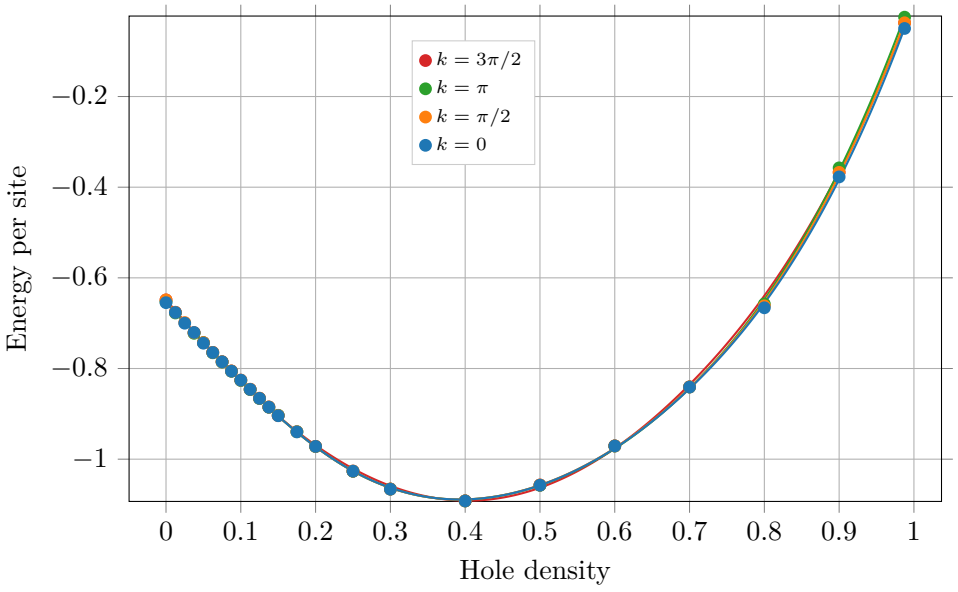

Figure 4.23: Energy per site for the Hubbard model on a 40×4 cylinder at interaction $U = 6$ for various dopings. We show data for all quasi-momentum sectors in hybrid space, which are rather close in energy for the most values of n. We fit a spline which serves illustrative purposes in the next plots.

To highlight the differences between the quasi-momentum sectors, we subtract the ground state energy for each doping in fig. 4.24. We see that the ground state is always in the $k = 0$ or in $k = \pi$ sectors. At half-filling and for very large hole numbers $k = 0$ is clearly the lowest energy sector. States in the sectors $k = \pi/2,\ 3\pi/2$ are always of higher energy than the ground state, however their results are remarkably similar for most dopings—indicating

good convergence and reliable results. For this reason we will also show these energies in the future plots, even though they are not the true ground state.

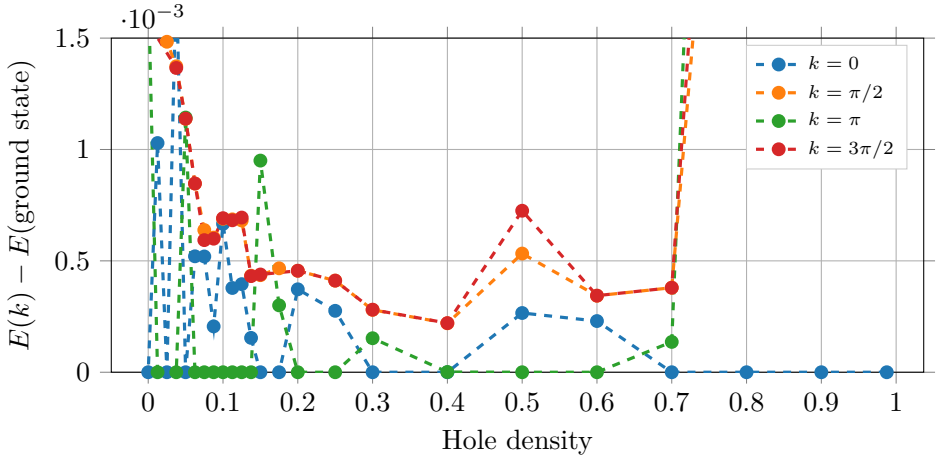

Figure 4.24: Quasi-momentum dependence of the energies shown in fig. 4.23. The values are shifted by the respective ground state energy. At half-filling and when there are only few particles in the system, the ground state is of momentum $k = 0$. For intermediate dopings there is competition between $k = 0$ and $k = \pi$. The ground state is never in one of the two remaining sectors $k = \pi/2, 3\pi/2$, but the lowest energies in these sectors generally agree very well.

Separation into phases of different n would show up in fig. 4.23 as a *linear* segment between n_1 and n_2 (compare section 1.5). To find this region, we calculate the slope of fig. 4.23 by computing differences. In fig. 4.25 we also show the slope of the spline fit from fig. 4.23 as a guide for the eye—there is no physical motivation for this fit. As we zoom in on the region of low doping, $1 - n \leq 0.2$ in fig. 4.25b we indeed find a region $0.07 \leq 1 - n \leq 0.1$ which seems to be flat. For the states in momentum sectors $k = \pi/2, 3\pi/2$ this region is less pronounced. Nonetheless, there is a significant deviation from the smooth interpolation for both curves indicating some kind of plateau.

As we consider systems at low doping the physics stems from the behavior of the holes. It is therefore customary to consider the energy *per hole* rather than per site. One usually plots the dependence on *reciprocal* hole density such that phase separation can be observed just like before. If the energy per site depends linearly on hole density $1 - n$, the energy per hole also depends linearly on $1/(1 - n)$,

$$\frac{E(nV)}{V}\Big|_{V,\text{pt}} = c_1(1-n)+c_0 \quad \Leftrightarrow \quad \frac{E(Vn) - E(V)}{(1-n)V}\Big|_{V,\text{pt}} = (c_0 - E(V))\,\frac{1}{1-n} + c_1, \tag{4.11}$$

however with different proportionality constants. For example White and Scalapino [38] argue that considering the energy per hole is more accurate as we subtract the half-filled energy $E(V)$ of the same system which might reduce finite size effects.

The dependence of energy per hole on reciprocal hole density in fig. 4.26 is also convex, as expected. However, there is a rather flat region highlighted by the black straight lines. As this plot is merely a different way to represent the data plotted in fig. 4.23, we also find indication of phase separation at the same hole densities $0.1 \geq 1 - n > 0.0625$. We once more show data for states with quasi-momentum $k = \pi/2, 3\pi/2$ which are not ground states but also appear to show a linear region, if slightly less pronounced. We find rather large differences for the energies per hole for both curves. This is due to the large difference in energy for the half-filled system, i.e. $E(n = 1, k \in \{\pi/2, 3\pi/2\}) > E(n = 1, k = 0)$.

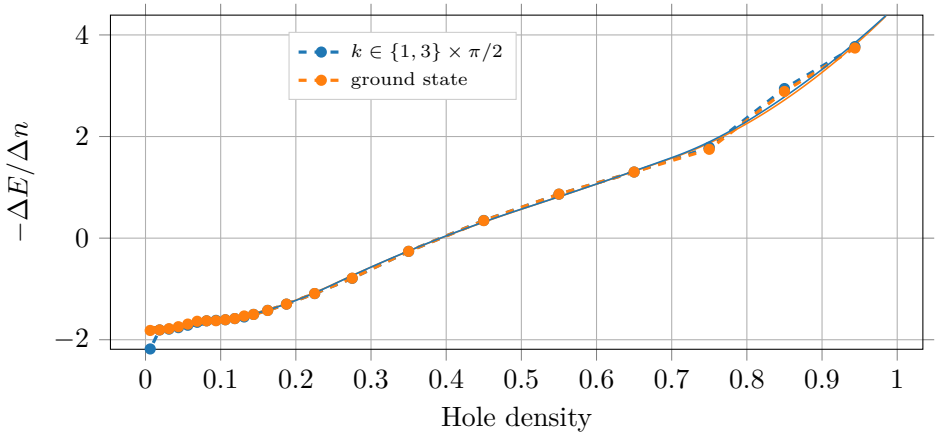

(a) Entire plot from half-filling to zero particles.

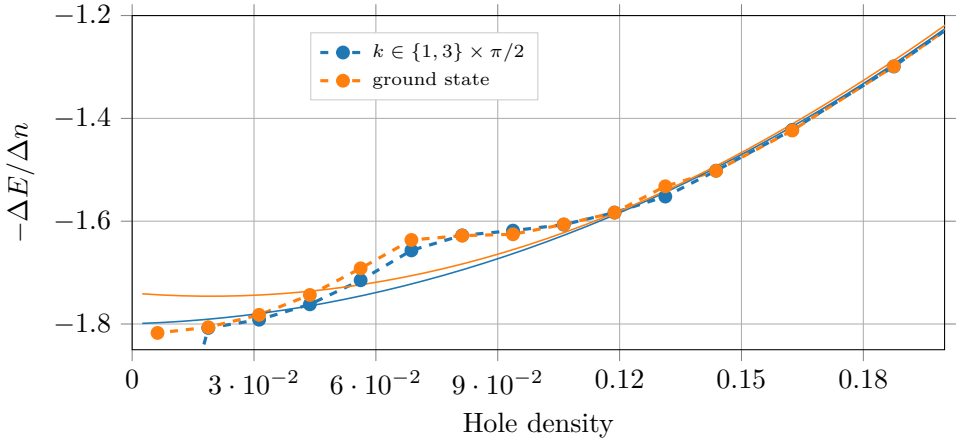

(b) Zoomed in on fig. 4.25a showing a flat region for dopings slightly below 0.1.

Figure 4.25: The slope of the curve in fig. 4.23 by dividing the first differences. In addition to the ground state values, we show data for $k \in \{1,3\} \times \pi/2$ (always the lower energy of both sectors) as the energies seem to have converged well, see fig. 4.24. We also show the spline we fitted in fig. 4.23—it matches the general trend in fig. 4.25a, but does not describe details in fig. 4.25b.

To quantify the "linearity" we once more calculate the slope of the curves in fig. 4.26. For these plots we do not show the initial spline fit from fig. 4.23 as it does not match the points well. However, we think the plateau for $0.1 \geq 1 - n > 0.0625$ is visible with the bare eye.

So far our plots *indicate* phase separation at $U = 6$ in a narrow window of dopings $0.1 \geq 1 - n > 0.0625$. Even if we disregard the fact that we only simulated one system of width $w = 4$ which is far from the thermodynamic limit, we need to ask ourselves: how significant are these results? Can we be sure that there are physical reasons for the energies being "too high" in fig. 4.26 and that we are not just looking at convergence issues?

To address this question we turn to other observables we had already used in section 4.1.2 to judge the level of convergence: we look at density profiles along the real space axis. We find highly symmetric particle density profile for almost all simulations shown in fig. 4.23—they are as symmetric as the first and last profile shown in fig. 4.28. However, precisely for the densities $n \in \{0.8875, 0.9, 0.9125, 0.925\}$, which might be affected by the phase separation, we find much larger antisymmetric components. In fig. 4.28 on the left one can observe these density profiles to be much less "periodic" and as we perform the Fourier transform as

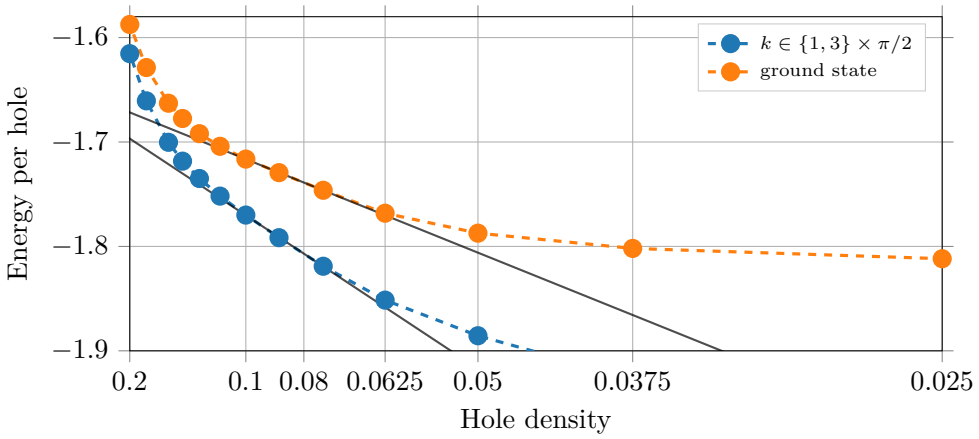

Figure 4.26: Energy per hole versus reciprocal hole density for the Hubbard model at interaction $U = 6$ on a 40×4 lattice. This is simply a different way to plot the data in fig. 4.23. We do not show all data points but zoom in on the region where phase separation might occur. There seems to be a flat region where the straight lines are drawn. As before, we also show values for momentum sectors $k = \pi/2, 3\pi/2$, even though this is not the ground state. The energy per hole is *smaller* for these momenta, because we calculate the energy per hole by subtracting the energy at half-filling. The energy without holes is significantly higher for quasi-momentum sectors $k = \pi/2, 3\pi/2$.

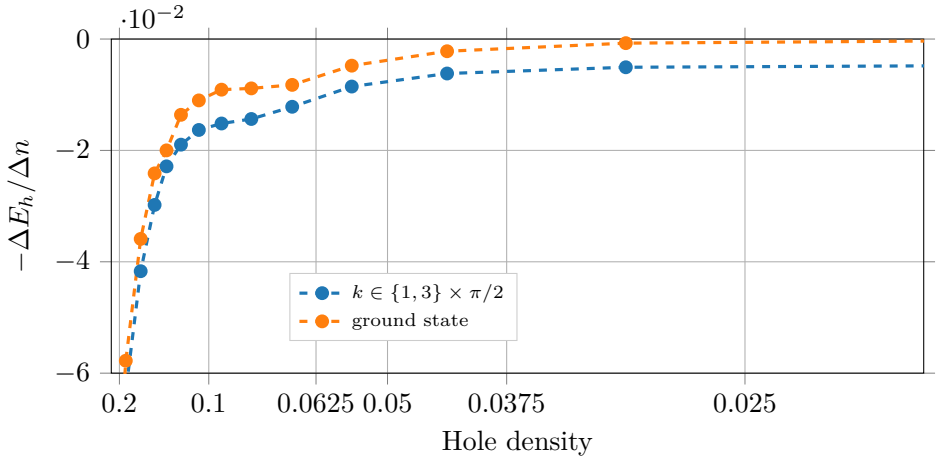

Figure 4.27: The slope of fig. 4.26 by dividing the first differences. The curve seems to be constant between hole densities 0.1 and 0.0625, indicating phase separation.

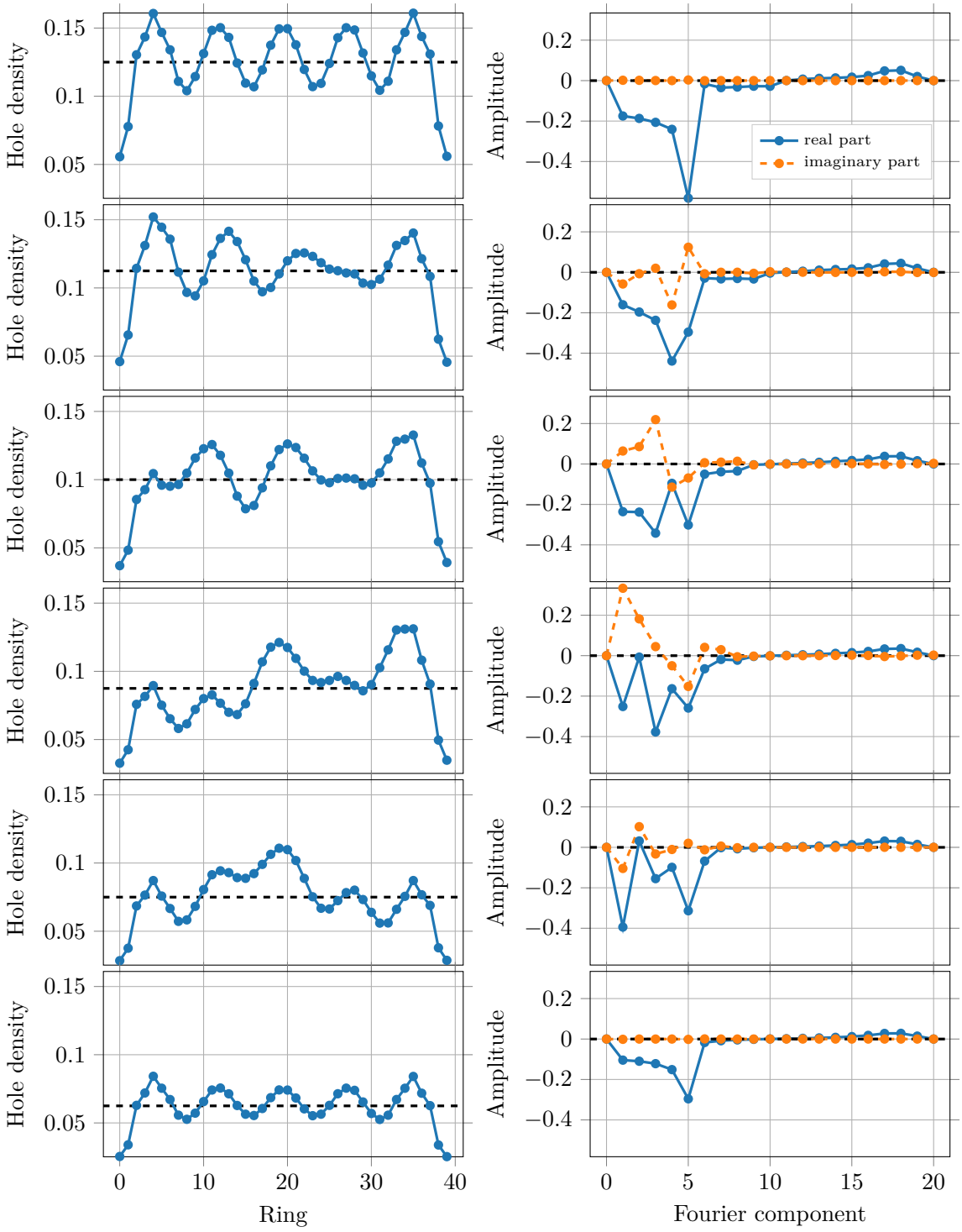

Figure 4.28: Density profiles for the Hubbard model at $U = 6$ on a cylinder of width $w = 4$ for the "relevant" dopings $n = 0.875,\ 0.8875,\ 0.9,\ 0.9125,\ 0.925,\ 0.9375$ (from top to bottom). The first and last plots show highly symmetric density profiles—we find all other other profiles for $n > 0.925$ and $n < 0.8875$ to be equally symmetric. To quantify (anti-)symmetry we show the Fourier transformation of the profiles as described in section 4.1.2.

described in section 4.1.2 we find non-vanishing imaginary contributions which are plotted on the right.

As we argued in section 4.1.2, antisymmetric components *could* be due to a lack of convergence. We are not aware of any feasible[6] approach to rule out this possibility. However, as we performed simulations in all momentum sector for a variety of particle densities, we consider these observations to be significant. In fig. 4.29 we compare the symmetric and antisymmetric components of all calculations performed on this 4×40 cylinder with interaction $U = 6$. We find that density profiles for states in *all* momentum sectors have finite antisymmetric components for hole densities $0.06 \lesssim 1 - n \lesssim 0.12$. We find this observation particularly remarkable as *all* momentum sectors are primarily symmetric for hole densities larger than 0.15.

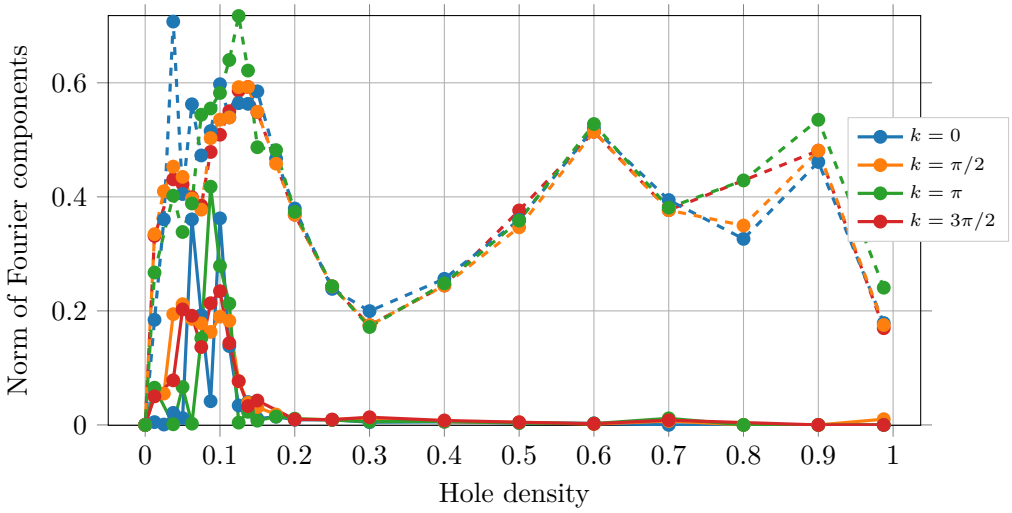

Figure 4.29: Norm of symmetric and antisymmetric components of the density profiles of the Hubbard model with interaction $U = 6$ on a 4×40 cylinder. The antisymmetric components are drawn with a solid line, the symmetric ones with the dashed line. The components correspond to real and imaginary parts plotted on the right of fig. 4.28. We show data for all momentum sectors separately as they behave qualitatively identical.

[6] Calculating the variance would be very elegant—but is too expensive.

5 Conclusion and outlook

In this thesis we have studied the two-dimensional repulsive Fermi-Hubbard model using the DMRG algorithm. This Hubbard model is one of the simplest approaches to describe *interacting* electrons and it is considered to be relevant for understanding high-T_c superconductors.

DMRG for systems in two dimensions comes with exponential costs in lattice *width*. Thus, it is advisable to use periodic boundaries along the width, even though DMRG generally "prefers" open boundaries.

Periodic boundaries yield conservation of quasi-momentum which we can exploit by transforming the Hamiltonian into *hybrid* space: we perform a Fourier transformation *only* along the periodic axis. Therefore, interactions—and thus entanglement—remain local in the MPS chain and DMRG is more efficient. This approach was published by Ehlers, White, and Noack [48] and Motruk et al. [60] and has already been applied to the Hubbard model by the latter collaboration.

In addition to the aforementioned momentum conservation, we employ particle number and $SU(2)$ spin symmetries. The implementation of non-abelian spin symmetries is a rather unique feature of our DMRG toolkit and allows for MPS bond dimensions which are roughly three times as large as for S^z symmetric calculations. Otherwise, we found similar results as Ehlers, White, and Noack [48]: using quasi-momentum conservation the MPS tensors become less dense and we can therefore achieve larger bond dimensions and find lower energies.

In order to reduce the entanglement entropy, we tried to reorder the physical sites in the MPS chain. We found that site ordering has a great impact on DMRG performance, but we were unable to find significant improvements over what has been proposed by Ehlers et al. [59].

We performed DMRG calculations for systems of various sizes, interaction strengths and dopings. We found that our algorithm yields accurate results compared with LeBlanc et al. [34]. Analogous to the findings by Ehlers, White, and Noack [48], hybrid space calculations with quasi-momentum conservation allowed for larger bond dimensions and lower variational energies than real space simulations. Unlike LeBlanc et al. [34] and Ehlers, White, and Noack [48], we cannot perform extrapolation in truncation error such that our extrapolated energies tend to be larger. As an alternative, we considered extrapolation in reciprocal bond dimension but did not find useful results.

Much like Ehlers, White, and Noack [48], we observed highly symmetric, seemingly periodic density profiles in most calculations. We found that these "stripes" seem to increase in amplitude as the systems gets larger but we could only observe exponentially decaying correlations—both for local density and local spin operators.

Eventually, we observed indications for phase coexistence at intermediate interactions *between* the commonly considered occupation numbers of $n = 1$ and $n = 7/8$. By calculating all particle densities possible for our rather small system, we found what appears to be a linear segment in the energy per site versus particle density. This would correspond to a coexistence region of phases with different molar volumes. While it is difficult to determine "linearity" from only very few data points, we could affirm our claims by measuring density

profiles. We found highly symmetric profiles, indicating good convergence, for all densities *except* the ones we assumed to be affected by phase coexistence.

We consider especially the results indicating phase coexistence to be exciting. While we were able to find indications for phase coexistence, we need to improve our methods to achieve definitive and publishable results. First of all, we need corresponding energies for larger systems. As always, we are strictly limited in system width—especially for critical systems, convergence will be difficult to achieve even for width $w = 6$.

For this reason, it is crucial that we find estimates for the error of our results. We have recently implemented two-site DMRG algorithm in our toolkit and are now able to calculate "proper" truncation error. The idea is to stick to the DMRG3S algorithm but to perform single sweeps of two-site DMRG in between to measure the error. We would thus also be able to perform extrapolation in the truncation error.

Once we have estimated errors for the measured energies, we should also employ a more fault-tolerant method to observe phase separation. In section 4.4 we have tried to detect a Maxwell construction by calculating the differences between adjacent data points. This approach is obviously very sensitive to single unconverged simulations. Finding a phase transition in noisy data is not a new problem and we hope to find better results using methods by Emery, Kivelson, and Lin [70] and Boninsegni et al. [71].

Furthermore, we hope that the calculation of ring-wise energies as proposed in section 4.3 could allow for comparing energies of many more particle densities. Alternatively, we could perform simulations on significantly longer cylinders. The latter approach obviously comes at higher computational costs. And while it seems to be more physically motivated, it might not be the "correct" extrapolation to the thermodynamic limit, because we consider systems of very large aspect ratios (compare White and Chernyshev [61]).

Lastly, we would be interested to see if dynamic reordering as described in section 3.3.2 can be used to reduce the entanglement entropy. Choosing the "right" order of sites in the MPS chain is crucial for inhomogeneous Hamiltonians. Minimizing the entanglement distance as measured by the two-site mutual information has proven to be an effective method to improve the ordering. However, calculating the mutual information is costly and requires a sufficiently accurate initial simulation. Switching sites *during* the DMRG updates could do away with both issues but more importantly, it would directly minimize the entanglement entropy of a bipartition of the system—which is precisely what DMRG wants.

Bibliography

[1] J. G. Bednorz, and K. A. Müller, "Possible high-T_c superconductivity in the Ba-La-Cu-O system", en, Zeitschrift für Physik B Condensed Matter **64**, 189–193 (1986).

[2] A. Damascelli, "Angle-resolved photoemission studies of the cuprate superconductors", Review of Modern Physics **75**, 473 (2003), arXiv:0208504 [cond-mat].

[3] "Towards a complete theory of high Tc", en, Nature Physics **2**, 138–143 (2006).

[4] B. Keimer, S. A. Kivelson, M. R. Norman, S. Uchida, and J. Zaanen, "From quantum matter to high-temperature superconductivity in copper oxides", Nature **518**, 179–186 (2015).

[5] B. Freelon, A. Augustsson, J.-H. Guo, P. G. Medaglia, A. Tebano, and G. Balestrino, "Electron Correlation and Charge Transfer in $[(Ba_{0.9}Nd_{0.1})CuO_{2+d}]/[CaCuO_2]_2$ Superconducting Superlattices", 10.1103/PhysRevLett.96.017003.

[6] P. A. Lee, N. Nagaosa, and X. G. Wen, "Doping a Mott insulator: Physics of high-temperature superconductivity", Reviews of Modern Physics **78** (2006) 10.1103/RevModPhys.78.17, arXiv:0410445 [cond-mat].

[7] J. F. Annett, and R. M. Martin, "Two-band Hamiltonian for CuO_2 planes", Physical Review B **42**, 3929–3934 (1990).

[8] F. C. Zhang, and T. M. Rice, "Effective Hamiltonian for the superconducting Cu oxides", Physical Review B **37**, 3759–3761 (1988).

[9] J. Hubbard, "Electron Correlations in Narrow Energy Bands", Proceedings of the Royal Society of London A: Mathematical, Physical and Engineering Sciences **276** (1963).

[10] L. W. Cheuk, M. A. Nichols, K. R. Lawrence, M. Okan, H. Zhang, E. Khatami, N. Trivedi, T. Paiva, M. Rigol, and M. W. Zwierlein, "Observation of spatial charge and spin correlations in the 2D Fermi-Hubbard model", Science **353**, 1260–1264 (2016), arXiv:1606.04089.

[11] J. Spalek, "t-J model then and now: A personal perspective from the pioneering times", (2007), arXiv:0706.4236.

[12] S. R. White, and D. J. Scalapino, "Density Matrix Renormalization Group Study of the Striped Phase in the 2D t-J Model", Physical Review Letters **80**, 1272–1275 (1998), arXiv:9705128 [cond-mat].

[13] H. K. Onnes, "Disappearance of the electrical resistance of mercury at helium temperatures", Proceedings Koninklijke Akademie van Wetenschappen te Amsterdam **14**, 113–115 (1911).

[14] N. W. Ashcroft, and N. D. Mermin, *Solid State Physics* (Saunders College Publishers, 1976).

[15] J. Bardeen, L. N. Cooper, and J. R. Schrieffer, "Theory of Superconductivity", Physical Review **108**, 1175–1204 (1957).

[16] J. Bardeen, and J. Schrieffer, "Chapter VI Recent Developments in Superconductivity", in (1961), pp. 170–287.

[17] W. Ketterle, and M. W. Zwierlein, "Making, probing and understanding ultracold Fermi gases", (2008) 10.1393/ncr/i2008-10033-1, arXiv:0801.2500.

[18]C. Kittel, *Quantum Theory of Solids* (Wiley, 1987).

[19]M. Tinkham, *Introduction to Superconductivity: Second Edition*, Dover Books on Physics (Dover Publications, 2004).

[20]E. Demler, "Fermionic Hubbard model", in *Lecture notes: strongly correlated systems* (2010).

[21]P. W. Anderson, P. A. Lee, M. Randeria, T. M. Rice, N. Trivedi, and F. C. Zhang, "The physics behind high-temperature superconducting cuprates: the 'plain vanilla' version of RVB", Journal of Physics: Condensed Matter **16**, R755 (2004), arXiv:0311467 [cond-mat].

[22]P. Fazekas, and P. W. Anderson, "On the ground state properties of the anisotropic triangular antiferromagnet", Philosophical Magazine **30**, 423–440 (1974).

[23]P. W. Anderson, "The Resonating Valence Bond State in La_2CuO_4 and Superconductivity.", Science **235**, 1196–8 (1987).

[24]A. Paramekanti, M. Randeria, and N. Trivedi, "High-Tc superconductors: A variational theory of the superconducting state", Physical Review B - Condensed Matter and Materials Physics **70**, 1–23 (2004), arXiv:0305611 [cond-mat].

[25]D. J. Scalapino, "The Case for $d_{x^2-y^2}$ Pairing in the Cuprate Superconductors", Physics Reports-Review Section of Physics Letters **250**, 330–365 (1995).

[26]D. J. Scalapino, and S. A. Trugman, "Local antiferromagnetic correlations and $d_{x^2-y^2}$ pairing", Philosophical Magazine Part B **74**, 607–610 (1996).

[27]J. M. Tranquada, B. J. Sternlieb, J. D. Axe, Y. Nakamura, and S. Uchida, "Evidence for stripe correlations of spins and holes in copper oxide superconductors", Nature **375**, 561–563 (1995).

[28]L. Landau, and E. Lifshitz, *Course of theoretical physics Vol. 5. Statistical physics, part 1*, Third edit (Pergamon, 1980).

[29]U. Schollwöck, "Lecture Notes: Thermodynamics and Statistical Physics", München, 2016.

[30]A. Parola, S. Sorella, S. Baroni, R. Car, M. Parrinello, and E. Tosatti, "Recent numerical results on the two dimensional Hubbard model", Physica C: Superconductivity **162-164**, 771–772 (1989).

[31]G. Fano, F. Ortolani, and A. Parola, "Hole-hole effective interaction in the two-dimensional Hubbard model", Physical Review B **42**, 6877–6880 (1990).

[32]S. R. White, D. J. Scalapino, R. L. Sugar, E. Y. Loh, J. E. Gubernatis, and R. T. Scalettar, "Numerical study of the two-dimensional Hubbard model", Physical Review B **40**, 506–516 (1989).

[33]E. Y. Loh, J. E. Gubernatis, R. T. Scalettar, S. R. White, D. J. Scalapino, and R. L. Sugar, "Sign problem in the numerical simulation of many-electron systems", Physical Review B **41**, 9301–9307 (1990).

[34]J. P. F. LeBlanc, A. E. Antipov, F. Becca, I. W. Bulik, G. K.-L. Chan, C.-m. Chung, Y. Deng, M. Ferrero, T. M. Henderson, C. A. Jiménez-Hoyos, E. Kozik, X.-w. Liu, A. J. Millis, N. V. Prokof'ev, M. Qin, G. E. Scuseria, H. Shi, B. V. Svistunov, L. F. Tocchio, I. S. Tupitsyn, S. R. White, S. Zhang, B.-X. Zheng, Z. Zhu, and E. Gull, "Solutions of the Two-Dimensional Hubbard Model: Benchmarks and Results from a Wide Range of Numerical Algorithms", Physical Review X **5**, 041041 (2015), arXiv:1505.02290v1.

[35]D. Scalapino, and S. White, "Stripe structures in the t-t'-J model", Physica C: Superconductivity **481**, 146–152 (2012), arXiv:1204.5212.

[36]S. R. White, and D. J. Scalapino, "Why do stripes form in doped antiferromagnets and what is their relationship to superconductivity?", (2000), arXiv:0006071 [cond-mat].

[37]S. R. White, and D. J. Scalapino, "Energetics of Domain Walls in the 2D t-J Model", Physical Review Letters **81**, 3227–3230 (1998).

[38]S. R. White, and D. J. Scalapino, "Phase separation and stripe formation in the two-dimensional t-J model: A comparison of numerical results", Physical Review B **61**, 6320–6326 (2000), arXiv:9907375 [cond-mat].

[39]P. Corboz, T. M. Rice, and M. Troyer, "Competing States in the t-J Model: Uniform d-Wave State versus Stripe State", Physical Review Letters **113**, 046402 (2014).

[40]R. Orús, "A practical introduction to tensor networks: Matrix product states and projected entangled pair states", Annals of Physics **349**, 117–158 (2014), arXiv:1306.2164.

[41]P. Corboz, S. R. White, G. Vidal, and M. Troyer, "Stripes in the two-dimensional t-J model with infinite projected entangled-pair states", Physical Review B **84**, 041108 (2011), arXiv:1104.5463.

[42]C. Shih, Y. Chen, and T. Lee, "Revisit phase separation of the two-dimensional t-J model by the power-Lanczos method", Journal of Physics and Chemistry of Solids **62**, 1797–1811 (2001).

[43]S. Rommer, S. R. White, and D. J. Scalapino, "Phase separation in t-J ladders", Physical Review B **61**, 13424–13430 (2000).

[44]S. R. White, and D. J. Scalapino, "Pairing on striped t-t'-J lattices", Physical Review B **79**, 220504 (2009), arXiv:0810.0523.

[45]P. Corboz, "Improved energy extrapolation with infinite projected entangled-pair states applied to the two-dimensional Hubbard model", Physical Review B **93**, 045116 (2016).

[46]S. R. White, and D. J. Scalapino, "Stripes on a 6-Leg Hubbard Ladder", Physical Review Letters **91**, 136403 (2003).

[47]G. Bedürftig, B. Brendel, H. Frahm, and R. Noack, "Friedel oscillations in the open Hubbard chain", Physical Review B **58**, 10225–10235 (1998), arXiv:9805123 [cond-mat].

[48]G. Ehlers, S. R. White, and R. M. Noack, "Hybrid-space density matrix renormalization group study of the doped two-dimensional Hubbard model", (2017), arXiv:1701.03690.

[49]U. Schollwöck, "The density-matrix renormalization group in the age of matrix product states", Annals of Physics **326**, 96–192 (2011), arXiv:1008.3477.

[50]J. Eisert, M. Cramer, and M. B. Plenio, "Colloquium: Area laws for the entanglement entropy", Reviews of Modern Physics **82**, 277–306 (2010), arXiv:0808.3773.

[51]S. Singh, R. N. C. Pfeifer, and G. Vidal, "Tensor network states and algorithms in the presence of a global U(1) symmetry", Physical Review B **83**, 115125 (2011), arXiv:1008.4774.

[52]A. Weichselbaum, "Non-abelian symmetries in tensor networks: A quantum symmetry space approach", Annals of Physics **327**, 2972–3047 (2012), arXiv:1202.5664.

[53]S. Singh, and G. Vidal, "Tensor network states and algorithms in the presence of a global SU(2) symmetry", Physical Review B - Condensed Matter and Materials Physics **86**, 1–31 (2012), arXiv:1008.4774.

[54]S. R. White, "Density matrix formulation for quantum renormalization groups", Physical Review Letters **69**, 2863–2866 (1992).

[55]C. Hubig, I. P. McCulloch, and U. Schollwöck, "Generic construction of efficient matrix product operators", Physical Review B **95**, 035129 (2017).

[56]R. N. C. Pfeifer, J. Haegeman, and F. Verstraete, "Faster identification of optimal contraction sequences for tensor networks", Physical Review E **90**, 033315 (2014), arXiv:1304.6112.

[57]C. Hubig, I. P. McCulloch, U. Schollwöck, and F. A. Wolf, "Strictly single-site DMRG algorithm with subspace expansion", Physical Review B - Condensed Matter and Materials Physics **91**, 1–10 (2015), arXiv:1501.05504.

[58]H. N. Phien, J. A. Bengua, H. D. Tuan, P. Corboz, and R. Orús, "Infinite projected entangled pair states algorithm improved: Fast full update and gauge fixing", Physical Review B **92**, 035142 (2015).

[59]G. Ehlers, J. Sólyom, O. Legeza, and R. M. Noack, "Entanglement structure of the Hubbard model in momentum space", Physical Review B - Condensed Matter and Materials Physics **92**, 1–14 (2015), arXiv:1508.07477.

[60]J. Motruk, M. P. Zaletel, R. S. K. Mong, and F. Pollmann, "Density matrix renormalization group on a cylinder in mixed real and momentum space", Physical Review B **93**, 155139 (2016), arXiv:1512.03318.

[61]S. R. White, and A. L. Chernyshev, "Néel order in square and triangular lattice heisenberg models", Physical Review Letters **99**, 2–5 (2007), arXiv:0705.2746.

[62]M. M. Wolf, F. Verstraete, M. B. Hastings, and J. I. Cirac, "Area laws in quantum systems: Mutual information and correlations", Physical Review Letters **100**, 1–4 (2008), arXiv:0704.3906.

[63]E. Fertitta, B. Paulus, G. Barcza, and Ö. Legeza, "Investigation of metal–insulator-like transition through the ab initio density matrix renormalization group approach", Physical Review B **90**, 245129 (2014).

[64]J. E. Atkins, E. G. Boman, and B. Hendrickson, "A spectral algorithm for seriation and the consecutive ones problem", SIAM Journal on Computing **28**, 297–310 (1998).

[65]C. Krumnow, L. Veis, Ö. Legeza, and J. Eisert, "Fermionic Orbital Optimization in Tensor Network States", Physical Review Letters **117**, 210402 (2016), arXiv:1504.00042.

[66]E. M. Stoudenmire, and S. R. White, "Real-space parallel density matrix renormalization group", Physical Review B **87**, 155137 (2013).

[67]A. W. Sandvik, "Finite-size scaling of the ground-state parameters of the two-dimensional Heisenberg model", Physical Review B **56**, 11678–11690 (1997), arXiv:9707123v1 [arXiv:cond-mat].

[68]W. H. Press, *Numerical Recipes 3rd Edition: The Art of Scientific Computing* (Cambridge University Press, 2007).

[69]F. I. Simkovic, Y. Deng, N. V. Prokof, B. Svistunov, I. Tupitsyn, and E. Kozik, "Controlled evidence for phase separation and strong magnetic fluctuations in the two-dimensional repulsive Hubbard model near half-filling", 2016.

[70]V. J. Emery, S. A. Kivelson, and H. Q. Lin, "Phase separation in the t-J model", Physical Review Letters **64**, 475–478 (1990).

[71]M. Boninsegni, A. B. Kuklov, L. Pollet, N. V. Prokof, B. V. Svistunov, and M. Troyer, "Vacancies in solid 4 He", 2008.

Acknowledgments

So writing this thesis took a little longer than I had hoped. But I guess that is how it goes when you spend a lot of time figuring out what you actually want to do. And in the end it is about the things you learned along the way, so a bit of wandering around might not be too bad.

Trying not to be too sentimental, I would like to thank:

- *Claudius Hubig* with whom I worked together for basically all of this thesis. He developed our DMRG toolkit and spent quite some time explaining it to me in detail. Not like I would have understood everything, yet... So I am happy he will be staying around in Munich!
- *Mareike Bojer* for the weekends we were both staring at our notebooks trying to work on our theses. And, well... more importantly for the times we did not even try to be productive.
- *Prof. Ulrich Schollwöck* for giving me the opportunity to conduct my thesis at his chair without making a fuzz (yes, I am looking at someone particular...). More importantly, I want to thank him for the cooperation which was really straightforward—in the best sense of the word: he gave us a free hand in doing our work but was always there for help if we asked him.
- my office mate *Jan Stolpp* with whom I had the most random, but often surprisingly insightful, physical discussions.
- all the other nice people at our chair: I am looking forward to next ≈ 3 years working with you... and yeah, you will get a cake sometime soon.
- *Till Klostermann, Mareike Bojer* and *Claudius Hubig* for proof reading this thesis. All remaining typos are basically their fault...

Deklaration

Hiermit erkläre ich, dass ich die Arbeit selbstständig verfasst habe, und dass ich keine anderen Quellen und Hilfsmittel als die angegebenen benutzt habe.

München, 6. März 2017, Leo Stenzel